VIBRATIONAL SPECTROSCOPY AND IMAGING OF PHARMACOLOGICAL AGENTS AND WATER INTERACTION WITH THE SKIN BARRIER

I. EFFECTS OF PERMEATION ENHANCERS ON FLUFENAMIC ACID DELIVERY IN EX VIVO HUMAN SKIN BY CONFOCAL RAMAN MICROSCOPY

II. INFRARED INVESTIGATION OF TERBINAFINE INTERACTION WITH STRATUM CORNEUM CONSTITUENTS

III. COMPARISON OF HYDRATION LEVELS IN HUMAN SKIN UPON APPLICATION OF COMMERCIAL MOISTURIZERS BY CONFOCAL RAMAN MICROSCOPY

by

YELENA PYATSKI

A Dissertation submitted to the

Graduate School-Newark

Rutgers, The State University of New Jersey

in partial fulfillment of the requirements

for the degree of

Doctor of Philosophy

Graduate Program in Chemistry

written under the direction of

Professor Richard Mendelsohn

and approved by

_____

_____

_____

_____

_____

Newark, New Jersey
May, 2019

ABSTRACT

VIBRATIONAL SPECTROSCOPY AND IMAGING OF PHARMACOLOGICAL AGENTS AND WATER INTERACTION WITH SKIN BARRIER

YELENA PYATSKI

Thesis director: Professor Richard Mendelsohn

Vibrational spectroscopy and imaging are advantageous for a number of dermatological applications, including characterization of endogenous components of skin or tracking penetration of pharmaceutical or cosmetic agents in skin tissue. Three applications illustrating the power of these techniques are described herein.

I. EFFECTS OF PERMEATION ENHANCERS ON FLUFENAMIC ACID DELIVERY IN EX VIVO HUMAN SKIN BY CONFOCAL RAMAN MICROSCOPY

For topical delivery to be effective, a drug or active agent must cross the stratum corneum (SC) barrier into viable tissue. As such, barrier modification has been the target of many approaches for epidermal, dermal and transdermal delivery. The use of permeation enhancers in formulations is certainly one of the most widespread approaches. In the current study, flufenamic acid (FluA), a non-steroidal anti-inflammatory drug, is used as a model active agent to investigate the influence of hydrophobic versus hydrophilic permeation enhancers on its penetration and spatial distribution in ex vivo human skin using confocal Raman microscopy. In separate experiments, FluA in octanol (hydrophobic environment) or propylene glycol/ethanol (75/25) (hydrophilic environment) was applied to the SC surface for varying time periods followed by evaluation of penetration via confocal Raman mapping. Use of deuterated versions of the aforementioned enhancers permit us to spectroscopically distinguish the exogenous chemicals from the endogenous

SC lipids without affecting penetration parameters. The FluA pathway is tracked by the C=C stretching mode at ~1618 cm^{-1}. The spatial distribution and relative concentration of exogenous materials along with perturbation to the skin molecular and ultrastructure are imaged using both univariate and multivariate analysis. This, in turn, provides insight into mechanisms of delivery.

II. INFRARED INVESTIGATION OF TERBINAFINE INTERACTION WITH STRATUM CORNEUM CONSTITUENTS

Stratum corneum, the outermost layer of the epidermis, consists of keratin-filled corneocytes embedded in a highly ordered lipid matrix. This structure provides the main permeability barrier of the skin and also maintains water homeostasis. Efficient cutaneous delivery often introduces modifications to the SC. Terbinafine is a small, fungicidal, lipophilic drug commonly applied using topical formulations. Previous studies have utilized quantitative techniques to evaluate the amount of terbinafine in skin. In addition, others have used model systems such as defatted, powdered keratin to study binding parameters. Generally, there is a paucity of research evaluating the molecular nature of terbinafine interaction in skin environments. Current work evaluates molecular structure alterations to specific SC constituents upon interaction with terbinafine in a "physiological" environment, i.e. *ex vivo* intact SC. In this study, isolated human SC was incubated in an ethanol/buffer solution of terbinafine followed by the acquisition of temperature-dependent IR spectra. IR spectroscopy is a widely used, non-destructive technique for studies of lipid and keratin structure in intact human SC. IR bands are very sensitive to secondary structure alterations in keratin and to lipid acyl chain packing/conformational order. Terbinafine was found to perturb keratin secondary structure. Partial reversibility of the terbinafine-induced changes was observed upon soaking with ethanol/buffer while reversibility was more

pronounced upon exposure to high relative humidity. Terbinafine-induced changes in endogenous lipid order, monitored by the symmetric CH_2 stretching frequencies, were mostly masked by the effect of ethanol. Finally, we note that this method is not limited to studies of terbinafine interaction with skin, but can also be applied to monitor perturbations in intact SC when evaluating dosage levels and a variety of topical drugs or cosmetics. The ability to monitor the API (active pharmaceutical ingredient) allows formulations to be screened for delivery of APIs into the SC or across the SC depending on the desired location of action.

III. COMPARISON OF HYDRATION LEVELS IN HUMAN SKIN UPON APPLICATION OF COMMERCIAL MOISTURIZERS BY CONFOCAL RAMAN MICROSCOPY

The appearance of facial youthfulness and radiance results from hydrated, moisturized skin. As skin ages, it loses its natural ability to retain moisture and becomes rough, dry, while resulting in a clinically dull appearance with a loss of radiance, firmness, and suppleness. These symptoms can be delayed and improved with therapeutic use of a moisturizer that builds and maintains moisturization over time; however, most moisturizers that occlude the skin surface are perceived as heavy, greasy and are not consumer-preferred.

A unique, consumer-preferred natural moisturizing factor (NMF) formula was developed, which mimics SC naturally occurring components, with specific emulsifiers that deliver water deep into skin. This formulation (advanced NMF moisturizer) provides immediate hydration and protection (or enhancement) of the skin barrier over time to lock in moisture.

Confocal Raman spectroscopy studies assessed the distribution of water in ex vivo skin after topical application of the new formulation, advanced NMF moisturizer and a leading humectant moisturizer. In contrast to a leading humectant moisturizer that does not contain NMF components, the NMF-containing formulation significantly increased the relative water content and spatial distribution of water throughout epidermal regions of skin.

The results from these studies illustrate that increasing skin water content in both the stratum corneum and viable layers of the epidermis through therapeutic hydration with an NMF-containing formula can significantly improve skin hydration, barrier function, and the clinical appearance of skin radiance.

Acknowledgements

I would like to thank my advisor, Dr. Richard Mendelsohn, for his guidance and support throughout this project, along with Dr. Carol Flach. I also would like to extend my gratitude to a postdoctoral member of the Mendelsohn group, Qihong Zhang, for her helpful recommendations with numerous laboratory techniques. And I'd like to thank my friends and family for their constant love and support as I progress through my degree. Special thanks goes to my grandma Frima Geller, who always encouraged me to step out of my comfort zone and try out new things. She passed away this January and this thesis is dedicated to her.

Table of Contents

List of Figures

List of Tables

List of Abbreviations

Alpha-hydroxy acids	AHAs
Active pharmaceutical ingredient	API
Asymmetric stretch	assym
Confocal Raman microscopy	CRM
Confocal Raman spectroscopy	CRS
Center of mass	COM
Ceramides	CER
Cetaphil	CP
Charged-coupled device	CCD
Chemical penetration enhancers	CPEs
Dermal replenishment	DR
Ethanol	EtOH
Ethanol-D6	Et-d
Film forming solution	FFS
Flufenamic acid	FluA
Fourier transform infrared radiation	FTIR
Franz diffusion cell	FDC
Hexagonal packing	HEX
High performance liquid chromatography	HPLC
Lamellar bodies	LBs
Lipid	Lip
Liquid packing	LIQ
Long periodicity phase	LPP
Mercury cadmium telluride	MCT
Natural moisturizing factor	NMF
n-octyl-d_{17} alcohol	Oct-d
Oil-in-water	o/w
Orthorhombic packing	OR
1,2-propanediol-d6	PG-d
Peak height ratio	PHR

Phosphate buffer solutions	PBS
Polyhydroxy acid	PHA
Principal component analysis	PCA
Pyrrolidone carboxylic acid	PCA
Propylene Glycol	PG
Relative humidity	RH
Room temperature	RT
Short periodicity phase	SPP
Standard deviation	SD
Stratum basale	SB
Stratum corneum	SC
Stratum granulosum	SG
Stratum spinosum	SS
Symmetric stretch	sym
Transepidermal water loss	TEWL
Terbinafine	Ter
Viable Epidermis	VE
Ultra Violet	UV

Chapter 1 Introduction

1.1 Skin structure

1.1.1 Basic skin structure and function

Skin is the largest organ in the body and represents about 16% of body total weight. Skin serves as a barrier to protect efflux of endogenous substances and influx of exogenous substances. The skin also has important immune and sensory functions, helps to regulate body temperature, and synthesizes vitamin D.

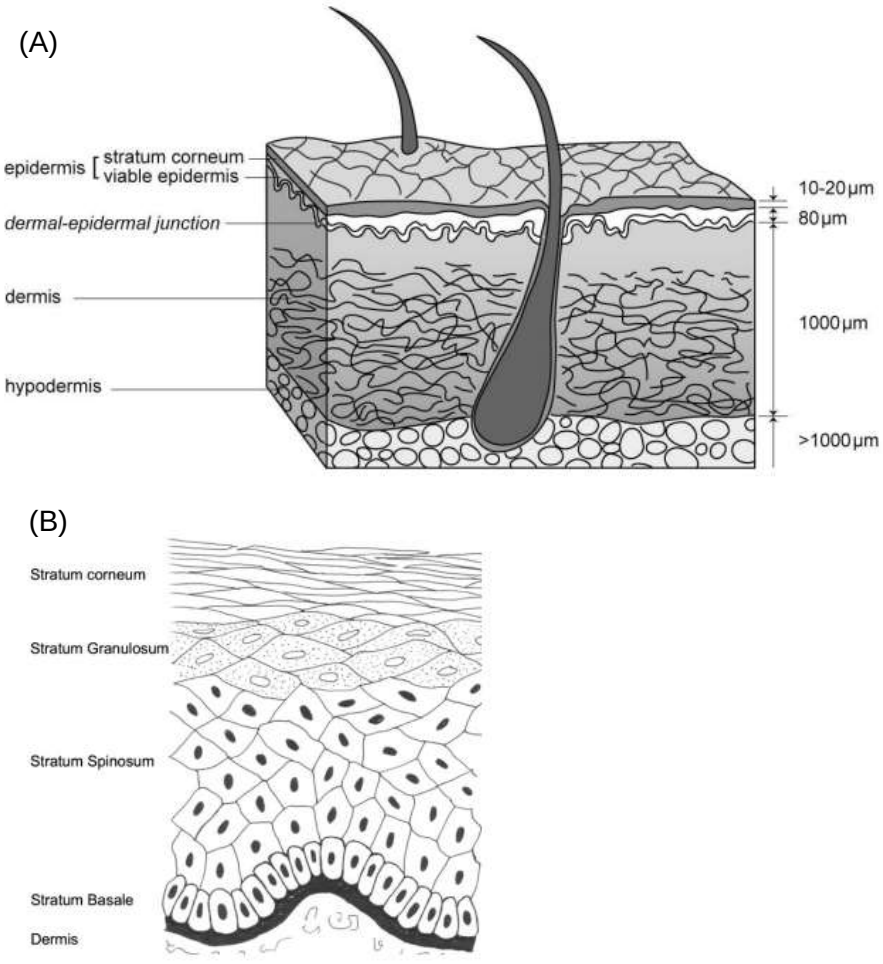

Figure 1-1 (A-B). Introduction into outer layers of skin structure (A) Schematic representation of different skin layers[1] (B) Diagram of the epidermis showing the main layers[2].

The outer skin layer is divided into three main parts: epidermis, dermis and hypodermis (subcutaneous tissue) (Figure 1-1 A). The epidermis in turn[3] is further divided into the basal layer or stratum basale, stratum spinosum, stratum granulosum and stratum corneum (the outermost skin layer) (Figure 1-1 B). The predominant cell type of the epidermis is the keratinocyte. Keratinocytes spread out from the basal layer to the granular layer, where they transform into the corneocytes of the SC. Keratin and many other proteins consist of keratinocytes. Keratins are the major structural proteins of the SC. The stratum granulosum (SG) consists of granules that appear in the cells at this layer in the epidermis. Although the SG is only a few cells thick, it is an important component of the epidermis. Some key transformations that help to form the SC barrier occur within the SG. Two types of granules are formed at the SG: protein-containing keratohyalin granules, and lipid-containing lamellar bodies (LB). In the SG, cells undergo transformation from keratinocytes into corneocytes, cells that form the SC. During this process, the nucleus in the keratinocytes is digested, the cytoplasm disappears, the lipids are released into the intercellular space, the keratin intermediate filaments aggregate to form microfibrils, and the cell membrane is replaced by a cell envelope made of cross-linked protein with lipids covalently attached to its surface. The resulting cells, corneocytes, are flat and assume the shape of either a hexagon or pentagon approximately 25 μm on a side with a surface area of approximately 1000 μm^2 and a thickness of approximately 0.5 to 1.0 μm.

1.1.2 Stratum corneum structure

Stratum corneum (SC) is the outermost layer of skin that protects the human body from exposure to the elements. It provides a protective barrier that regulates penetration of various exogenous substances and limits water loss. The layer beneath the SC is the viable

epidermis (VE). The SC structure is frequently depicted as a brick and mortar model (Figure 1-2), with the "bricks" representing the hydrophilic corneocytes and the "mortar" representing the hydrophobic lipids[3,4,5].

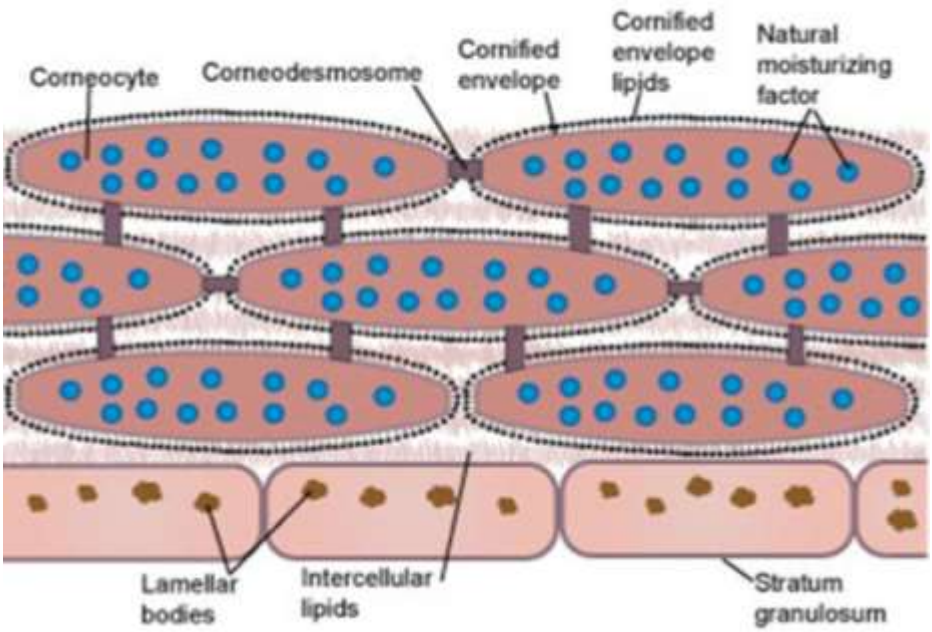

Figure 1-2. Stratum corneum "bricks and mortar" model[6] .

Corneocytes are terminally differentiated anucleated keratinocytes that have lost their nucleus and organelles. Lipid layers are formed from fatty acids and ceramides that are released from lamellar bodies located in the VE.

The SC is approximately 60% keratin by dry weight. Keratins are major structural proteins of skin, hair, and nail, and form a coiled-coil motif. At the SG, as keratinocytes are transformed into the corneocyte ''bricks,'' the coiled-coils aggregate to form structures called microfibrils, which are thought to lie parallel to the surface of the skin and serve to reinforce the corneocytes and limit SC swelling in the plane of the skin surface (Figure 1-3). Another important component of corneocytes is the NMF. NMF consists of lactate, amino acids and pyrollidone carboxylic acid (PCA) formed from the amino acid glutamine.

These natural moisturizers are needed to maintain proper hydration of the SC, allowing it to be flexible.

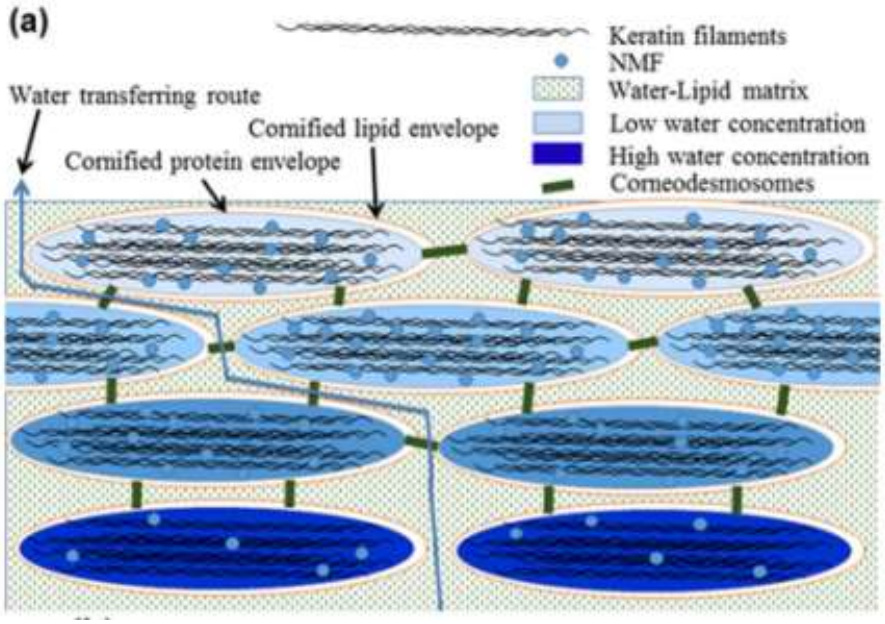

Figure 1-3. Schematic structure of the SC, corneocytes embedded in an intercellular matrix. Corneocytes consist of keratin fibers, NMF and water[7].

The lamellar bodies that appear at the SG contain lipids which are released into the intercellular space as the SC forms. These lipids are glucosyl ceramides, cholesterol, cholesterol esters, and long-chain fatty acids in an approximately equimolar ratio. The lipids spontaneously organize into multiple layers between the SC cells. This lipid ‘‘mortar’’ is critically important to the barrier function of skin. Lipids in the SC appear within the intercellular space of corneocytes. Organization of these lipids is essential in forming the protective barrier of the skin. The SC lipids are arranged in lamellar sheets that are stacked on top of each other between the corneocytes[8,9]. Two types of lipid lamellar phases are observed in the human SC and they are differentiated by their periodicities or repeat distances. The lipids in the long periodicity phase (LPP) have a repeat distance of approximately 13 nm. The short periodic phase (SPP) has a repeat distance of 6.4 nm [10,11].

A growing body of research work indicates that LPP lipids play an essential role in the barrier function of the skin[12]. The lipid packing within the lamellae defines the lateral organization[5] (see Figure 1-4 B); it further defines how close in space the lipid molecules are to each other. The packing is divided into three categories: liquid, hexagonal and orthorhombic (Figure 1-4 A,C). Lipids in the liquid state are conformationally disordered and loosely packed. Lipids become progressively more ordered and more densely packed in the hexagonal and orthorhombic phases. In healthy human skin, at physiological temperatures, lipids are mostly arranged in an orthorhombic phase with lesser amounts of hexagonal and liquid forms.

1.2 Stratum corneum permeation pathways

Two major skin permeation pathways exist: diffusion of substances through the SC and appendageal pathways via hair follicles or glands[15,16]. Based on the composition of SC there are two possible routes for diffusion through the skin: intercellular and intracellular[17]. In the intercellular route substances pass through the bilayer avoiding the corneocytes. Contrary to the assumption that this pathway takes longer than diffusion via corneocytes, it is actually relatively fast. The liquid crystalline structures of the lipid matrix allow it to form hydrophobic and hydrophilic domains, hence both hydrophobic and hydrophilic[17] materials can pass via this route. The transcellular pathway requires passing though both corneocytes and lipid bilayers. Diffusion through corneocytes is slower, which makes this pathway more difficult.

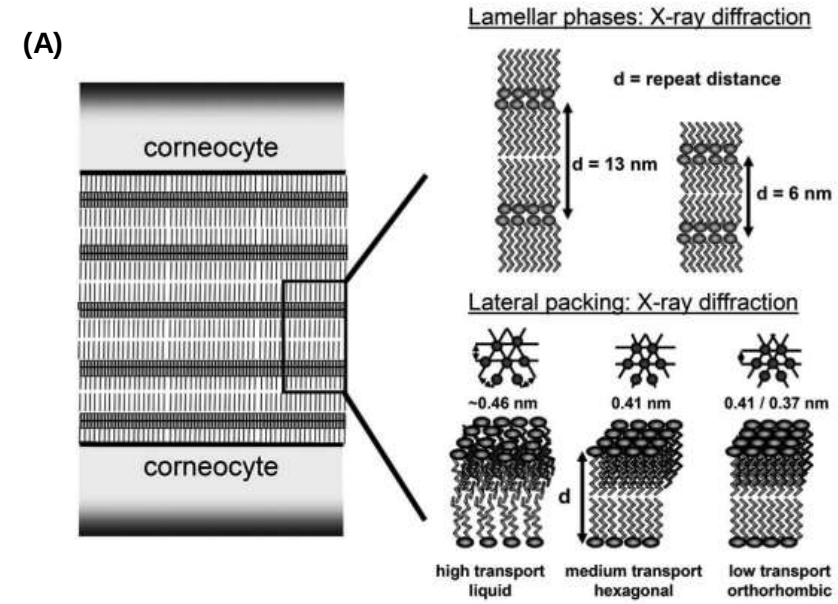

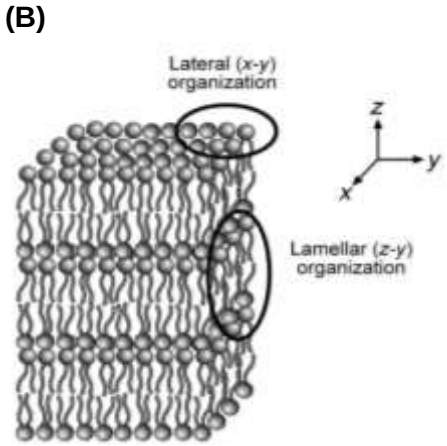

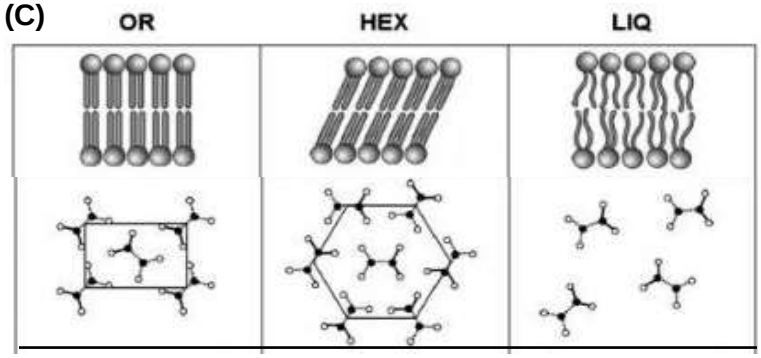

Figure 1-4 (A-C). Lipid organization and structure in a SC: (A) Lipid packing in human SC, lamellar phases and lateral packing; (B) Structure of lipid lamellae. The ovals indicate the lateral organization (i.e. the molecular packing in the plane of the lamellae, roughly parallel to the SC surface) and the lamellar organization (i.e. the symmetry and the repeat distance in the direction normal to the SC surface) of the lipids[13]; (C) Lipid matrix organization in the SC: OR – orthorhombic packing (best packed), HEX - hexagonal packing (less packing efficiency), LIQ - liquid packing (actually liquid crystal, disordered)[14].

The follicular route has received much attention, because this pathway has been shown to be important for percutaneous absorption and can be used for drug delivery[18,19].

Skin is routinely treated with various products, such as cosmetics or drug delivery formulations to treat diseases. In the case of cosmetic applications, the product is expected to stay on the surface of the skin, while topical pharmaceuticals are expected to permeate the skin barriers. Hence, understanding of the penetration mechanism is important as well as knowledge of which substances can enhance or impede permeation. The last class of materials are known as chemical penetration enhancers (CPEs).

There are different methods to measure diffusion of active agents into skin. The Franz diffusion cell (FDC)[20,21] is the most commonly used technique to measure skin permeation *in-vitro*[22]. Tape stripping methods are used for *in-vivo* measurements. With the most recent technological developments, there are various Raman techniques now available to measure substance penetration both *in-vitro* and *in-vivo*[23].

Human or pig skin is usually used in the FDC method. The skin sample is placed in the FDC filled with a buffer solution, oriented with the bottom of the skin facing the buffer, while the surface of the skin is treated with the product. The cell is sealed and incubated at a fixed temperature over time. At the appropriate time intervals, fluid is sampled for active material analysis.

The tape stripping used in the FDC method, as the name implies, uses an adhesive to remove sequential layers of skin. Each tape strip is expected to remove corneocytes layer by layer. However there are many disadvantages with this method[24,25]. First, upper layers of the SC form an irregular landscape filled with furrows and wrinkles. Therefore the first few tape strips remove SC of hills, followed by the SC of the furrows and

wrinkles[26]. This skews the accuracy of tracking of topically applied material. The depth penetration or thickness of the film is not very accurate. Second, the first strips might not remove any SC at all, but instead remove material that was applied topically. All this contributes to the fact that the number of removed strips might not correlate with the assumed depth[25].

1.3 Applications of vibrational spectroscopy to skin studies

Delivery of many topical pharmaceutical agents depends on their ability to penetrate the ordered lipid matrix of the SC and VE. Qualitative and quantitative studies of mechanisms of SC permeation by pharmaceuticals involve a variety of procedures, e.g. tape stripping, cutaneous microdialysis, liquid scintillation spectrometry and HPLC. The methods are destructive to the sample and sometimes are not particularly reliable [27,28,29]. For instance, HPLC offers very high sensitivity. However, the key criteria of the method are that the extraction process (sample preparation for HPLC analysis) does not degrade the drug, that the process is efficient and reproducible, and that it is free from interference from components of the SC and/or the tape adhesive[30]. Quantification of the drug in the combined tape-strips enables the total amount in the stratum corneum to be determined. HPLC suffers as it does not provide information about spatial distribution in the SC and VE of the active ingredient. As noted below vibrational spectroscopy techniques provide nondestructive, label-free measurements of spatial distribution in the skin in-vivo, ex-vivo or in-vitro.

Vibrational spectroscopy and imaging offer multiple advantages for a variety of dermatological applications, ranging from studies of isolated single skin cells (corneocytes) to characterization of endogenous components of intact skin or to

exogenous skin substances such as pharmaceuticals. In the current thesis the techniques of confocal Raman microscopy (CRM) and FTIR were used. CRM was used to map the depth-dependent permeation of the pharmaceutical agent flufenamic acid (FluA) into ex-vivo skin. In the second project, IR was used to evaluate structural perturbations of keratin and lipids caused in the SC by the antifungal agent terbinafine. In the third project, CRM was used to compare a novel advanced NMF moisturizer with a commercially available product.

Raman spectroscopy is based on the generation of inelastically scattered light by sample molecules illuminated with a laser source. The effect allows for study and identification of vibrational states of molecules. The technique is a valuable analytical tool for molecular finger printing as well as for monitoring changes in molecular structure, while IR is better for monitoring changes in molecular structure such as physical state changes, e.g., the orthorhombic→hexagonal transition in lipids and protein denaturation[5,14]. In comparison to the other analytical techniques for studying skin, FT-IR and Raman spectroscopy offer several major advantages. Since the Raman effect is the result of light scattered from a sample as opposed to the light absorbed by a sample, the approach requires little to no sample preparation. As opposed to FTIR, Raman does not suffer from significant interference from the water present in the sample. These properties of Raman facilitate the measurement of solids, liquids, and gases not only directly, but also through transparent containers such as glass, quartz, and plastic.

Similar to FT-IR, Raman spectroscopy is highly selective, which allows it to identify and differentiate molecules that are very alike. Many molecules with related chemical structures have clearly different Raman spectra.

FTIR advantages compared with Raman include higher precision, because of the He-Ne laser used to mark the interference fringes in the spectrometer. In addition, IR spectra may be obtained at much higher signal/noise levels than Raman spectra, permitting the tracking of much smaller spectral changes.

1.4 Confocal Raman microscopy

In older Raman microscopy instruments, a large amount of elastically scattered light was generated, because the whole sample had to be illuminated at once. Reducing the scattered light via insertion of confocal masks is the basis of the design for confocal Raman instruments. In confocal microscopy, scattered light from unwanted sample regions is minimized, thus preventing it from entering the microscope objective. This is achieved by examining each point of the specimen sequentially and measuring the amount of light scattered or absorbed just by that point. This is realized firstly by a point illumination in the focal plane and secondly by a pinhole in the conjugate plane of the detection beam path Figure 1-5(B). Due to the point illumination and detection, only information from a single point is determined at a time. To generate data for an image, the sample is scanned point-by-point and line-by-line. The advantages of confocal microscopy over conventional wide-field microscopy include improved resolution, high discriminatory power, reduced background signal, and the ability to collect from different focal planes to generate depth

(A)

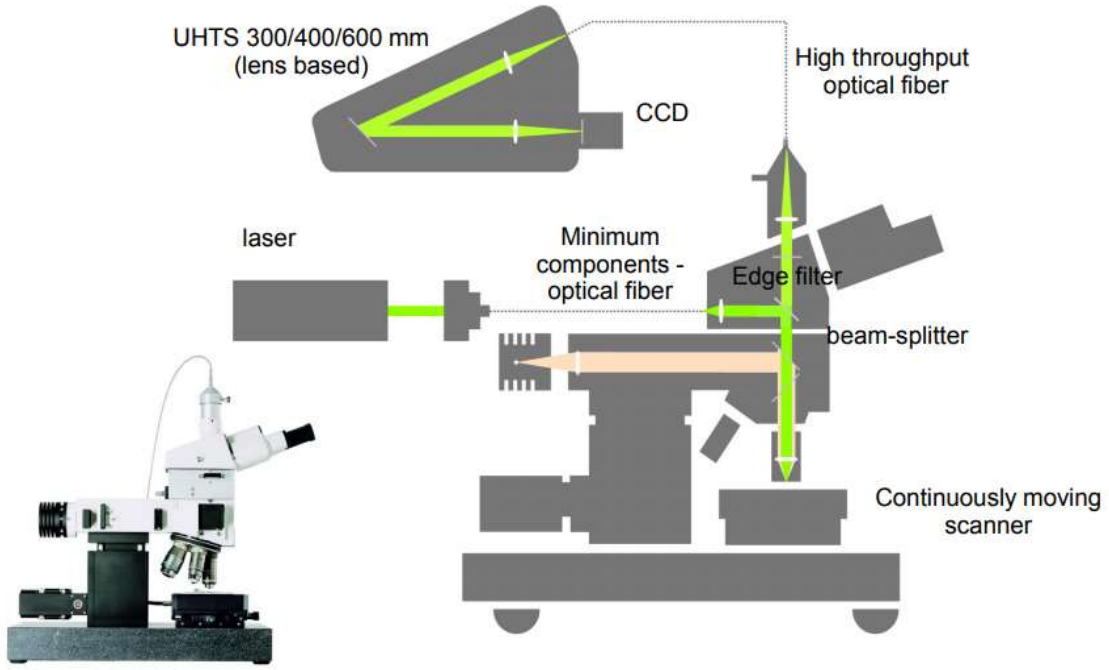

(B)

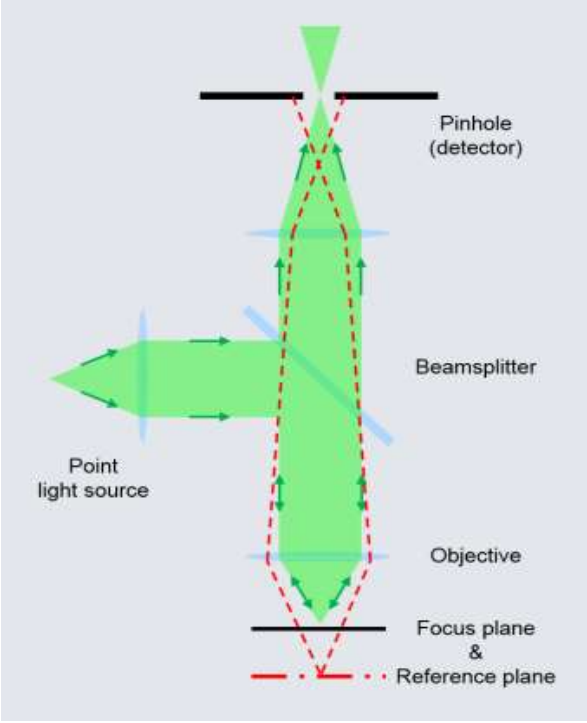

Figure 1-5 CRM instrument set up (A) Setup and beam path of WITec Raman confocal microscope (B) Principles of confocal microscopy of WITec instrument.

Confocal Raman spectroscopy in the current study permits in depth imaging of the distribution of pharmaceutical agents with ~1micron spatial resolution at depths up to ~ 60 μm.

WITec has developed a confocal Raman microscopy system that features an excitation laser coupled to a microscope[31] with a single mode optical fiber, Figure 1-5(A). The latter provides a Gaussian beam profile that can be focused to a diffraction-limited spot size. The laser beam is reflected by a holographic beamsplitter and focused onto the sample with a microscope objective, while the sample is scanned with a piezoelectric scan table. The same objective collects the Raman-scattered light, and an extremely steep edge filter suppresses reflected laser and Rayleigh-scattered light. The scattered light is then focused into a multimode optical fiber in which the fiber core (100 μm, 50 μm, or 25 μm) acts as a pinhole for confocal microscopy. The multimode fiber is coupled to a spectrometer with a CCD camera for Raman spectral imaging. The core of the multimode fiber also acts as an entrance slit for the spectrometer. with a single mode optical fiber. Combining confocal microscopy with Raman spectroscopy techniques provides a powerful tool for materials analysis.

1.4 References:

1. Geerligs, M., "Skin layer mechanics", Eindhoven: Technische Universiteit Eindhoven **2010**, DOI: 10.6100/IR657803.

2. Wickett, R.R., "Structure and function of the epidermal barrier", *Am J Infect Control*, **2006**, 34, pp. S98-S110.

3. Proksch, E., Brandner, J.M., Jensen, J.-M., "The skin: an indispensable barrier", *Experimental Dermatology*, **2008**, 17 (12), 1063-1072.

4. Baroni, A., et.al., "Structure and function of the epidermis related to barrier properties", *Clinics in Dermatology*, **2012**, 30(3), pp. 257-262.

5. Boncheva, M., "The physical chemistry of the stratum corneum lipids", *International Journal of Cosmetic Science*, **2014**, 36, pp. 505–515.

6. Hames, S.C., "Segmentation of skin strata in reflectance confocal microscopy depth stacks", **2015**, *Proc. SPIE 9413, Medical Imaging 2015: Image Processing*, 94131U (20 March 2015); doi: 10.1117/12.2081737; https://doi.org/10.1117/12.2081737.

7. Choe, C., Schleusener, J., Lademann, J., Darvin, E.M.**,** "Keratin-water-NMF interaction as a three layer model in the human stratum corneum using in vivo confocal Raman microscopy", , *Scientific Reports*, **2017**, 7, pp.15900-16002.

8. Janssens, M., van Smeden J., Gooris, G.S., Bras, W., Portale G., Caspers, P.J., Vreeken, R.J.,, Hankemeier, T., Kezic, S., Wolterbeek, R., Lavrijsen, A.P., Bouwstra, J.A., "Increase in short-chain ceramides correlates with an altered lipid organization and decreased barrier function in atopic eczema patients", *Journal of lipid research*, **2012**, 53(12), pp.2755-2766.

9. Thakoersing, V.S., Gooris, G., Mulder, A.A., Rietveld, M., El Ghalbzouri, A., Bouwstra, J.A., "Unrevelling barrier properties of three different in-house human skin equivalents", *Tissue engineering. Part C, Methods*, **2012**,18(1), pp.1-11.

10. Janssens, M., van Smeden, J, Gooris, G.S., Bras, W., Portale, G., Caspers, P.J., Vreeken, R.J., Kezic, S., Lavrijsen, A.P., Bouwstra, J.A. , "Lamellar lipid organization and ceramide composition in the stratum corneum of patients with atopic eczema", *The Journal of investigational dermatology*, **2011**, 131(10), pp. 2136-2138.

11. White, S.H., Mirejovsky, D., King, G.I., "Structure of lamellar lipid domains and corneocyte envelops of murine stratum corneum", *Biochemistry*, **1988**, 27(10), pp. 3725-3732.

12. Groen, D., Poole, D.S., Gooris, G.S., Bouwstra, J.A., "Is an orthorhombic lateral packing and a proper lamellar organization important for the skin barrier function?", *Biochimica et biophysica acta*, **2011**, 1808(6), pp.1529-1537.

13. Bowstra, J., Gooris, G.S., Janssens, M, Bouwstra, J.A.., "The Lipid Organization in

Human Stratum Corneum and Model Systems", *The Open Dermatology Journal*, **2010**, 4, pp.10-13.

14. Boncheva, M., Damien, F., Normand, V., "Molecular organization of the lipid matrix in intact Stratum corneum using ATR-FTIR spectroscopy", *Biochimica et Biophysica Acta (BBA) - Biomembranes*, **2008**, 1778(5), pp.1344-1355.

15. Lademann, J., Richter,. H., Teichmann, A., Otberg, N., Blume-Peytavi, U., Luengo, J., Weiss, B., Schaefer, U.F., Lehr, C.M., Wepf, R., Sterry, W., "Nanoparticles – An efficient carrier for drug delivery into the hair follicles", **2007**,*European Journal of Pharmaceutics and Biopharmaceutics*, **2007**, 66(2), pp.159-164.

16. Knorr, F., Lademann, J., Patzelt, A., Sterry, W., Blume-Peytavi, U., Vogt, A., "Follicular transport route – Researchprogress and future perspectives", *European Journal of Pharmaceutics and Biopharmaceutics*, **2009**, 71(2), pp.173-180.

17. Gonzalez, H., "Percutaneous absorption with emphasis on sunscreens", **2***Photochem. Photobiol. Sci*., **2010**, 9(4), pp.482-488.

18. Lademann, J., Otberg, N., Richter, H., Weigmann, H.J., Lindemann ,U., Schaefer H, Sterry, W., "Investigation of follicular penetration of topically applied substances", *Photochem. Photobiol. Sci*., **2001**, 14(1), pp. 17-22.

19. Lademann, J., Richter, H., Teichmann, A., Otberg, N., Blume-Peytavi, U., Luengo, J., Weiss, B., Schaefer, U.F., Lehr, C.M., Wepf, R., Sterry, W., "Nanoparticles – An efficient carrier delivery into the hair follicles", *European Journal of Pharmaceutics and Biopharmaceutics*, **2007**, 66(2), pp.159-164.

20. Kasting, G.B., Bhatt VD, Speaker TJ.., "Microencapsulation decreases the skin absorption of N, N-diethyl-m-toluamide (DEET)", *Toxicology in Vitro*, **2008**, 22(2), pp.548-552.

21. Ross, J.S., Shah, J.C., "Reduction in skin permeation of N,N-diethyl-m-toluamide (DEET) by altering the skin/vehicle partition coefficient", *Journal of Controlled Release*, **2006**, 67(2-3), pp.211-221.

22. Santhanam, A., Miller, M.A, Kasting, G.B., "Absorption and evaporation of N,N-diethyl-m-toluamide from human skin in vitro", *Toxicology and Applied Pharmacology*, **2005**, 204(1), pp.81-90.

23. Pot, L.M., Coenraads, P.J., Blömeke, B., Puppels, G.J., Caspers, P.J., "Real-time detection of p-phenylenediamine penetration into human skin by in vivo Raman spectroscopy", *Contact Dermatitis*, **2016**, 74(3), pp. 152-158.

24. Bashir, S.J., "Physical and physiological effects of stratum corneum tape stripping", *Skin research and technology: official journal of International Society for Bioengineering and the Skin (ISBS) [and] International Society for Digital Imaging of Skin (ISDIS) [and' International Society for Skin Imaging (ISSI)*, **2001**, 7(1), pp. 40-48.

25. Jacobi, U.,Weigmann, H.J, Ulrich, J., Sterry, W., Lademann, J., "Estimation of the relative stratum corneum amount removed by tape stripping", **2005**, *Skin research and technology: official journal of International Society for Bioengineering and the Skin (ISBS) [and] International Society for Digital Imaging of Skin (ISDIS) [and] International Society for Skin Imaging (ISSI)*, 11(2), pp. 91-96.

26. Lademann, J., "In vivo methods for the analysis of the penetration of topically applied substances in and through the skin barrier", *Int J Cosmet Sci*, **2012**, 34(6), pp.551-559.

27. Franz T.J., Lehman, P.A, Raney, S.G.., "Use of excised human skin to assess the bioequivalence of topical products", *Skin Pharmacol Physiol*., **2009**, 22(5), pp.276–286.

28. Yang Y., " Development and validation of in vitro-in vivo correlation (IVIVC) for estradiol transdermal drug delivery systems", *J Control Release*., **2015**, 210, pp.58–66.

29. Ruela, A. L. M., Perissinato, A.G.., Mudrik, P.S., Pereira, G.R., "Evaluation of skin absorption of drugs from topical and transdermal formulations", **2016**, *Brazilian Journal of Pharmaceutical Sciences*, 52(3), pp.527-544.

30. Herkenne, C., "*In Vivo* Methods for the Assessment of Topical Drug Bioavailability", **2008**, *Pharm Res.***,** 25(1), pp. 87–103.

31. Hollricher, O., "Confocal Raman microscopy teams high-resolution capabilities with powerful materials analysis", **2003**, *Spie's oe magazine*, 11, pp.16-20.

Chapter 2: Effects of Permeation Enhancers On Flufenamic Acid Delivery In Ex Vivo Human Skin By Confocal Raman Microscopy

2.1 Introduction

The outermost layer of human skin the SC provides an essential protective barrier minimizing the penetration of exogenous substances and inhibiting water loss from the body. A simplified structure of the SC is often portrayed as a brick and mortar model with keratin-filled corneocytes embedded in a lipid matrix[1]. The barrier properties of the SC predominantly reside in the highly ordered lipid matrix and poses major challenges for topical delivery of therapeutic agents. The SC lipid barrier must be crossed when permeation takes place by either intercellular or transcellular pathways.

Delivery of many topical pharmaceutical agents depends on their ability to penetrate the ordered lipid matrix of the SC and VE. Structural factors such as lipid packing or the presence of chemical penetration enhancers (CPEs) in the formulation can significantly affect the bioavailability of pharmaceutical substances in skin. A frequently used approach for successful drug delivery via the SC is the use of CPEs that alter the permeability properties of the barrier, such as lipid fluidization and keratin denaturation [2,3]. Many CPEs reversibly affect keratin α-helical structure by introducing β-sheet structures, thus making a more accessible transient passage of active ingredients. Other effects of CPEs on SC include lipid fluidization, thus changing the solubility properties of the SC barrier.

In this study[4], flufenamic acid (FluA) is used as the lipophilic model drug (Figure 2-1) to investigate the influence of hydrophilic versus hydrophobic permeation enhancers on its penetration and spatial distribution in ex vivo human skin. FluA is a common anti-inflammatory product that can be administered orally or topically[5]. Topical applications

are advantageous as side effects of first pass metabolism are significantly reduced[1,2,3]. Earlier studies investigated the interrelationship between penetration and permeation of lipophilic FluA in human skin and skin equivalents[6]. An evaluation of in vivo/ in vitro correlations of FluA delivery[7] led to a predictive method for in vivo penetration into deeper skin layers based on in vitro experiments. More recent work has focused on various delivery systems for FluA ranging from gel[8] and micellar formulations[9] to microemulsions[10,11]. The goal of the last two studies was to limit the irritation potential of the enhancers.

In the current work, confocal Raman microscopy was used to obtain xz (z=depth) images of the spatial distribution as well as relative concentration of FluA in the SC and VE. This approach is nondestructive and allows the observation of multiple components simultaneously without the use of probe molecules. Information inherent in the spectra also permits a detailed look at perturbations to skin regions with ~1 micron spatial resolution and changes in the molecular structure of particular endogenous constituents. Although many studies focus on the sensitive quantification of exogenous agent penetration utilizing sequential tape stripping and/or segmentation of skin regions followed by chemical analysis (e.g. HPLC or radioactivity), important information regarding the lateral spatial distribution of exogenous materials is lost. Visualization of the excipient and drug distribution relative to the microstructure and perturbation of the skin provides valuable mechanistic insight regarding transport pathways. Over the past decade, confocal Raman microscopy has evolved to become an important approach providing a better understanding of percutaneous drug delivery[12-18] .

The SC and VE regions of skin have distinct vibrational modes (Figure 2-1 A-B). The following vibrational frequencies are of interest in the current work: OH stretching (3100-3800) cm^{-1} from water in the skin, CH symmetric stretching 2850 cm^{-1}, CH asymmetric stretching 2880 cm^{-1} from CH_2 and CH_3 groups in the sample lipids, as well as CH_3 symmetric stretching at 2930 cm^{-1} from the protein side chains present in the sample, Amide I (peptide bond C=O stretch from keratin and other proteins) band at 1655 cm^{-1}. The following frequencies were also monitored from the indicated chemical species: FluA which has aromatic C=C stretching modes at 1618 cm^{-1} and CD stretching from deuterium labeled CPEs at 2110 cm^{-1}. CPE solutions were labeled with deuterium to trace their location in the skin.

2.2 Materials and methods

2.2.1 Materials

The following chemicals and reagents were used in the experiments: flufenamic acid (FluA) (Fluka, USA), n-octyl-d17-alcohol (Oct-d) (CDN Isotopes, Canada), 1.2-propanediol-D6 (PG-d) (Cambridge Isotope Laboratories, USA), ethanol-D6 (Et-d) (Aldrich, USA).

Human abdominal skin from plastic surgery was obtained from dermatological offices with informed consent and ethics board approval from each office. Skin sections were wrapped in aluminum foil, fast frozen with liquid nitrogen and stored at –20°C for no more than six months, prior to usage.

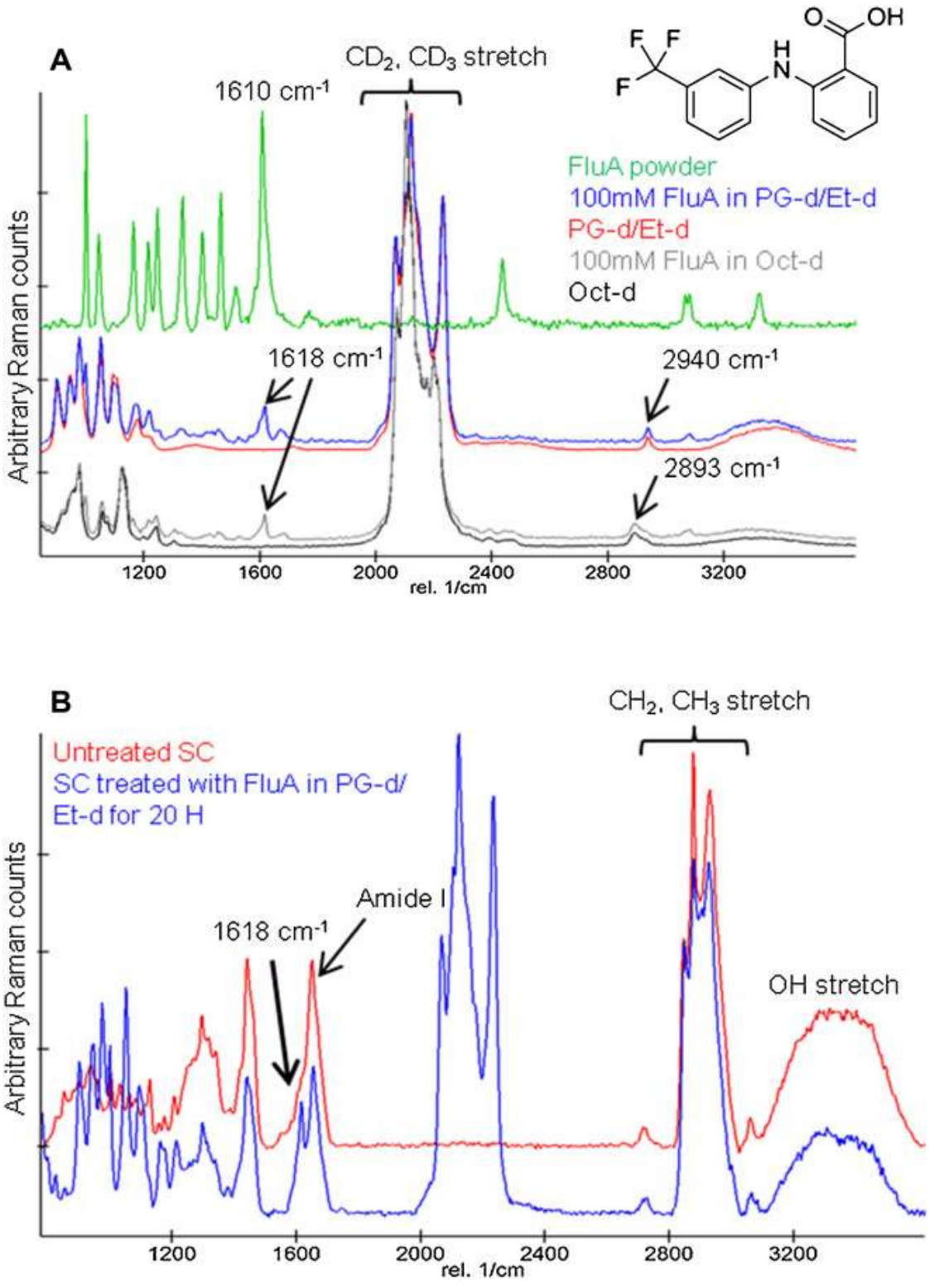

Figure 2-1. Typical Raman spectra of formulation components, as well as treated and untreated SC. (A) Flufenamic acid powder (green), PG-d/Et-d (75:25, v/v) solvent (red), Oct-d solvent (black), 100 mM FluA in PG-d/Et-d (blue), 100 mM Flu Oct-d (grey). (B) untreated SC (red), SC treated with 100 mM FluA in PG-d/Et-d (blue).

2.2.2 Methods

Sample preparation

100mM FluA was prepared in either Oct-d or PG-d/Et-d (25:75) solution. Since FluA was not soluble in the hydrophilic enhancer PG-d, Et-d was added to the mixture to improve solubility. For ex-vivo experiments, a piece of full thickness skin (~3-4 mm) was cut about 1.5x1.5 cm^2 and defrosted. The skin surface was cleaned with cotton swabs and deionized water to remove any excess of sebum. A Franz diffusion cell (FDC) was used for skin incubations, which were done at 34°C for 6 and 20 hours. The donor compartment of FDC was filled with distilled water to keep skin hydrated, while the receptor compartment was filled with 50uL of applied relevant skin treatment. To keep skin viable during Raman measurements, it was placed into a specially designed brass Raman cell (figure 2-2). Skin was positioned on the fine metal mesh, on top of the well filled with water to keep skin hydrated. Skin was covered and sealed with glass slip.

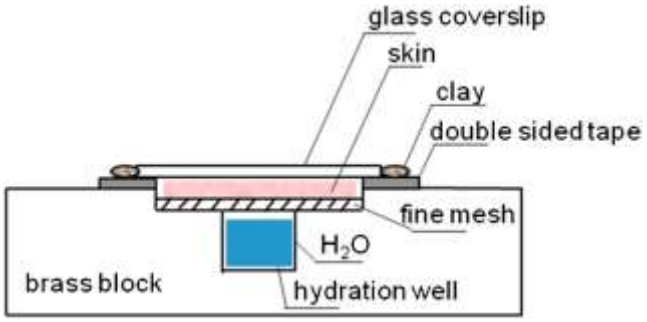

Figure 2-2. Cross section schematic of the homemade sample holder used to acquire Raman skin images. Two circular concentric wells were milled into a brass block to accommodate water and full thickness skin with diameters of approximately 7 and 16 mm and depths of approximately 7 and 1.5 mm, respectively. The lateral dimensions of the block are the same size as a typical glass slide.

Raman measurements and analysis

Raman skin imaging was accomplished by using a WITec Alpha-300R Plus confocal Raman microscope (Ulm, Germany) equipped with a 532 nm laser and a 100X

oil immersion objective (NA 1.25). Measurements were performed at room temperature (RT) with laser power of 20 mW for Oct-d treated skin experiments and 10 mW for PG-d/Et-d treatments. Data acquisition and analysis were completed using WITec Project Plus 4.1 software. Images were collected in the XZ plane (skin depth profiles) with size of the maps 100 x 60 μm^2, using 2 μm steps and a 10 s integration time.

Cosmic ray removal and baseline correction (size of 120 and noise factor of 1) were part of the initial data treatment in Project Plus data acquisition software. The integrated area of peaks (sum) and intensity at peak maxima (max) were generated and ratios of various parameters were used to obtain the relative concentration of endogenous and exogenous components. Table 2-1 lists wavenumbers for chemical bonds of interest.

Table 2-1. List of Raman wavenumber ranges used for data processing and treatment.

Chemical bond and vibrational mode	**Wavenumber Range, cm^{-1}**
OH stretching sum	3083.9-3675.4
CH stretching sum	2809.3-3019.3
CD stretching sum	1941.2-2341.2
Amide I max	1629.5-1676.1
FluA C=C max	1602.8-1627.8

Images with relative FluA were measured from FluA C=C peak/Amide I peak intensity ratio. Relative enhancer concentrations were measured from the integrated area of the CD stretching region/CH stretching region ratio. The relative water concentration was obtained from the integrated area of the OH stretching band/CH stretching region ratio.

In addition to that, cluster analysis (k-means without background, Euclidean normalization and distance mode with a minimum number of clusters) was used to differentiate the SC from viable epidermis (VE) and to delineate the SC from viable epidermis (VE). Based on cluster analysis, a binary mask was generated, as well as an average spectrum for each cluster. Upon application of these to images of the parameters specified above, the statistics option offered by WITec Project Plus software was utilized to provide evaluation of various spectral parameters for skin regions. For particular qualitative spectral comparison, spectra were normalized to Amide I peak height.

2.3 Results

2.3.1 Confocal Raman evaluation of FluA and CPE penetration

Raman spectra of FluA crystalline powder, the CPEs used in this study and the FluA solutions are shown in Figure 2-1 (A). The most intense band in the FluA spectrum observed at 1610 cm^{-1} arises from aromatic C=C stretching modes. It is a convenient marker for FluA detection in the ex vivo skin penetration experiments. This band broadens and shifts to a higher frequency (1618 cm^{-1}) once FluA is dissolved. The CD_2 and CD_3 stretching contour is easily distinguished from endogenous CH skin lipid bands and is used to track delivery vehicle (CPE) penetration into the skin. Weak residual CH stretching bands are noted in the spectra of the solvents at 2940 and 2893 cm^{-1} due to incomplete deuteration. Figure 2-1 (B) shows a typical spectrum of untreated SC overlaid with a SC spectrum where the intact skin was incubated with FluA in PG-d/Et-d for 20 H. Characteristic skin bands, such as Amide I (1650 cm^{-1}), CH_2, CH_3 stretch (2800-3000 cm^{-1}) and OH stretch (3100-3600 cm-1), noted in the figure, were used to monitor changes in keratin structure, endogenous lipid acyl chain order and levels of hydration, respectively,

in the skin sections. In addition the C=C stretching band (1618 cm^{-1}) due to FluA that has penetrated into the skin is marked and is used to evaluate relative FluA concentration profiles under various treatment conditions.

Images of relative FluA and vehicle concentration for untreated, vehicle only treated, and 6 vs 20 H FluA treatment (Figure 2-3, A, B and Figure 2-4 A, B) demonstrate

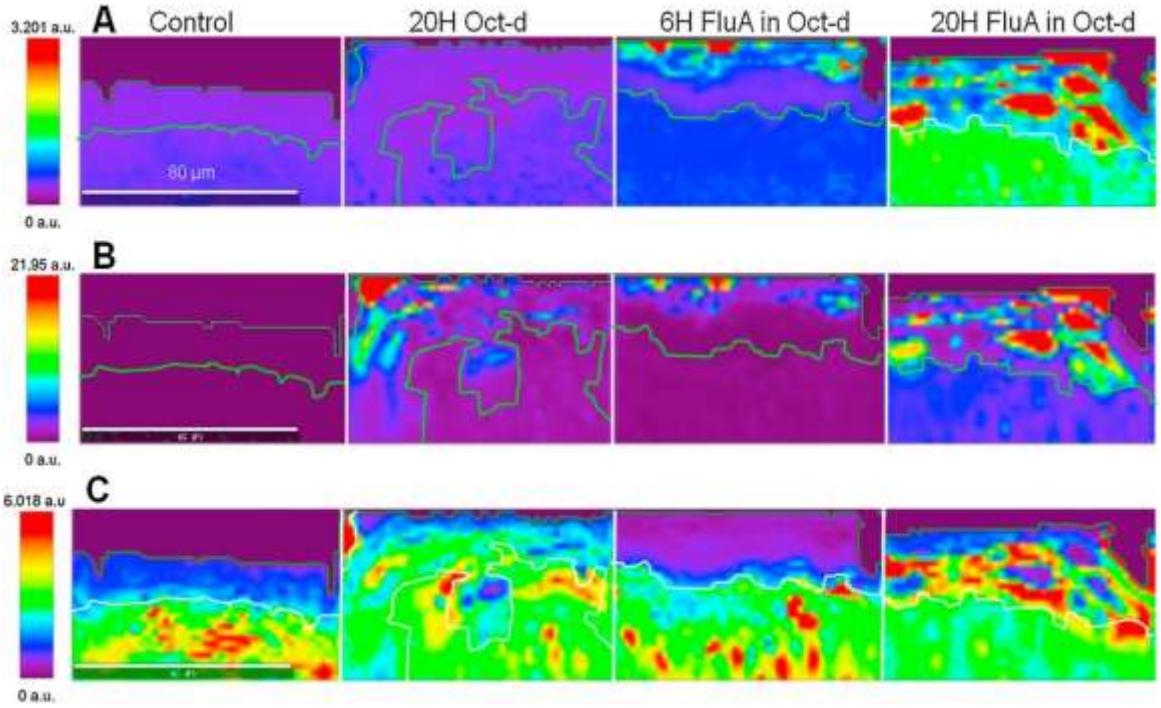

Figure 2-3. Confocal Raman image planes of relative concentrations of FluA, Oct-d and water in skin samples. Images are shown (left to right) for control (untreated), placebo (20H incubation with Oct-d) and 6H versus 20H incubation periods for 100 mM FluA in Oct-d treated skin. The upper and lower SC boundaries are outlined. (A) Images of relative FluA concentration as measured by the FluA C=C peak/Amide I intensity ratio; (B) relative Oct-d concentration as measured by the integrated area of the CD stretching region/area of the CH stretching region ratio; (C) relative water concentration as measured by the integrated area of the OH stretching band/area of the CH stretching region ratio. For data analysis details see Materials and Methods section. The scale bar of 80 µm applies to both x and z directions in all images. The ranges of the color scale bars were chosen to highlight differences within the four images shown for each spectral parameter.

the temporal and spatial distribution of the exogenous agents in skin. To compensate for confocal losses of signal intensity with depth, the relative concentration of FluA is

monitored via the intensity ratio of the FluA C=C stretching band (~1618 cm^{-1}) to the Amide I intensity at ~1650 cm^{-1} (Figure 2-3 A and Figure 2-4 A). The relative concentration of CPE is measured as the ratio of the integrated area of the CD stretching region over the integrated area of the CH stretching region (see Materials and Methods for details) as shown for both vehicles in Figures 2-3 B and 2-4 B.

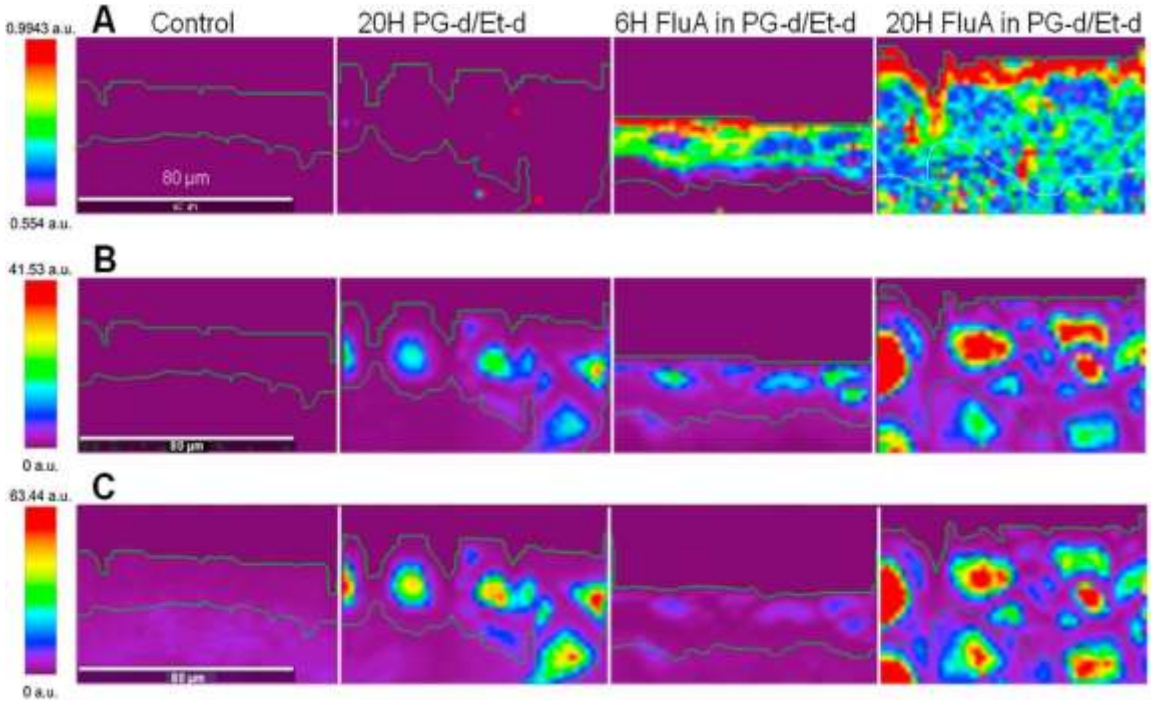

Figure 2-4. Confocal Raman image planes of relative concentrations of FluA, PG-d/Et-d and water in skin samples. Images are shown (left to right) for control (untreated), placebo (20H incubation with PG-d/Et-d) and 6H versus 20H incubation periods for 100 mM FluA in PG-d/Et-d treated skin. The upper and lower SC boundaries are outlined. (A) Images of relative FluA concentration as measured by the FluA C=C peak/Amide I intensity ratio; (B) relative PG-d/Et-d concentration as measured by the integrated area of the CD stretching region/area of the CH stretching region ratio; (C) relative water concentration as measured by the integrated area of the OH stretching band/area of the CH stretching region ratio. For data analysis details see Section 2. The scale bar of 80 µm applies to both x and z directions in all images. The ranges of the color scale bars were chosen to highlight differences within the four images shown for each spectral parameter.

Relative concentrations of FluA and Oct-d (Figure 2-2 A and B, respectively) in the SC and VE regions of skin display time-dependent increases with a notable spatial distribution. After 6 H of incubation, small (≤ 20 μm^2) discrete pockets of Oct-d are observed in the

upper SC layers which grow in number, size and depth with incubation time (figure 2-3 B). In a parallel manner, the spatial distribution of FluA appears to co-localize with Oct-d in the SC. The heterogeneous distribution of FluA in the SC (20 H incubation) is contrasted by a more homogeneous distribution in the VE. Somewhat surprisingly, the relative FluA concentration outside the Octanol-d rich pockets in the SC is lower than that observed throughout the VE. A similar set of images (Figure 2-3 C and Figure 2-4 C) display the spatial distribution of the relative water content in these samples as deduced from the ratio of the area of the OH stretching band to the CH stretch as described above. A relatively low water content typically observed in the SC is evident in the untreated and 6 H FluA image (1st and 3rd images in Figure 2-3 C, purple and dark blue regions). In contrast, this profile is greatly perturbed for both Oct-d 20 H treatments (2nd and 4th images in Figure 2-3 C) where several regions with high (red) relative water content are observed. The regions with high water content are complementary to the spatial distribution of Oct-d inclusions.

The relative concentration of FluA, delivered from PG-d/Et-d, and the hydrophilic agent itself, also display time-dependent increases in the SC (Figure 2-4 A and B, respectively), although the spatial distributions of the active versus vehicle significantly differ (i.e. co-localization of FluA and enhancer is not observed). For both incubation periods, the highest concentration of FluA is detected in the upper SC layers whereas relatively high concentrations of the vehicle are observed to develop in the spatially segregated, discrete domains ($\geq$ 20 μm^2) throughout the sampled skin regions. Compared to maps of the vehicle distribution (Figure 2-4 B), the images shown in Figure 2-4 A of 6 and 20 H FluA treatment are somewhat complementary, i.e., regions with highest vehicle concentrations generally have lower FluA concentrations. Inspection of the CD stretching

region in the Raman spectra of the two pure components used in the delivery vehicle (see Figure 2-1 A) compared to spectra within the pockets of high concentration in the skin reveals that the majority of the Et-d has evaporated during the incubation period or (alternatively) rapidly penetrated to deeper, unmeasured skin regions. In addition, the thickness of the SC swells following 20 H incubation and, in contrast to the distribution of Oct-d, discrete solvent pockets are also observed in the VE. Images of the relative water content depicted in Figure 2-4 C for the 20 H PG-d/Et-d treatments show a significant increase in water content in the skin compared to the 20 H Oct-d treated sections (compare range on the scale bars in Figures 2-4 C to 2-3 C).

The average values of the relative concentration of FluA in the SC and VE are compared for duplicate experiments in Figure 2-5 and help in the assessment of FluA uptake in skin. The levels shown for two control (untreated) skin sections provide a baseline value of ~0.45 which results from the inherent width of the Amide I band. The incubation time and the delivery vehicle significantly influenced the observed concentration of FluA. For the 20 H incubation, higher concentrations of FluA with Oct-d were observed in the SC and VE compared to PG-d/Et-d delivery. Large SD's in the SC for Oct-d reflect the variability of FluA concentration in and out of Oct-d inclusions which is clearly evident in Figure 2-3 (A) for the 20 H incubation image. Much smaller differences between vehicles were observed in the two skin regions for the 6 H incubation experiments where somewhat higher than baseline FluA values are noted.

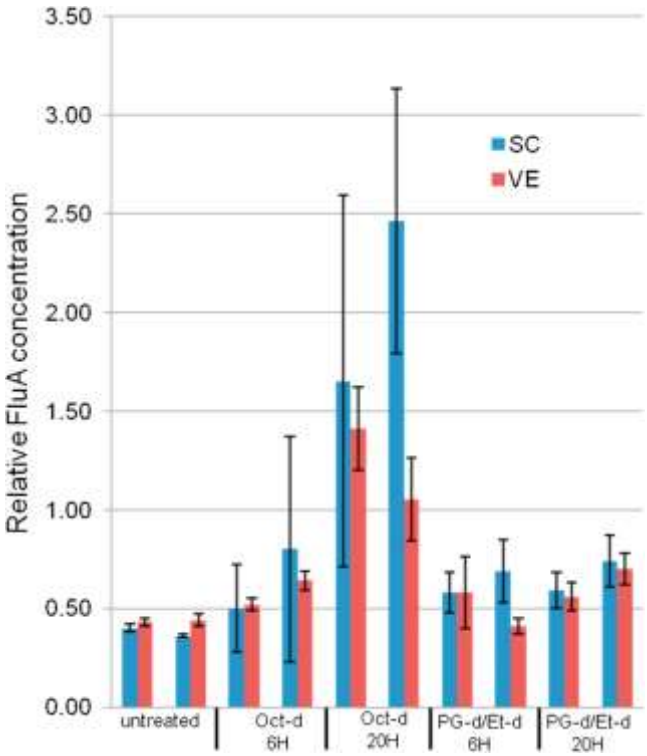

Figure 2-5. Relative FluA concentration in SC (blue bars) and VE (red bars) for duplicate experiments under various conditions. The error bars show ± 1SD and predominantly reflect the variability of FluA concentration in and out of solvent inclusions. The baseline values for untreated skin (~0.45) are apparent in the leftmost two datasets.

2.3.2 Molecular structure/composition changes upon treatment

Sets of overlaid spectra in the CH and OH stretching region are displayed in Figure 2-6 (A-D) to probe potential mechanisms of SC perturbation leading to penetration of the exogenous materials. The spectra were chosen from the regions marked in each inset image of relative solvent concentration. Spectra are color-coded and were selected from areas outside (blue and purple) and within (red and pink) the solvent inclusions for each of the materials. The spectra were chosen from the regions marked in each inset image of relative solvent concentration.

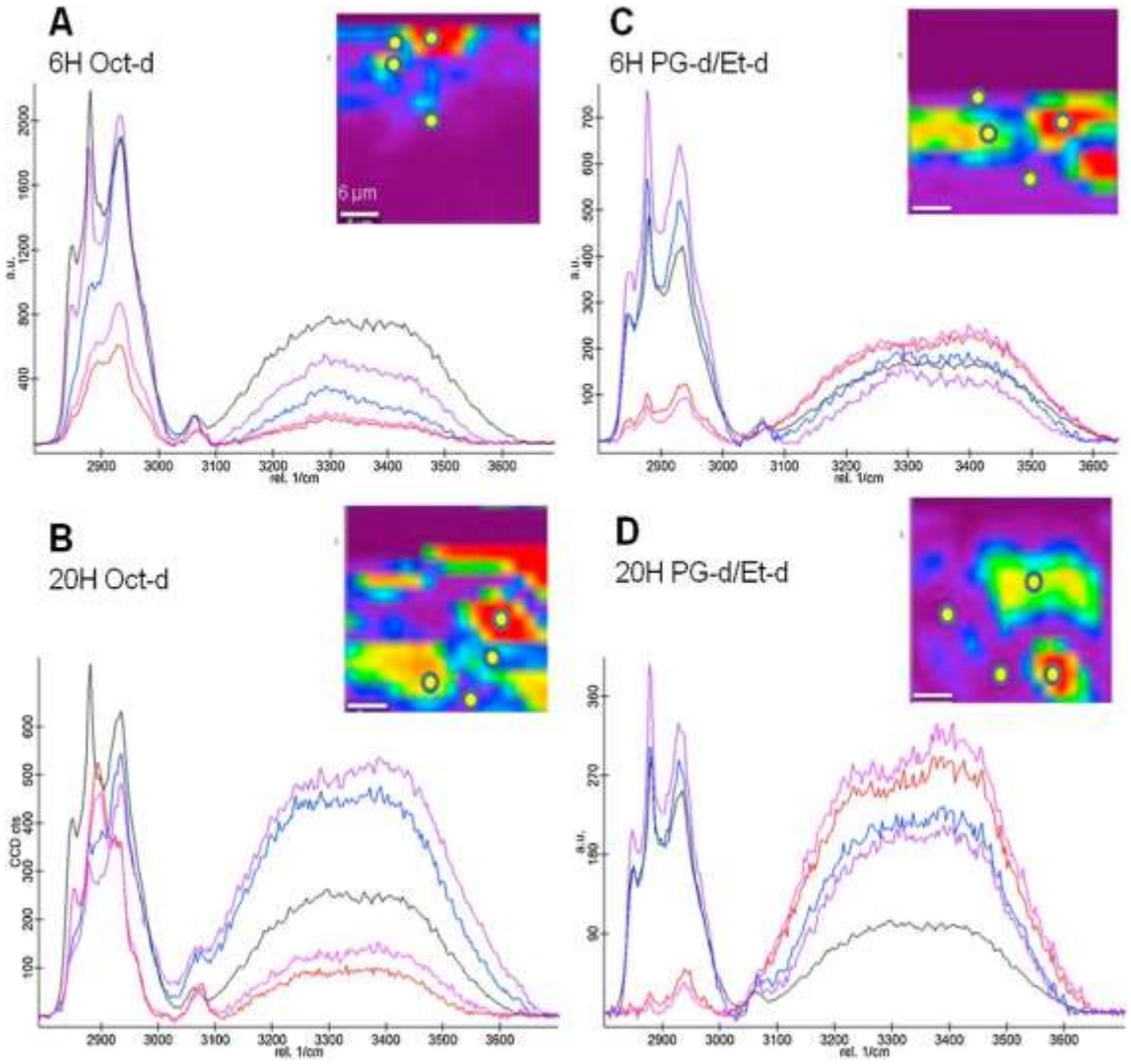

Figure 2-6. Overlaid spectra of the CH and OH stretching region of untreated SC (black) and treated SC from regions within (red and pink) and outside (purple and blue) of the solvent inclusions. Inset images of relative solvent concentrations are marked at positions where the single pixel spectra were extracted. Spectra are shown on a true intensity scale (excluding untreated SC which is an average spectrum obtained from cluster analysis). Skin was treated with 100 mM FluA solutions as follows: (A) 6H incubation with Oct-d solution, (B) 20H incubation with Oct-d, (C) 6H incubation with PG-d/Et-d solution, and (D) 20H incubation with PG-d/Et-d. The scale bar of 6 µm applies to both x and z directions in all images and the color scheme is the same used in Figs. 2-B and 3-B for each respective solvent.

An average spectrum of untreated SC (black) is included in each set for comparison. The dominant peaks in the C-H stretching region are the symmetric and asymmetric methylene along with the symmetric methyl (~2850, 2880, 2930 cm^{-1}, respectively) stretching bands.

In Raman spectra of skin, the methylene modes mostly arise from lipid acyl chains, whereas the methyl band is mostly due to protein. The contribution to the methyl intensity at 2930 cm^{-1} from SC lipids is significantly less than that arising from SC protein as is demonstrated by published work on purified lipids[19] and the spectra shown herein. In addition, the contour of the bands in this region also reflects lipid acyl chain intra- and inter-molecular conformation and packing, respectively, in a complex manner. In spite of the complexity of the contour, a ratio of intensities (2880/2930 cm^{-1}) is tentatively suggested to provide a qualitative measure of the lipid/protein ratio. A comparison of the spectra between the two delivery vehicles reveals that there is little lipid and protein in the PG-d inclusion whereas some lipid and protein are observed in the Oct-d pockets. After 20 H Oct-d incubation, the CH stretching region (Figure 2-6 B, within the pockets) is dominated by the single bond CH stretch (at ~2893 cm^{-1}) due to incomplete deuteration of the octanol as is observed in the spectrum of the pure solvent (Figure 2-1 A). Similarly, within the pockets for the 20 H PG-d/Et-d experiment (Figure 2-6 D), the weak symmetric methyl stretching band (2930 cm-1) is broadened on the high frequency side, possibly due to a CH stretching contribution from the delivery vehicle (see Figure 2-1 A, band marked at ~ 2940 cm^{-1}).

Major spectral differences are noted in the CH stretching region from areas outside the solvent inclusion for the 20 H Oct-d delivery (Figure 2-6 B) compared to the untreated SC spectrum. In contrast, the spectra obtained outside the pockets for the PG-d/Et-d delivery (Figure 2-6 C and D) are very similar to the untreated SC. Variation in lipid content with depth is noted outside the pockets for the 6 H Oct-d treatment (Figure 2-6 A). The spectrum shown in blue is extracted from ~4 μm below the SC surface and exhibits a

lower lipid to protein ratio than the spectra extracted from either ~12 μm deep (purple) or the untreated control. It is possible that some endogenous lipid is being extracted from the surface layers by the Oct-d during the incubation period. In addition, the presence of the symmetric CH_2 stretching band (~2850 cm^{-1}) within the Oct-d pockets, especially after 20 H incubation (Figure 2-6 B), unequivocally indicates that endogenous lipid resides in the inclusions.

Evaluation of the relative water content, as monitored via the OH stretching band area in the spectra shown in Figure 2-6 (A-D), is consistent with the images shown in Figures 2-3 C and 2-4 C. Comparing spectra from the two Oct-d experiments (Figure 2-6 A and B), it is evident that the relative water content outside the solvent inclusions increases with incubation time. It is not surprising that water and Oct-d are phase separated in the SC. On the contrary, due to the hygroscopic nature of PG-d, relatively high water content is observed within the inclusions. It is noted that after 20 H PG-d/Et-d incubation (Figure 2-6 D), the water content outside the pockets is also somewhat higher than that of untreated SC.

Inspection of the Amide I spectral region reveals the potential for the observation of time- and delivery vehicle-dependent perturbation of keratin structure in the SC. A series of overlaid, normalized spectra obtained by cluster analysis are displayed in Figure 2-7 (A-D) for the four treatments. Cluster analysis was conducted using spectra in the SC over the 100-3790 cm^{-1} region and resulted in delineation of regions with and without solvent inclusions. The Amide I region of the resultant spectra are overlaid with an average spectrum obtained from untreated SC.

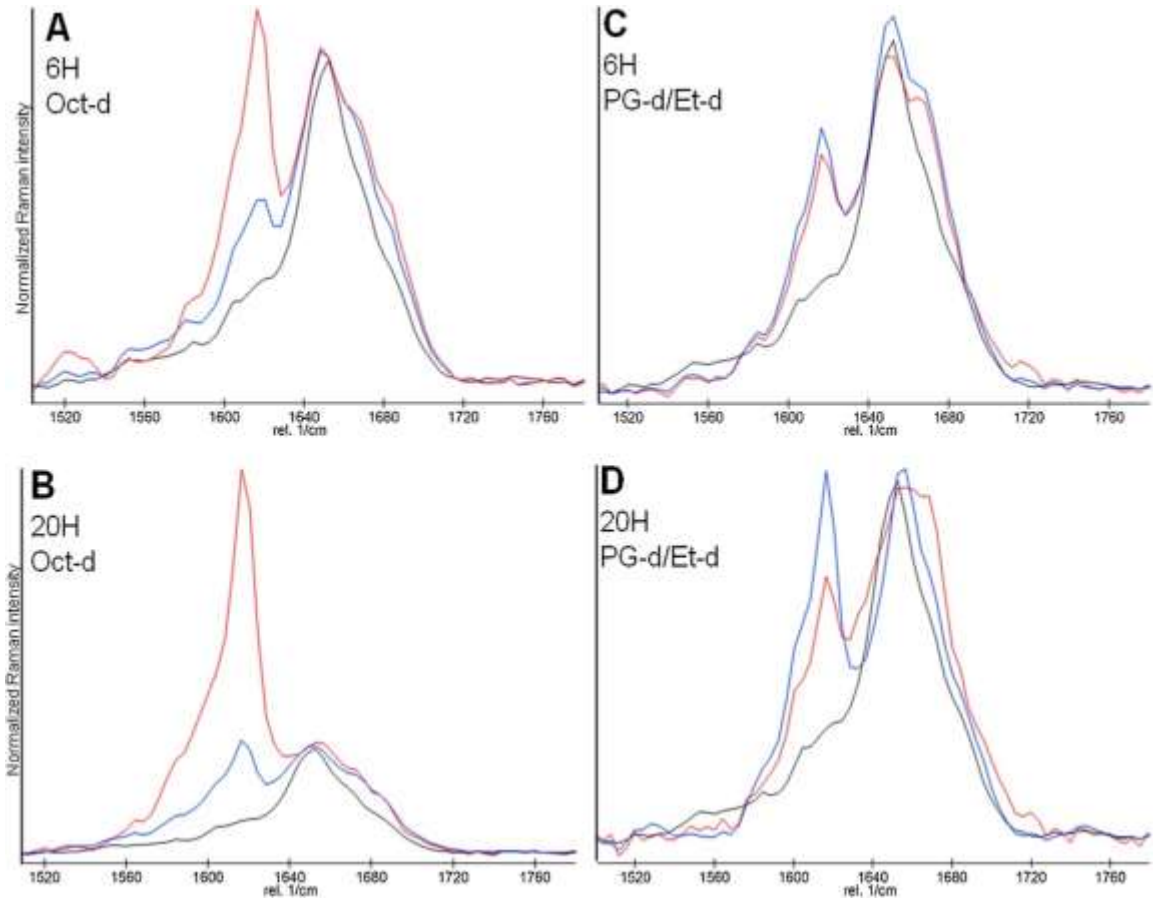

Figure 2-7. Overlaid normalized, average spectra in the Amide I spectral region including the FluA C=C stretch (~1618 cm^{-1}) of untreated SC (black) and treated skin from regions within (red) and outside (blue) of the solvent pockets obtained by cluster analysis. Skin was treated with 100 mM FluA solutions as follows: (A) 6H incubation with Oct-d solution, (B) 20H incubation with Oct-d, (C) 6H incubation with PG-d/Et-d solution, and (D) 20H incubation with PG-d/Et-d.

The Amide I band mostly arises from the peptide bond carbonyl stretch and its contour is sensitive to protein secondary and tertiary structure [20, 21]. In Raman spectra of the SC, keratin is the main contributor to intensity in the Amide I region with minor contributions arising from the components of natural moisturizing factor (NMF), small amounts of other SC proteins, and the ceramide Amide group. In Figure 2-7, the shape and position of the Amide I band in untreated SC (~1650 cm^{-1}) are consistent with the helical structure of keratin. In spectra of the treated skin, the C=C stretching band arising from FluA (~1618

cm^{-1}) is apparent along with Amide I. Compared to the spectrum of untreated SC, a slight broadening on the high frequency side of the Amide I band is observed for both Oct-d incubation times in the both SC regions (within and outside of the solvent inclusions). This observation may indicate a small change in the structure or hydration state of keratin. In contrast, a marked shoulder is observed at ~1668 cm^{-1}, predominantly in the spatial regions within the PG-d pockets, possibly indicating a greater amount of keratin denaturation compared to the Oct-d treatment. It is noted that the relative concentration of FluA in the PG-d pockets is likely to be less accurate compared to other skin regions due to the changes in the Amide I band shape along with significant decrease in intensity. Amide I intensity in this spectral region has been assigned to β-sheet structure [20,21] and this structural change has been shown to be reversible under certain conditions [16-18]. It should be noted, however, that the presence of the high frequency shoulder may well be due to, at least in part, the dissolution of particular NMF components [22] in PG-d which is consistent with the relatively low lipid and protein content observed in the inclusions (Figure 2-6 C and D).

2.4 Discussion

Understanding how the SC barrier responds to permeation enhancers provides mechanistic information important to the pharmaceutical, personal care, and cosmetic industries. In the current study, confocal Raman microscopy provided visualization of obvious enhancer-induced changes in the SC ultrastructure (10-100 μm scale) together with alterations in the spatial distribution and molecular structure of endogenous skin components. From both the lipophilic and hydrophilic vehicles used, the structure of the SC appeared to facilitate the formation of fairly discrete, oval-shaped domains (size range: a few to 100s of μm^2) of relatively high delivery agent concentration, albeit within the

constraints of this experiment (ex vivo skin, high enhancer amounts, incubation times, etc). Although several features of the enhancer domains were similar, the spatial distribution of the relative concentration of the model drug, FluA, in the skin was significantly different between the two vehicles. In addition, the spatial redistribution and molecular structure perturbation of endogenous skin constituents differed between the two vehicles. It should be noted that the protocol utilized herein is generic, i.e., it can be applied to investigation of various CPE's and active agents.

Previous reports, investigating the effect of hydration on water distribution in SC, utilized confocal Raman[12] and electron microscopy[23-25] to visualize water in discrete domains which were similar to the solvent inclusions in the current study. At high levels of hydration, both inter- and intracellular inclusions within the SC were observed. To the best of our knowledge, the presence of similar chemical (enhancer) inclusions in the SC has not been verified in the literature although their formation has been alluded to as a "pool" mechanism to facilitate diffusion in previous studies[26,27].

Previous penetration studies utilize FluA as a model lipophilic drug[6,7] with one goal of the study to develop a predictive in vivo method based on in vitro data. A subsequent report[8] compared FluA in vitro penetrations using various lipophilic ointments and hydrogels with different excipients in the formulations. In general, the concentration of FluA detected in the SC and deeper skin layers was higher for the hydrogel delivery systems, somewhat in contrast with the current results. However, within the hydrogel formulations, the one containing isopropanol, in which FluA is the most soluble, delivered the highest concentration of drug into the skin.

The distribution of FluA in the SC appears to be predominantly driven by its

solubility in the enhancers used in this study. A log P (partition coefficient P is a ratio of the concentrations of a solute between two immiscible phases, octanol and water) value of 5.62[28] defines the high solubility of FluA in octanol, whereas the addition of ethanol was necessary to dissolve the model drug in the hydrophilic vehicle, propylene glycol. After 20 H incubation, the contour of the CD stretching region for the hydrophilic vehicle that penetrated into the SC closely resembles that of pure PG-d. This observation and a relatively high FluA concentration in the outer 10 μm of the SC leads to the suggestion that Et-d penetrates quickly to deeper skin regions after the deposition of FluA in the upper SC. Some Et-d may also evaporate during the incubation period. The highest relative FuA concentration in the outer SC layers for hydrophilic delivery is approximately one half of the maximum value observed in the Oct-d pockets. Much lower FluA concentration is observed deeper in the SC which swells to about twice its normal thickness after 20 H incubation with the hydrophilic agent. In Figure 2-4 B and C (rightmost images), pockets of high PG concentration along with water are also observed in the viable epidermis. No evidence of significant FluA crystallization was observed in the Raman images. If crystallization had occurred, a shift (to ~ 1610 cm^{-1}) and narrowing of the C=C stretching band would have been noted (see Figure 2-1 A). Raman spectroscopy is an effective probe for detecting crystallization. In this regard, previous studies report microcrystals of exogenous materials close to the SC surface via stimulated Raman scattering[29] and within pigskin at a depth of ~ 35 μm after metabolism (in the skin) of a prodrug to the active, soluble drug using conventional confocal Raman microscopy[18]. It is possible that the FluA residing in the upper SC, delivered using the hydrophilic agent, continues to serve as a reservoir for prolonged diffusion deeper into the skin. It is also possible that the FluA in

the outer layers has ionized as its pKa of 3.65[28] is below the pH of the outer SC (pH ~ 5). This occurrence is likely to further slow the diffusion of FluA in the SC.

The distribution and relative concentration of FluA is also presumably dependent on vehicle-induced perturbation of the SC barrier. FluA is lipophilic and as such would likely utilize the continuous lipid pathway to penetrate through the SC. This pathway, in regions outside the vehicle pockets, does not appear to be significantly perturbed in the hydrophilic vehicle experiments as evidenced by the similarity in the CH stretching, consistent with previous reports that propose PG integration into the lipid hydrophilic head group region rather than interaction into the bilayers, leaving the acyl chain packing and conformational order less perturbed[30,31,32]. Although the relative water content in the SC has increased for the hydrophilic experiment after 20 H incubation both within and to a lesser extent, outside the pockets, FluA is not water soluble and diffusion, although slow, will most likely be through regions of endogenous lipid. In contrast, the lipid barrier appears to be significantly perturbed in the Oct-d experiments where time dependent lipid extraction is suspected and endogenous lipids are observed in the Oct-d pockets. In addition, water appears to be infiltrating into previously occupied SC spaces after the 20 H incubation period (Figure 2-3 C, rightmost image, and 2-6 B). These observations are consistent with earlier reports of octanol-induced endogenous SC lipid extraction[33]. Further analysis of the CH stretching region to shed light on excipient-induced perturbation, is complicated by the presence of the isolated CH stretch band arising from incomplete deuteration of the solvents. This and the intricacy of the contour which reflects the degree of lipid acyl chain packing and conformational order[34-36] , prevent further comment until additional control experiments are conducted. Regardless, the highest concentrations of

FluA appear to penetrate through the SC via the network of Oct-d inclusions which are not observed in the viable epidermis compared to that in SC regions outside the solvent pockets. Finally, when considering vehicle promoted changes influencing drug permeation, one commonly cited factor, i.e., drug release from the vehicle[33, 2], appears to be secondary to the solubility of FluA in octanol.

In the current work, the evolution and spatial distribution of the PG-d domains coincides with the development of the water pockets whereas the distribution of Oct-d inclusions is complementary to regions with a relatively high water concentration. The increase in water content for the Oct-d experiment first develops in the lower SC regions (compare 6 to 20 H incubation in Figure 2-3 C) suggesting that this water originated in the VE as opposed to coming from the environment.

To further investigate changes in the relative water content we focus on variation in the OH stretching region (see Figure 2-6). The OH stretching contour (3000-3700 cm^{-1}) in Raman spectra of the SC is overlapped with a contribution from the protein backbone Amide NH stretch (~ 3300 cm^{-1}), although the relative intensity of the latter, compared to the 2930 cm^{-1} methyl stretch, has been shown to be weak in freeze-dried SC[22]. In addition, the intensity in the OH region arises from several underlying bands. In spectra of liquid water, characteristic peaks are observed at ~ 3250 and 3450 cm^{-1} with a shoulder at ~ 3600 cm^{-1} [37]. Assignment of these bands is complicated by Fermi resonance, intensity considerations affected by salts, and various hydrogen bonding patterns; however, the shoulder at ~ 3600 cm^{-1} is commonly and reasonably assigned to free and/or weakly bound OH groups[37,38.] Qualitatively, the spectra in Figure 2-6 B and D (20 H incubation) display a slight increase in relative intensity on the high frequency side of the OH stretching

contour for regions with highest water content, i.e., outside of the Oct-d pockets and within the PG-d inclusions.

The confocal Raman images presented herein highlight the ability of the technique to examine compositional and structural heterogeneity in skin while tracking the penetration pathway of permeation enhancers and active agents. Future experiments will continue to address mechanisms of permeation enhancement that have been proposed, albeit with limited experimental evidence. Based on this poof of principle measurements, future experiments will be designed to more closely mimic excipient levels in commercial products. Finally, recent technological advancement in Raman approaches, such as stimulated Raman scattering, show promise of greater sensitivity and faster collection times along with in vivo capabilities[29, 39].

2.5 Conclusion

Overall, the structure of the SC appears to support the formation of localized pockets (size: a few – 100 of mm^2) of relatively high delivery agent concentration within the parameters of this experiment.

The highest FluA concentration is observed in the SC Oct-d pockets followed by a fairly homogenous spatial distribution in the upper VE. Oct-d appears to increase the H_2O content in the SC in regions outside the Oct-d pockets. This, along with possible lipid extraction and disordering, perturbs the barrier. Further study of SC lipid perturbation is needed.

In case of PPG-d/EtOH-d delivery agent, the highest concentration of FluA resides in the upper SC. H_2O accumulates while FluA and endogenous lipid is driven off in the regions with high PPG-d concentration. Denaturation of endogenous keratin in the SC is

observed in the regions with high PPG-d concentration. Further study is required to evaluate FluA concentration in the VE due to swelling of SC by PPG-d.

2.6 References

1. Elias, P.M., "Structure and function of the stratum corneum permeability barrier", *Drug Dev. Res*., **1988,** 13, pp. 97-105.

2. Lane, M.E., **"**Skin penetration enhancers", *Int. J. Pharm.*, **2013**, 447, pp. 12-21.

3. Williams, A.C., Barry, B.W., "Penetration enhancers", *Adv. Drug Deliv. Rev*., **2012**, 64, pp. 128-137.

4. Pyatski, Y., Zhang, Q., Mendelsohn, R., Flach, C.R., "Effects of Permeation Enhancers on Flufenamic Acid Delivery in Ex Vivo Human Skin by Confocal Raman Microscopy", *International Journal of Pharmaceutics,* **2016**, 505(1), pp.319-328.

5. Reynolds, J.E.F., **"**Martindale: The Extra Pharmacopoeia*",* **1993,** *American Pharmaceutical Association*, (30 ed.).

6. Wagner, H., Kostka, K.H., Lehr, C.M., Schaefer, U.F., **"**Interrelation of permeation and penetration parameters obtained from in vitro experiments with human skin and skin equivalents"**,** *J. Control. Release,* **2001,** 75, pp. 283-295.

7. Wagner, H., Kostka, K.H., Lehr, C.M., Schaefer, U.F., **"**Human skin penetration of flufenamic acid: in vivo/in vitro correlation (deeper skin layers) for skin samples from the same subject", *J. Invest. Dermatol*., **2002**, 118, pp. 540-544.

8. Wagner, H., Kostka KH, Adelhardt W, Schaefer UF., "Effects of various vehicles on the penetration of flufenamic acid into human skin", *Eur. J. Pharm. Biopharm*., **2004,** 58, pp. 121-129.

9. Rubio, L., "Bicellar systems as new deliver strategy for topical application of flufenamic acid"**,** *Int. J. Pharm*., **2013,** 444, pp. 60-69.

10. Hoppel,M., "Influence of the composition of monoacyl phosphatidylcholine based microemulsions on the dermal delivery of flufenamic acid", **2014**, *Int. J. Pharm*., 475, pp. 156-162.

11. Hoppel, M., Ettl, H., Juric, S., Valentina, S.,"Effect of monoacyl phosphatidylcholine content on the formation of microemulsions and the dermal delivery of flufenamic acid", *Int. J. Pharm*., **2015,** 479, pp. 70-76.

12. Albèr, C., Brandne,, B.D., Björklund, S,, Billsten, P., Corkery, R.W,, Engblom. J., "Effects of water gradients and use of urea on skin ultrastructure evaluated by confocal Raman microspectroscopy", *Biochim. Biophys. Acta*, **2013,** 1828, pp. 2470-2478.

13. Förster, M., Bolzinger, M.A., Ach, D., Montagnac, G,, Briançon, S., "Ingredients tracking of cosmetic formulations in the skin: a confocal Raman microscopy investigation", *Pharm. Res*., **2011,** 28, pp. 858-872.

14. Smith, G.P.S., McGoverin, C.M., Fraser, S.J., Gordon, K.C., "Raman imaging of drug delivery systems", **2015,***Adv. Drug Del. Rev*., **2015,** 89, pp. 21-41.

15. Tfayli, A., Piot, O., Manfait, M., "Confocal Raman microspectroscopy on excised human skin: uncertainties in depth profiling and mathematical correction applied to dermatological drug permeation", *J. Biophotonics*, **2008,** 1, pp. 140-153.

16. Zhang, G., Flach, C.R., Mendelsohn, R., "Tracking the dephosphorylation of resveratrol triphosphate in skin by confocal Raman microscopy", *J. Control. Release*, **2007,** 123, pp. 141-147.

17. Zhang, G., Moore, D.J., Flach, C.R, Mendelsohn, R., "Vibrational microscopy and imaging of skin: from single cells to intact tissue", *Anal. Bioanal. Chem*., **2007,** 387, pp. 1591-1599.

18. Zhang, G., Moore, D.J., Flach, C.R, Mendelsohn, R., "Imaging the prodrug-to-drug transformation of a 5-fluorouracil derivative in skin by confocal Raman microscopy", *J. Invest. Dermatol*., **2007**, 127, pp. 1205-1209.

19. Percot, A., Lafleur., M.,"Direct observation of domains in model stratum corneum lipid mixtures by Raman microspectroscopy", *Biophys. J.,* **2001,** 81, pp. 2144-2153.

20. Peticolas, W.L., "Raman spectroscopy of DNA and proteins", *Methods in Enzymology, Academic Press, New York*, **1995,** pp. 389-397.

21. Yager, P., "Membranes", **1987,** *T.G. Spiro (Ed.), Biological Applications of Raman Spectroscopy, John Wiley and Sons, New York*, pp. 203-261.

22. Caspers, P., Lucassen, G.W., Wolthuis, R., Bruining, H.A., Puppels, G.J., "In vivo Raman spectroscopy of human skin: determination of the composition of natural moisturizing factor", *SPIE Proc*., **1999,** 3608, pp. 99-102.

23. Bouwstra, J. A., A de Graaff, Gooris, G.S., Nijsse, J., "Water distribution and related morphology in human stratum corneum at different hydration levels", *J. Invest. Dermatol.*, **2003,** 120, pp. 750-758.

24. Richter, T., Peuckert, C., Sattler, M., Koenig, K., "Dead but highly dynamic—the stratum corneum is divided into three hydration zones", *Skin Pharmacol. Physiol*., **2004**, 17, pp. 246-257.

25. Warner, R. R., Stone, K.J.,Boissy., Y.L., "Hydration disrupts human stratum corneum ultrastructure", **2003**, *J. Invest. Dermatol*., 120, pp. 275-284.

26. Ongpipattanakul, B., Burnette, R.R., Potts, R.O., "Evidence that oleic acid exists in a separate phase within stratum corneum lipids", *Pharm. Res.,* **1991,** 8, pp. 350-354.

27. Santos, P., "Influence of penetration enhancer on drug permeation from volatile formulations"**,** *Int. J. Pharm*., **2012,** 439, pp. 260-268.

28. Hadgraft, J., "The selection of non-steroidal anti-inflammatory agents for dermal delivery"**,** *Int. J. Pharm*., **2000,** 207, pp. 31-37.

29. Belsey, N., Garrett, N.L., Contreras-Rojas, L.R., "Evaluation of drug delivery to intact and porated skin by coherent Raman scattering and fluorescence microscopies", *Control. Release,* **2000,** 174, pp. 37-42.

30. Bouwstra, J.A., "Structural investigations of human stratum corneum by small-angle X-ray scattering", **1991,** *J. Invest. Dermatol.,* 97, pp. 1005-1012.

31. Brinkmann, I., "An attempt to clarify the influence of glycerol, propylene glycol, isopropyl myristate and a combination of propylene glycol and isopropyl myristate on human stratum corneum"**,** *Die Pharm.,* **2005,** 60, pp. 215-220.

32. Hoogstraate, A. J., et. al., "Kinetics, ultrastructural aspects and molecular modelling of transdermal peptide flux enhancement by *N*-alkylazacycloheptanones**",** *Int. J. Pharm.,* **1991,** 76, pp. 37-47.

33. Dias, M., Hadgraft, J., Lane, M.E., "Influence of membrane-solvent-solute interactions on solute permeation in skin"**,** *Int. J. Pharm*., **2007,** 340, pp. 65-70.

34. Gaber, B.P., Peticolas, W.L., "On the quantitative interpretation of biomembrane structure by Raman spectroscopy", *Biochim. Biophys. Acta*, **1976**, 465, pp.260-274.

35. McCarthy, P.K., Huang, C.-H., Levin, I.W., " Raman spectroscopic study of polycrystalline mono- and polyunsaturated 1-eicosanoyl-d39-2-eicosenoyl-sn-glycero-3-phosphocholines: bilayer lipid clustering and acyl chain order and disorder characteristics", *Biopolymers*, **1999**, 57, pp. 2-10.

36. Yellin, N., " Hydrocarbon chain disorder in lipid bilayers", *Biochim. Biophys. Acta*, **1977**, 489, pp. 177-190.

37. Leikin, S., Parsegian, V.A., Yang, W.-H., Walrafen., G.E., " Raman spectral evidence for hydration forces between collagen triple helices", *Proc. Natl. Acad. Sci. U. S. A.* **1977**, 94, pp. 11312-11317.

38. Lafleur, M., Pigeon, M., Pezolet, M., Caille, J.P., "Raman spectrum of interstitial water in biological systems", *J. Phys. Chem.*, **1989**, 93, pp. 1522-1526.

39. Saar, B.G., “Video-rate molecular imaging in vivo with stimulated Raman scattering”, *Science*, **2010**, 330, pp. 1368-1370.

Chapter 3: Infrared Investigation of Terbinafine Interaction with Stratum Corneum Constituents

3.1 Introduction:

Efficient transdermal delivery of many pharmaceuticals requires introducing modifications to the SC barrier. These modifications are usually achieved by using proper active ingredients and formulation excipients. However, most of the methods used evaluate dermatopharmacokinetics to assess bioavailability and bioequivalence of drug in skin [1,2,3]. The major analytical techniques used for this purpose are based on HPLC. Although the sensitivity of HPLC is very high, rendering it very useful for determination of concentrations as low as 1 μmol/L[4] , the approach provides no information about the mechanism of interaction of the drug with the SC constituents.

Terbinafine is a small lipophilic drug (molecular weight=291 Da, log [octanol/water partition coefficient]=3.3, see structure Figure 3-1) which functions as an antifungal substance used to treat ringworm, pityriasis versicolor, and fungal nail infections. The lipophilic properties of terbinafine make it possible for it to accumulate at high concentrations in the SC. It is marketed under the trademark Lamisil® and either taken by mouth orally or applied to the skin as a cream or ointment. Terbinafine is highly soluble in organic solvents such as ethanol (EtOH). It is important to evaluate the mechanism of action of terbinafine in the SC to design better formulations and improve drug bioavailability.

The mechanism of terbinafine action on fungal infections is based on squalene epoxidase inhibition[5]. Ergosterol is an essential component found in cell membranes of fungi, having equivalent functions that parallel those of cholesterol in animal cells. It is thus required for membrane integrity and also for growth. Terbinafine acts specifically by

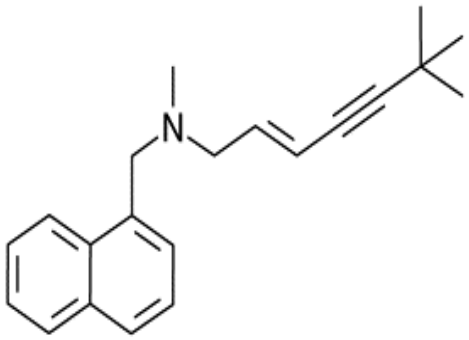

Figure 3-1. Chemical structure of terbinafine.

inhibiting fungal ergosterol biosynthesis at the point of squalene epoxidation. As a result of this inhibition, the treated fungal cells rapidly accumulate intermediate squalene and become deficient in the end-product of the pathway, ergosterol. Terbinafine, as in many other antifungal agents has the following properties for effective treatment: efficacy at low concentrations, fungicidal activity with convenient dosing schedules, keratinophilic and lipophilic physical properties, high clinical cure rates and a reservoir effect in the stratum corneum. Terbinafine efficacy is achieved by its reversible binding to keratin in SC. Also, due to its lipophilic properties, it can accumulate at high concentrations in the lipid layers of the SC[6].

Due to its superior antifungal properties there is significant interest in improving drug delivery systems for terbinafine. As most topical therapies require multiple daily applications as well as lengthy treatment durations to achieve good efficacy, a research group developed a novel cutaneous solution (film-forming solution, FFS) only requiring one application[7]. This was a clinical breakthrough in medicine, combating the medication compliance issue. The combination of a volatile solvent (ethanol), terbinafine (as a hydrochloride salt), and a polymer resulted in a smooth film of terbinafine on skin. In vivo pharmacokinetic studies of terbinafine FFS were conducted following single-dose

administration[6]. The FFS approach showed improved higher total terbinafine recovered. Furthermore, the terbinafine film resided on skin surface for approximately 72 h, whereas terbinafine cream only exhibited adherence for 12 h. The novel formulation provides the antifungal agent with more adherence to the SC. This probably is due to the way the hydrochloride salt interacts with proteins in the horny layer, or the hydrophilic/hydrophobic nature of the polymer.

No detailed research has been published at the physicochemical level to probe the interactions of terbinafine with SC keratin and lipids. IR is the most advantageous and non-destructive technique for studies of both lipid and keratin structures in an unperturbed skin SC environment. In contrast, most of the HPLC methods require destruction of samples and homogenization of skin to extract needed compounds. Additionally, IR bands are very sensitive to structural changes in both lipid and keratin components. In this study, IR methods were applied to monitor changes with time and temperature in the conformation-sensitive SC IR bands upon introduction of terbinafine.

Current commercially available terbinafine treatment (Lamisil ®), is formulated with ingredients such as benzyl alcohol, cetyl alcohol, stearyl alcohol and polysorbate 60. It is common practice in the pharmaceutical industry to use alcohols and detergents as CPEs for topical transdermal formulations in order to interact with the lipid matrix of the stratum corneum, to alter its nanostructure and thereby increase permeability[8]. Alcohols and detergents can extract barrier lipids and/or disrupt their bilayer structures, which then makes the stratum corneum more permeable[9,10,11]. Among alcohols, ethanol is a well known skin penetration enhancer that acts by decreasing the molecular interaction between the polar head groups of ceramides found in the skin and/or through interactions between

their alkyl chains[12]. Different mechanisms of ethanol action have been proposed, including fluidization of the intercellular lipid matrix, or the extraction of epidermal lipid components[13,14]. Increased transepidermal water loss (TEWL) has been observed following ethanol application to subjects and this was attributed to extraction of lipids. Some researchers have observed changes in SC lipid melting temperatures. The maximum effects were observed for ethanol:water (50:50), but neat ethanol was not examined independently[15]. It has been suggested that ethanol disrupts SC intercellular lipid structure, forms pores, and promotes the orthorhombic-(the most tightly packed lipid organization) to hexagonal (a less tightly packed lipid organization) lipid phase transitions[16,17,18]. Recently, ethanol was used as a solvent of choice to design a more long acting transdermal terbinafine film-forming solution (FFS) that required only one application[19].

3.2 Materials and Methods

3.2.1 Materials

The following chemicals were used without further purification : trypsin (porcine pancreas) (Sigma, MO, USA), 10X PBS (Sigma-Aldrich, MO, USA), ethanol (Pharmaco-Aaper, KY, USA), citric acid (Sigma, MO, USA).

Human skin (female Caucasian, abdominal pieces from plastic surgery) was obtained from ZenBio Labs, NC, USA. Sections were wrapped in aluminum foil, flash frozen in liquid nitrogen and stored at -20°C for no more than 6 months prior to usage.

3.2.2 Sample preparation

Skin samples from frozen sections were cut to a size of ~1x1cm and thawed. Sebum was removed with q-tips. The stratum corneum (SC) of samples was subjected to tryptic digest by placing them SC side up into a 0.5% w/v trypsin in phosphate-buffered saline

solution for ~24 hours at room temperature (RT) pH 7.4-7.6. The SC was then physically separated from skin, washed in distilled water and placed into a 10% w/v terbinafine solution in EtOH/100 mM citrate buffer pH 5.8 (50:50) for 18hr at room temperature. The sample was then briefly rinsed in deionized water, placed on a ZnSe IR window and allowed to dry in a desiccator for ~24 hrs. For reversible binding experiments, after the 10% terbinafine soak, the SC was transferred into the EtOH/buffer (50:50) solution for 6hrs, prior to again placing it onto a ZnSe window to dry. For experiments where relative humidity (RH) was controlled, soaking in a 10% terbinafine solution was followed by drying of SC on a ZnSe window and IR measurements were performed. The sample was then left for 24hr in a relative humidity chamber at ~80% RH. Following this procedure, IR spectra were again acquired.

3.2.3 IR measurements

Dried SC was sandwiched between two ZnSe windows and placed into a temperature controlled IR sample cell (Harrick Scientific, Ossining, NY). A 5 mm size mask was used to cover any sample discontinuities. A thermocouple embedded into the cell assembly was used to monitor the sample temperature. Temperature-dependent IR spectra were acquired with a Nicolet 6700 spectrometer equipped with an MCT detector (Thermo Electron Corporation, Madison, Wisconsin, WI). Typically, two scans each consisting of 128 interferograms were co-added with resolution of 2 cm^{-1} and processed with 1 level of zero filling. N_2 gas was used to purge the IR instrument to reduce interference from water vapor. . Thus, the Amide I contour in each case shows major intensity near 1650 cm^{-1}, but as noted above, this band is complicated by sharp peaks from the rotation-vibration spectrum of water vapor.

3.2.4 Infrared data analysis

IR data treatment was initially performed in GRAMS v.6.00, in which the "mfutils" program was used to group multiple files at different temperatures into one multifile per experiment. Additional manipulations including spectral baseline correction, peak integration, spectral normalization, and peak height ratio (PHR) determinations were accomplished using ISys v.3.1.1.18 software. Peak frequencies were determined from second-derivative spectra with a center of gravity routine[20]. Plots of peak frequencies vs. temperature were created with Excel. The extent of β-sheet present was estimated using peak height ratios (PHR) of the β-sheet shoulder peak maximum vs α-helix peak maximum. Values at 25±2 °C were plotted in Excel as bar charts. Precision in the frequency measurement as good as 0.05 cm^{-1} can be achieved if IR measurements are carried out with great care as described by Pensack et. al.[18].

3.3 Results

3.3.1 Terbinafine effect on keratin's β-sheet content

One of the major components of the SC is keratin, a fibrous protein normally possessing a predominantly α-helical conformation. The structural organization of keratin in SC corneocytes is of major importance for establishing the barrier properties of skin, the water-holding capacity of skin, the mechanical strength and elastic resilience of skin, and skin pathologies, e.g., dry skin.

Spectra-structure correlations between the protein amide bond vibrational frequencies and secondary structure are well established [21,22,23]. In particular, the Amide I and Amide II frequencies are very sensitive to changes in protein secondary structure. The Amide I mode is a combination of peptide bond C=O (70-85%) and C-N (10-20%).

stretching internal coordinates It appears at ~1650 cm^{-1} for an α-helix and at 1620-1630 cm^{-1} for a β-sheet[22]. Additional weak β-sheet peaks are observed at 1680-1695 cm^{-1} [24]. The Amide II band (1550 cm^{-1}) is a combination of in plane N-H bending (40-60%) and C-N stretching (18-40%) internal coordinates of the peptide bond. The mode appears at ~1540-1550 cm^{-1} for the α-helix and 1520-1530 cm^{-1} for the β-sheet[25].

Spectral data in the region ~ 1484-1725 cm^{-1} for various experiments relevant to the interaction of terbinafine with keratin are shown in Figures 3-2. One complication evident in many of the spectra is that the most intense feature in the Amide I region appears to split into an apparent "doublet" with peaks at ~1651.3 and 1654.7 cm^{-1}. In fact, the Amide I peak, at the relatively high absorbance levels in the contour, was overlapped by residual water vapor interference. It is noted that the SC sample cannot be reduced in thickness without causing damage. Therefore, the Amide II mode (present as a relatively lower intensity band and relatively free from water vapor interference in the spectra) was used as the most reliable source of keratin secondary structure information.

IR spectra, truncated, baseline corrected, normalized and offset from each other, of the Amide I and Amide II spectral regions for SC treated under different experimental conditions, are shown in Figure 3-2(A) and include: SC untreated, SC treated with buffer (no ethanol), SC treated with EtOH-containing buffer, SC treated with terbinafine in EtOH buffer, and SC treated with terbinafine and soaked in EtOH/buffer to reverse terbinafine binding. The. Thus, the Amide I contour in each case shows major intensity

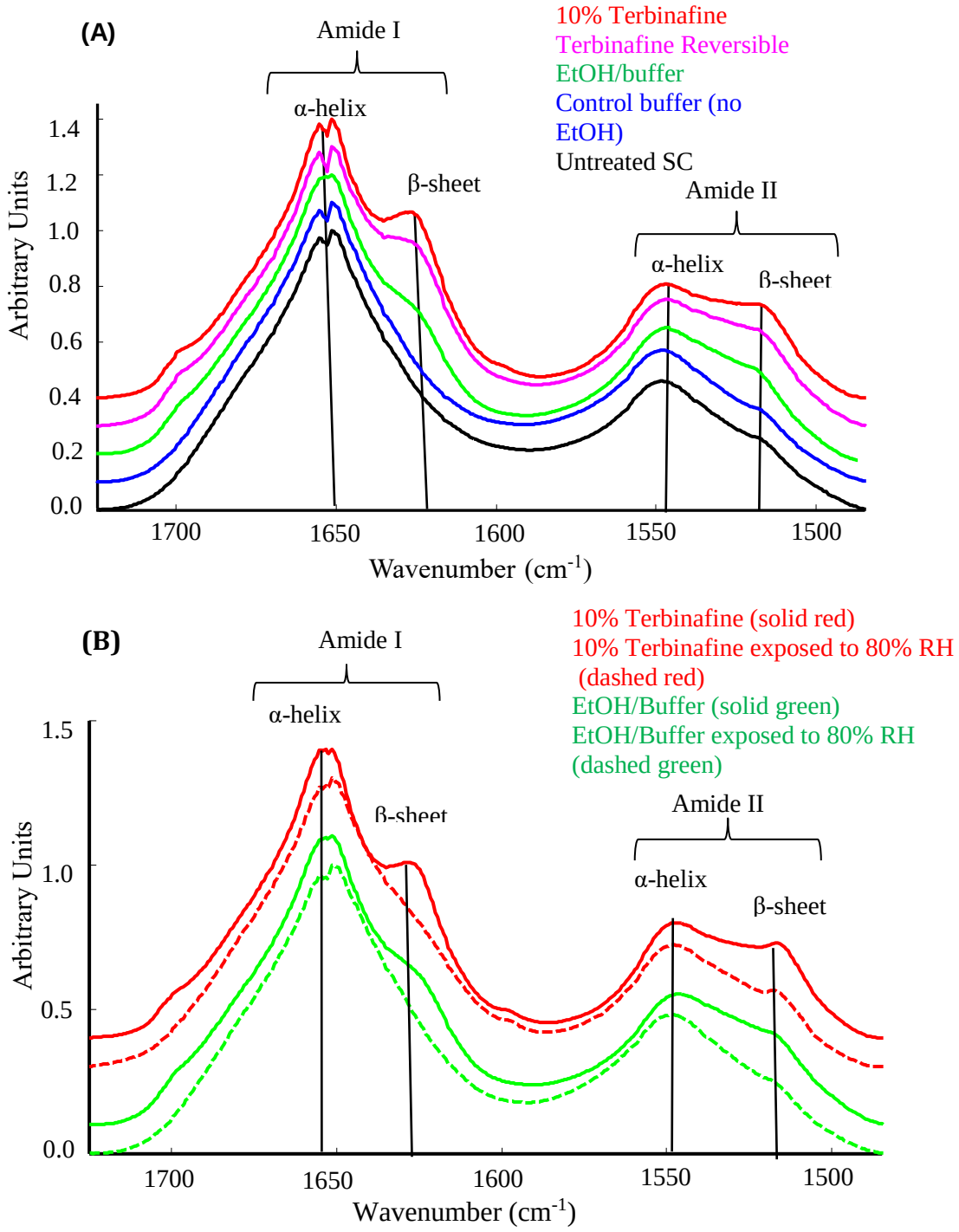

Figure 3-2(A-B). IR spectra of the Amide I and Amide II regions (1725.5-1484.5 cm^{-1}) of SC treated under different conditions, normalized to the Amide I mode: (A) SC untreated (black), SC treated with buffer (no ethanol) (blue), SC treated with EtOH-containing buffer (green), SC treated with 10% terbinafine in EtOH buffer (red), reversible binding experiment (pink). (B) SC treated with 10% terbinafine before exposure to RH (red solid), SC treated with 10% Terbinafine after exposure to 80% RH (red dashed), SC treated with EtOH buffer before exposure to RH (green solid), SC treated with EtOH buffer after exposure to RH (green dashed).

near 1650 cm^{-1}, but as noted above, this band is complicated by sharp peaks from the rotation-vibration spectrum of water vapor. The Amide II contour shows a major single feature at 1547 cm^{-1} and an additional weaker feature at 1518 cm^{-1}, arising from a small percentage of β - sheet structure. Addition of EtOH to the buffer induces some α-helix→β-sheet conversion as revealed by the shoulder at 1628 cm^{-1} in the Amide I band and increased intensity of shoulder at 1518 cm^{-1} in the Amide II band. More substantial β-sheet formation was observed in terbinafine treated SC as judged by very pronounced shoulders at 1628 cm^{-1} and 1518 cm^{-1} in the Amide I and Amide II regions, respectively. Additional confirmation of β-sheet presence is also manifested by a weak shoulder at 1690-1700 cm^{-1} in the Amide I contour.

Spectra for terbinafine reversible binding experiments were collected following the reversal of terbinafine binding as discussed in the experimental section. For these experiments, SC was first soaked in 10% terbinafine EtOH/buffer solution and then soaked in EtOH/buffer solution only. It was observed that the effect of terbinafine dissolved in EtOH/buffer only, was mostly reversed as monitored from β-sheet→α-helix changes in the secondary structure of keratin (as deduced from the Amide I and II assignments discussed above).

The effect of increasing relative humidity (RH) on the α-helix to β-sheet interconversion induced in keratin by terbinafine is shown in Figure 3-2(B) which depicts IR spectra of SC treated with 10% terbinafine before and after exposure to 80% relative humidity. In addition, control spectra of an SC sample experiment compared with SC treated with EtOH/Buffer control (i.e., no terbinafine) are shown before and after the same RH change. Spectra again were truncated, baseline corrected, normalized and offset for

ease of evaluation. The β-sheet to α-helix reversible interconversion was induced by rehydration of SC at 80% humidity. Thus, as is evident in the figure, β-sheet shoulders in rehydrated terbinafine treated SC and EtOH/buffer control treated SC were mostly absent in the resultant Amide I and Amide II bands.

To provide a more quantitative measure of keratin structural changes than simple visual examination of the Amide I and II contours, the peak height ratio (PHR) of the Amide I at 1628 cm^{-1} (β-sheet) to Amide I at 1654cm^{-1} (α-helix) and Amide II 1518 cm^{-1} (β-sheet) vs 1547 cm^{-1} (α-helix) were calculated and plotted as bar charts, with Amide I shown in Figure 3-3(A) and the Amide II in Figure 3-3(B). Spectra were truncated and baseline corrected. The desired ratios were calculated and plotted as bar chart plots. Bar chart values were selected at 25±2 °C. Each bar on the chart is an average of several experiments. The data so plotted clearly demonstrate progression of the α-helix to β-sheet conversion with introduction of EtOH (SC treated with EtOH/buffer control) and then terbinafine (SC treated with 10% solution of terbinafine in EtOH/buffer). The smallest level of β-sheet structure was observed in untreated and buffer control treated SC. The reversible binding experiment slightly reduced the level of β-sheet formations and reduced it down to the levels of SC treated with ethanol containing buffer. Rehydration of terbinafine treated SC lowered the level of β-sheets to the quantities present in the SC treated with ethanol containing buffer, while rehydration of EtOH/buffer control treated SC reduced the amount of β-sheets to the quantities similar of those present in the untreated and buffer treated SC. There is a striking similarity in the change in Amide I and II regions patterns (bar chart plots Figure 3-3 A-B). The close resemblance of these

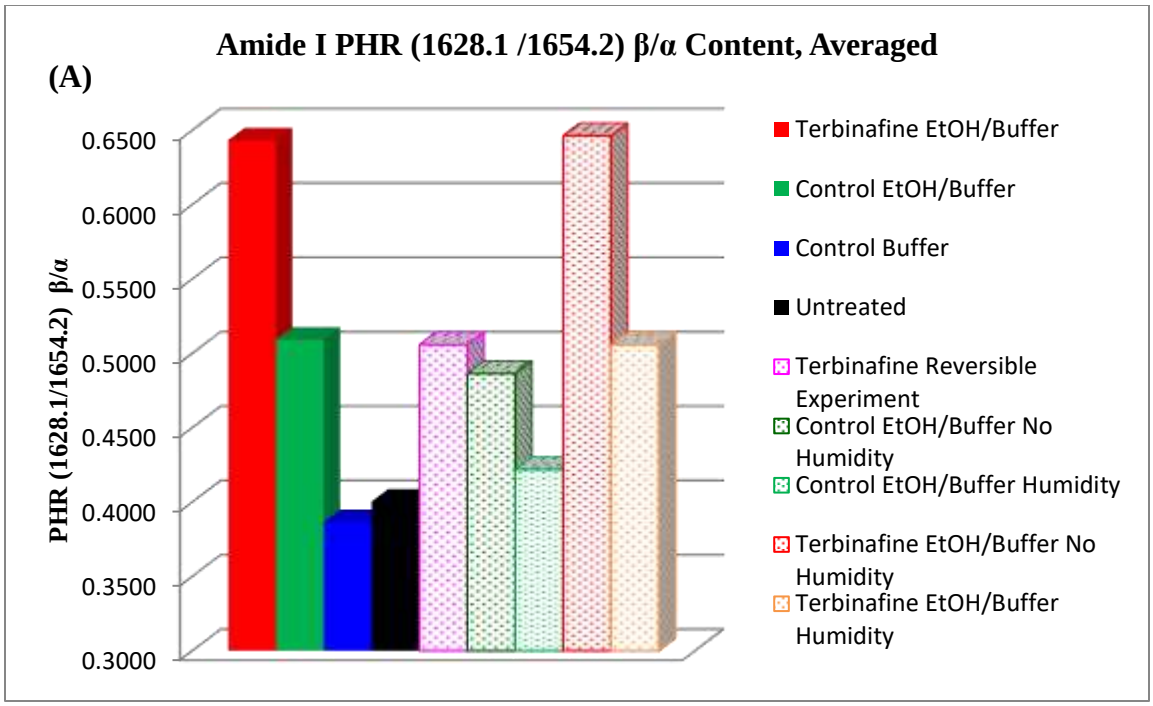

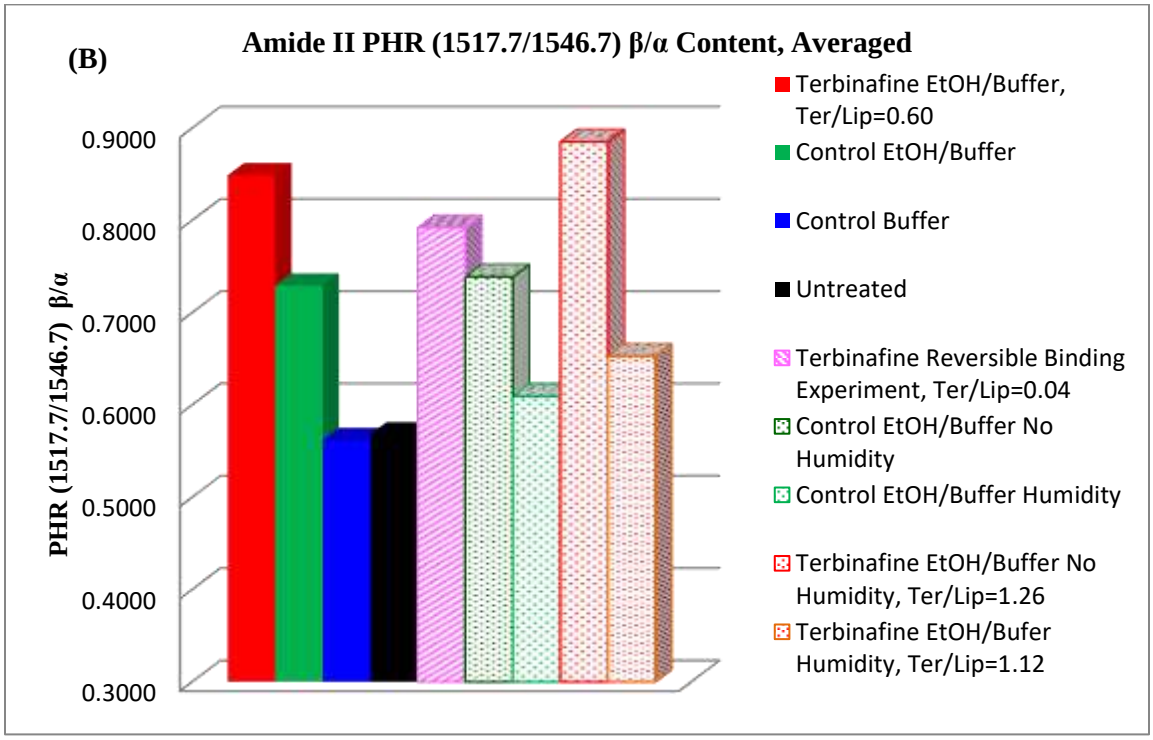

Figure 3-3 (A-B). β sheets estimation bar charts with averaged Amide I (A) and Amide II (B) PHR data of SC treated under various conditions.

patterns demonstrates that Amide I and Amide II regions are very sensitive to keratin's secondary structure changes and are complimentary and consistent with each other.

The Amide II band thus proved to be as informative and useful in evaluation of keratin structural changes as the Amide I band. In addition as noted above, the band suffers much less interference than Amide I from residual water vapor. Therefore, for a more quantitative evaluation of spectral changes, it was decided to create difference spectra (from the Amide II region) in which a spectrum of untreated SC was subtracted from spectra of samples treated in the various ways described above. The advantage of this approach is that it reduces spectral overlap from the skin ceramide Amide II vibrations known to occur in this spectral region[26]. Any bands observed in the difference spectra should originate at least mostly from altered protein secondary structure. The difference spectra are shown in Figure 3-4. Following spectral subtraction, the resultant AUC (Area Under the Curve) was integrated, and bar charts were plotted (see Figure 3-6 (A-B)). The Amide II integrated AUC pattern closely resembles the Amide II PHR pattern (where control buffer and untreated SC were considered as a baseline marker). It appears that this data treatment approach is more favorable, since by subtraction of the Amide II band of untreated SC, the difference spectra directly probe the change in β structure content.

Representative spectra in Figure 3-4 shows a clear progression in the increase of β-sheet content as follows: terbinafine treated SC and terbinafine treated SC before exposure to RH (replicate experiment) > terbinafine treated SC washed with EtOH/Buffer > EtOH/buffer control before exposure to RH and EtOH/buffer control (replicate experiment), > terbinafine treated SC exposed to RH > EtOH/buffer only treated SC exposed to RH. Simultaneously, following subtraction, there is a clear pattern of negative

difference spectral dips at the α-helix peak. The magnitude of the negative peaks are increased in the following order: terbinafine treated SC and terbinafine treated SC before exposure to RH (replicate experiments) > terbinafine treated SC washed with EtOH/buffer > EtOH/buffer control > terbinafine EtOH/buffer treated SC exposed to RH, > and EtOH/buffer control and EtOH/buffer control before exposure to RH (replicated experiment). EtOH/buffer control exposed to RH produced positive feature (increased α-helix content after subtraction. EtOH/buffer treated SC exposed to RH is the only subtracted spectrum that demonstrated this feature.

Upon subtraction of spectra, additional bar charts were plotted in Figure 3-6. The pattern of subtracted spectra Figure 3-6 (B) resemble the pattern of Amide II PHR in Figure 3-6(A), where control buffer and untreated SC were considered as a baseline marker. The only exception is negative feature formed upon spectral subtraction from EtOH/buffer treated SC exposed to RH. In addition, a semi-quantitative estimation of terbinafine was performed, as depicted in Figure 3-5, using the ratio of terbinafine area under the peak at 775cm^{-1} (B) to lipid integrated low frequency half of the peak area at 2850 cm^{-1} (lipid symmetric CH_2 stretch) (A). Half the peak area was used, because there were some baseline interferences in the high frequency half of the peak. In the terbinafine doublet, only the 775cm^{-1} band was used, because the second peak at ~790 cm^{-1} suffered baseline interferences on the high frequency side. In EtOH/buffer reversible

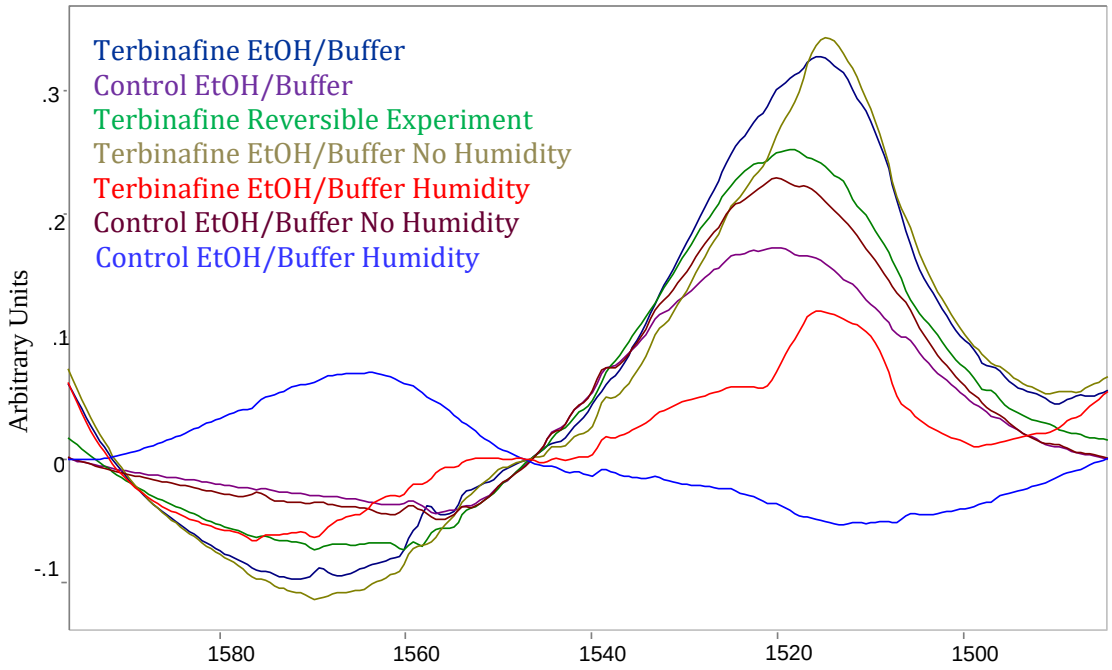

Figure 3-4. Difference spectra (from Amide II region) in which a spectrum of untreated SC was subtracted from spectra of samples treated in the various ways described above.

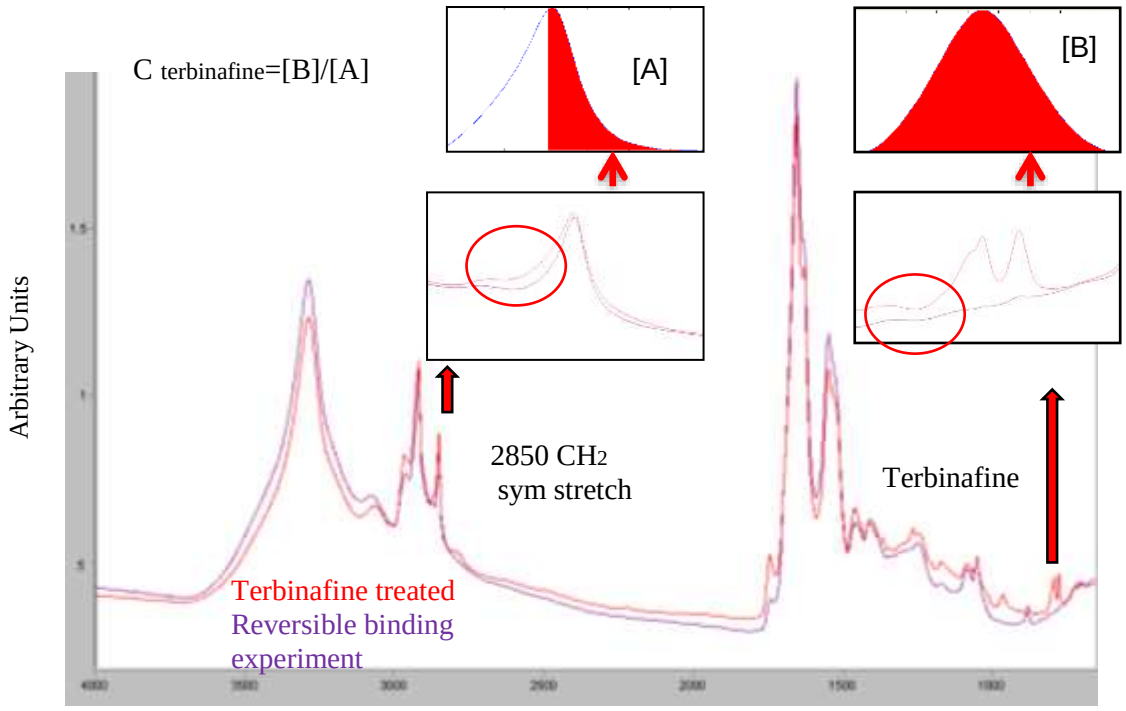

Figure 3-5. Semi quantitative estimation of terbinafine. It was estimated using the ratio of terbinafine area under the peak at 775 cm^{-1} (B) to lipid integrated half peak area at 2850 cm^{-1} symmetric CH_2 stretch (A). Half peak area was used, because there were some baseline interferences at the frontal area of the CH_2 symmetric stretch peak. Terbinafine peak at only 775cm^{-1} was used, because another terbinafine peak at 791 cm^{-1} had baseline nterferences at the peak fronting area.

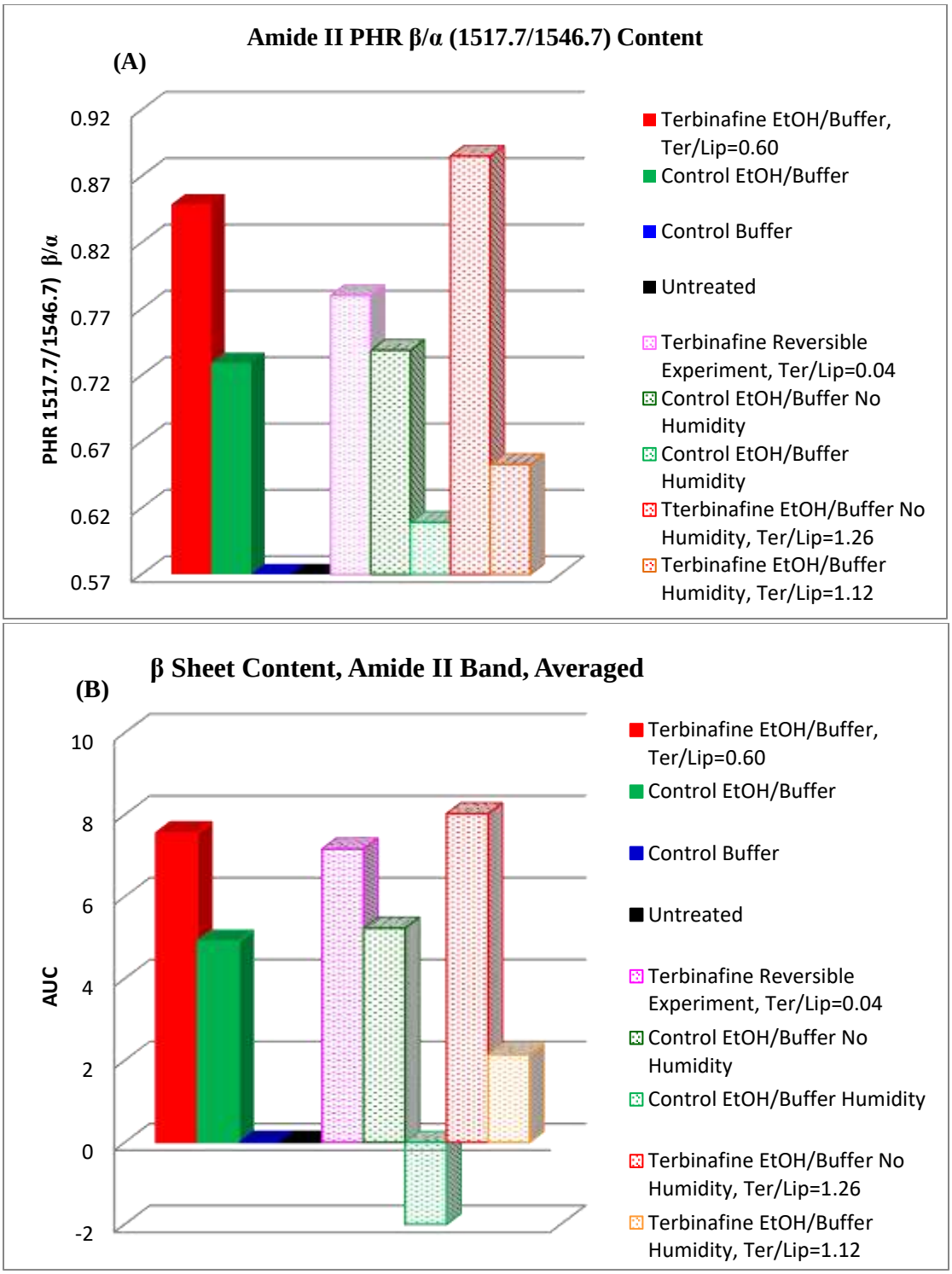

Figure 3-6. β sheets estimation via bar charts with averaged Amide II data. (A) Amide II PHR pattern, where control buffer and untreated SC were considered as a baseline marker (B) Amide II presented as area under the curve (AUC) of untreated SC subtracted from spectra treated under various conditions. Terbinafine semi quantitatively estimated as Ter/Lip ratio.

wash experiment, the amount of β-sheet is slightly enhanced in comparison to EtOH/buffer treated SC, while the amount of terbinafine is significantly reduced in comparison to the terbinafine EtOH/buffer treated SC. In the rehydration experiment, the amount of β-sheet was reduced while the amount of terbinafine remained unchanged.

3.3.2 Effect of terbinafine on carboxylate groups

In addition to the secondary structure information from the Amide I and II regions, bands due to the symmetric and antisymmetric stretches of the COO^- groups in amino acid side chains may provide clues about the tertiary structure of the keratin[27]. IR spectra of carboxylate groups in SC treated under various conditions are shown in Figure 3-7(A). Untreated and buffer treated SC have maxima at 1403 cm^{-1}, in agreement with literature values for the COO,- the symmetric stretching band maxima[28] suggested to occur in the 1405-1402 cm^{-1} range.

Following EtOH buffer treatment, the band shifted to 1399 cm^{-1}. In contrast, terbinafine treatment resulted in band shifts to 1409 cm^{-1}. Reversal of the terbinafine effect shifted this band back to 1403 cm^{-1}. There is a significant band at 1362 cm^{-1} in the IR spectrum of the carboxylate group in terbinafine treated SC. This band is characteristic of terbinafine.

COO^- IR spectra of SC treated with high RH in comparison to untreated and buffer treated SC with no RH applied, are displayed in Figure 3-7(B). Applied high RH shifts the COO^- band in EtOH buffer treated SC very close to the position of untreated and buffer control treated SC at 1403 cm^{-1} with no RH applied. At the same time, in the case of terbinafine treated SC, application of high RH results in a further shift of the band from 1409 cm^{-1} to 1414 cm^{-1}. This is different from RH effect on Amide I and II bands,

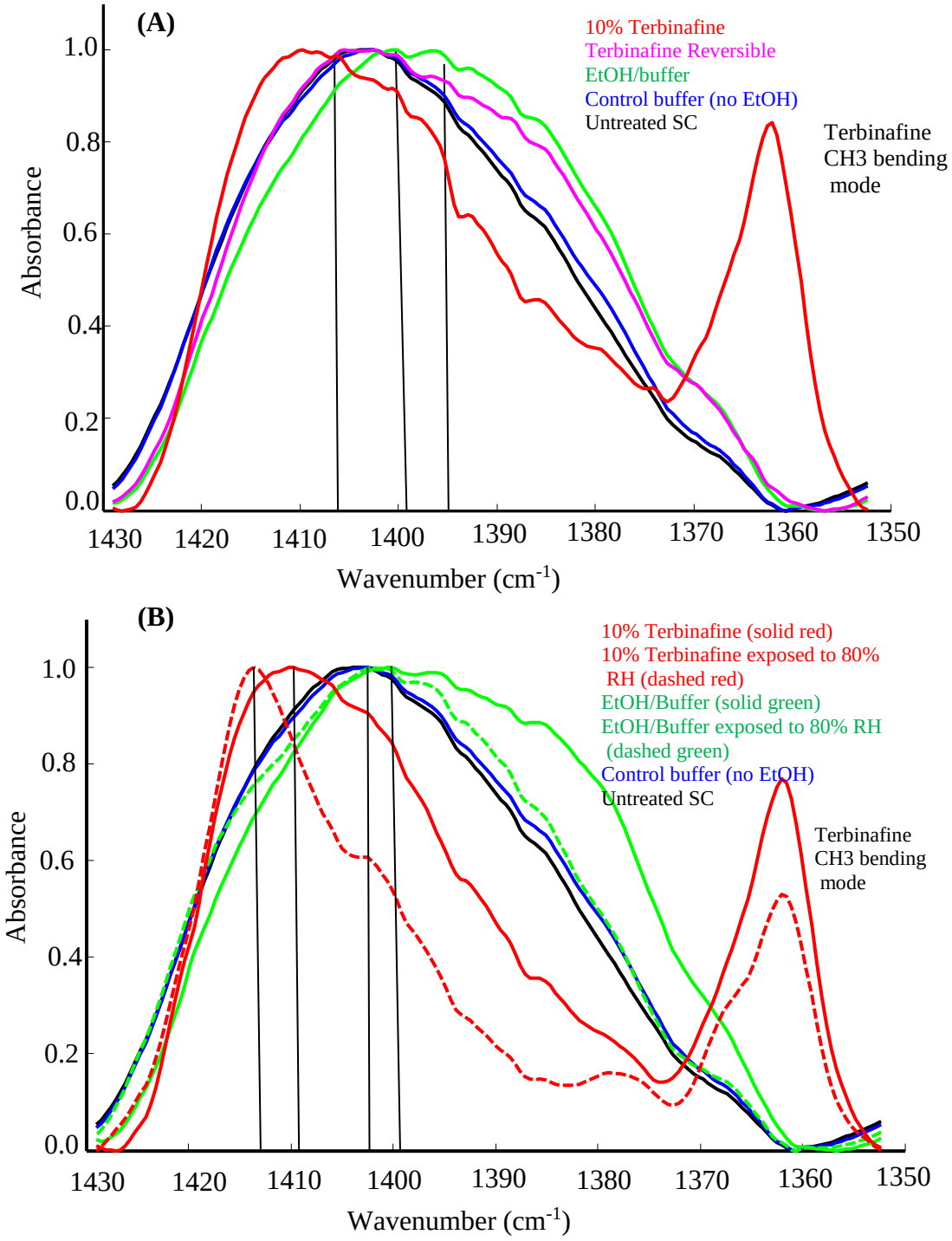

Figure 3-7 (A-B). IR spectra (1429-1352 cm^{-1}) of carboxylate groups in SC under various treatment conditions: (A) SC untreated (black), SC treated with buffer (no ethanol) (blue), SC treated with EtOH-containing buffer solution only (green), SC treated with terbinafine in EtOH buffer solution (red), reversible binding experiment (pink). (B) SC treated with 10% terbinafine before exposure to RH (red solid), SC treated with 10% Terbinafine after exposure to 80% RH (red dashed), SC treated with EtOH buffer solution only before exposure to RH (green solid), SC treated with EtOH buffer after exposure to RH (green dashed).

which revealed that those bands resumed the shape of untreated or buffer treated bands.

3.3.3 Terbinafine effect on lipids

Lipids in the SC are mostly packed as ordered orthorhombic or more fluid hexagonal phases[29]. These phases, and transitions between them, are usually monitored from the following IR features: CH_2 methylene rocking (711-735 cm^{-1}), CH_2 scissoring contour (1462, 1467, 1472 cm^{-1}), CH_2 symmetric stretching (2850.2-2853.5 cm^{-1}), CH_2 asymmetric stretching vibration (~2917-2918 cm^{-1})[18].

The methylene symmetric and asymmetric stretching frequencies demonstrate different sensitivities to molecular organization of SC. The CH_2 symmetric stretching band is sensitive mostly to changes in trans-gauche isomerization in the lipid chains. In Figure 3-8, the temperature dependence of this frequency (~2850 cm^{-1}) 2nd derivative is plotted over the temperature range 10-80°C. The CH_2 stretching band frequency at ~2850 cm^{-1} was monitored vs temperature. Plots of the 2nd derivative of the peak for untreated SC, control buffer treated SC (two data sets averaged results), control EtOH buffer treated SC (three data sets averaged results) and terbinafine treated SC (three data sets averaged results) demonstrated differences in transition temperature. In the case of untreated and buffer treated SC, the transition occurs at about 37-38ºC. However, control EtOH buffer and terbinafine treated SC exhibit a transition temperature of ~ 42°C. EtOH/buffer treatment produced an increase (~4°C) in the temperature of the orthorhombic to hexagonal packing transition compared to the untreated or buffer treated experiments. Possibly ethanol extracts short chain lipids, thus leaving longer fatty acids which tend to have higher

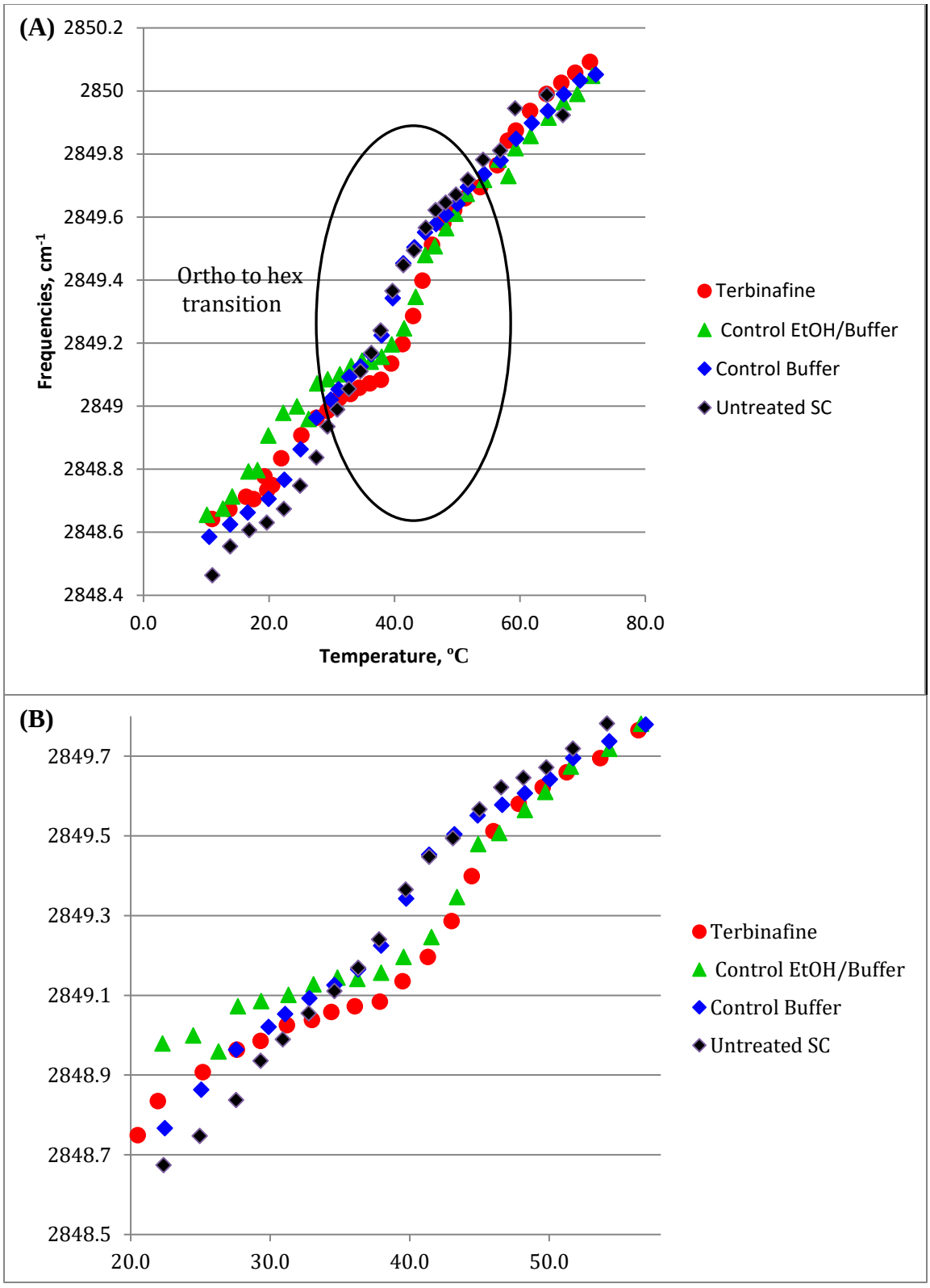

Figure 3-8 A-B. (A) 2nd Derivative symmetric CH_2 stretching frequency (cm^{-1}) vs temperature, °C (averaged), (B) phase transition region magnified

melting temperatures [30]. The effect of ethanol/buffer treatment on the ortho to hex lipid packing transition limits our ability to detect any possible further effect of terbinafine on this process.

3.4 Discussion

An understanding of how the SC barrier responds to an antifungal topical medicine provides mechanistic information important to the pharmaceutical industry and helps to design better drugs. In the current study, transmission IR spectroscopy helps to understand the effects of terbinafine on major SC constituents, namely keratin and lipids. Both EtOH and terbinafine have significant effects on keratin secondary and tertiary structure. The maximal absorption peaks of the Amide I and II bands at 1651 and 1543 cm^{-1} in native SC are assigned to the α-helix structure of keratin. Changes in the Amide I and II band shapes in Figure 3-2 (A) and (B) clearly demonstrate α-helix to β-sheet transition events, which have been shown in previous studies of keratin[31]. Mostly α-helical keratin (Amide I band at 1650 cm^{-1}) demonstrated increased peak intensity at 1628 cm^{-1} (typical for β-sheet structure) in response to treatments with EtOH/buffer and terbinafine. The maximal peak of the Amide II band at 1543 cm^{-1} associated with the α-helical structure, was transformed to a peak with a shoulder at 1516 cm^{-1} of increasing intensity depending on the nature of the experiment undertaken. This peak is indicative of β-sheet formation.

Figure 3-9 sums up Amide II β-sheet content values which are displayed in Figure 3-6(B). In the presence of EtOH (control) some of α-helical keratin is transformed to β-sheet, leading to a value of Δ AUC 4.9 β-sheet content present. Once SC is treated with 10% terbinafine in EtOH/buffer, further structural change occurs in keratin and the β-sheet content increases to 7.6. When terbinafine treated SC is washed with EtOH/buffer,

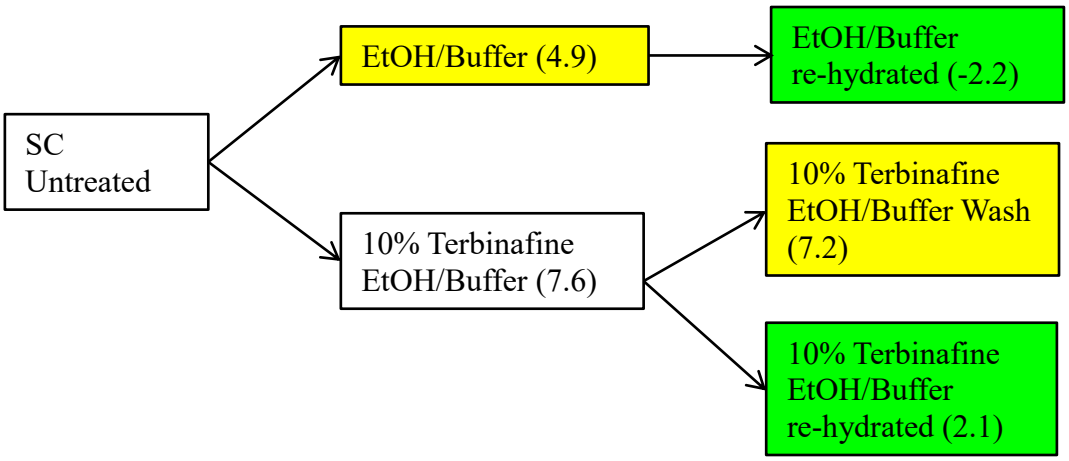

Figure 3-9. Amide II β-sheet content presence. Yellow boxes demonstrate effect of ethanol on β-sheet content, while green boxes show effect of exposure to RH on the keratin secondary structure.

the amount of bound terbinafine is reduced, and β-sheet formation is reduced to 7.2. Since terbinafine can be washed away with additional EtOH/buffer treatment, it shows that terbinafine is not a very strong keratin binder. Re-hydration of terbinafine or ethanol treated SC facilitates refolding of keratin into α-helices and the amount of β-sheets goes down to 2.1. It is reasonable to assume water displaces ethanol and restores hydrogen bonds that are important to support the α-helical configuration.

Keratin fibers consist of amino acids favoring a helix formation, namely lysine, aspartic acid, glutamic acid and leucine, cysteine and proline. Aspartic acid, glutamic acid and cysteine are acidic and comprise about 17% of all amino acids in keratin[32]. Keratin fibers are held together by cysteine rich proteins – which favor formation of disulfide bridges. Keratin filaments also possess additional weak bonds including Van der Waals's forces, hydrogen bonds and ionic bonds. At the uppermost layers of skin (30–0% SC depth), keratin chains are highly folded and persist in a most stable α-helix conformation form[33]. Thus, the water cannot intercalate into the keratin chains and there are limited vacancies for binding water molecules with keratin. However, due to such amino acids

such as leucine, it might be more prone to bind lipophilic molecules like terbinafine. As shown here and elsewhere, ethanol also is known to denature keratin, thus perhaps opening more binding sites for terbinafine[34]. When keratin chains are more unfolded and therefore the interaction between the side-chains of keratin is weak, the terbinafine molecules can intercalate more into keratin filaments and bind there. It was shown that glutamic acid side chains are important binding sites in α-helix keratin[35]. Consistent with this, Figure 3-7 (A) and (B) clearly demonstrate sensitivity of amino acids carboxylic groups (including glutamic) to the different terbinafine binding conditions.

Treatment of SC with terbinafine and subsequent removal by washing with EtOH/buffer (Figure 3-2A, magenta color spectrum) revealed that the terbinafine binding to keratin is not fully reversible within the 24-48 hours after treatment. The same results were achieved upon rehydration of terbinafine treated SC at ~ 80% RH, Figure 3-2 (B). It has been established[36] that the drug molecules did bind with the keratin in a reversible way. The favorable effect of a reservoir was thereby created, and the drug then can be released over time into the deeper and surrounding tissues. For example, defatted nail powder was treated with terbinafine and the release profile exhibited two phases[37]. An initial rapid release was followed by a slower sustained release. The time required to release 50% (t_{50}) and 80% (t_{80}) of total drug loaded was found to be 8 and 24 days, respectively. The fraction of drug retained in the nail powder after the study period (1 month) was found to be 0.14±0.02 μg/mg, which was 3.36±0.57% of the total drug loaded. This result suggested that the drug loaded into the nail powder was almost completely released and did not bind irreversibly to the nail keratin. Another study[38] confirmed high rates of terbinafine binding to keratin and its accumulation at high levels in the tissues when topically applied. It was

also reported[39] that active topical delivery of terbinafine via SC occurs within the first two hours with about 30% of the total amount of drug delivered, 31% delivered from 2-12 hours and 39% thereafter. SC levels of terbinafine were still detected 7 to 14 days after topical application. Washing terbinafine from the SC surface for 12 hours removed about 73% of the drug and induced a decrease in the terbinafine content. Also a gradient penetration of terbinafine was observed via topical transdermal application, with about 20-30% of the drug present in the lower levels of SC. The presence of ethanol enhanced the topical absorption of terbinafine[40]. Hence the partially reversible binding of terbinafine within 48 hours as observed in Figures 3-2(A) and 3-2 (B), is in agreement with findings reported by the other studies cited above.

Ethanol is commonly employed as a "permeability enhancer" for transdermal drugs and is well known to influence the lipid membrane in a dose dependent manner, disrupting packing and increasing lipid motion at low concentrations and selectively extracting lipids at moderate concentrations ≥30%[41]. In Figure 3-8 (A-B) the ortho to hexagonal transition temperature is shifted from 38ºC to 42ºC in SC treated both with EtOH/buffer and terbinafine in EtOH/buffer. Perhaps by extracting small disordered lipids, ethanol helps to stabilize lipid packing, thus increasing the transition temperature by 4ºC. The effect of ethanol on human stratum corneum and other tissues has been extensively discussed in the literature[14,37,38]. In an early study of rat liver plasma membranes, Lewis et. al. found an EtOH-induced statistically significant reduction in the methylene C-H frequencies. Lipid chain interdigitation was suggested as a possible cause of this effect. Bommannan et. al.[14]. used ATR-IR and demonstrated that pure EtOH treatment for 30 minutes led to extraction of appreciable amounts of lipids from the SC. The structural changes induced by ethanol

were reversed within 24 hr. More recently, Kwak et. al.[41] studied the effect of EtOH on an equimolar mixture of N-palmitoyl sphingosine (ceramide), palmitic acid and cholesterol. FT-IR and ^{2}H NMR spectroscopy were utilized to show that EtOH can have several parallel effects. Most notable were disruption of chain packing and increasing lipid motions at low concentrations and selective extraction of lipids at moderate concentrations. The current results add one additional element to the discussion. The data in Figure 8(A) show that EtOH/buffer treatment increases the midpoint temperature of the orthorhombic-to-hexagonal packing transition by about 4 degrees from 38ºC to 42ºC. This ordering effect, consistent with that observed by Kwak et. al., originates in the stabilization of chain packing, and probably arises from extraction of shorter chain lipid species. The effects at low temperature in Figure 8(A) are more difficult to understand, but the frequency changes between the control EtOH/buffer and terbinafine experiment in this buffer are of the order of ~0.1-0.2 cm^{-1}, close to the limit of current experimental precision.

Another study[42] revealed that different volume ratios in EtOH/water mixtures have an effect on ordered structures in intercellular lipids and soft keratin in the SC. All volume ratios in EtOH/water mixture greatly affected the short lamellar structure in the intercellular lipids and the fibril structures of the keratin. It had a negligible effect on the long lamellar structure in the intercellular lipids and the hydrocarbon-chain packing structures. The structural changes in SC due to the application of EtOH/water mixtures suggest that it is heavily involved in the skin permeability of topically applied drugs and terbinafine in formulations containing both EtOH and water.

3.5 Conclusion

It was demonstrated that IR can be successfully used to monitor structural changes in isolated SC induced by terbinafine under various treatment conditions. The most prominent changes were observed in Amide I and Amide II bands, which represent changes in secondary and tertiary structures of keratin. In addition, shifts were detected in the COO^- band, which confirm changes to tertiary structure of keratin. EtOH induces a significant baseline level of β-sheet in keratin, while terbinafine in EtOH significantly enhances β-sheet presence in keratin. The long term delivery effect of drug in SC might be achieved by terbinafine binding to the keratin. The terbinafine effect is partially reversible with EtOH wash. Rehydration allows keratin mostly to refold.

For the current study, the effect of EtOH on lipid packing seems to overwhelm any detectable additional effect of terbinafine on this property . This is also clearly evident in Figure 8. Finally, the importance of the current result is that the methods depicted here may be useful a useful general mechanism not just for monitoring structural changes in the SC induced by a wide variety of exogenous agents and formulations.

3.6 References

1. Alberti, I., Kalia, Y.N., Naik, A., Bonny, J.D., Guy, R.H., "In vivo assessment of enhanced topical delivery of terbinafine to human stratum corneum", *Journal of Controlled Release*, **2001**, 71, pp. 319–327.

2. Alberti, I., Kalia, Y.N., Naik, A., Bonny, J., Guy, R.H., "Effect of ethanol and isopropyl myristate on bioavailability of topical terbinafine in human stratum corneum in vivo", *International Journal of Pharmaceutics*, **2001**, 219, pp.11-19.

3. Alberti, I., Kalia, Y.N., Naik, A., Guy, R.H., "Assessment and prediction of the cutaneous availability of topical terbinafine, in vivo, in Man", *Pharmaceutical Research*, **2001**, 18(10), pp.1472-1475.

4. Dapic, I., Jakasa I., Yau N.L.H., Kezic S., "Evaluation of an HPLC Method for the Determination of Natural Moisturizing Factors in the Human Stratum Corneum", *Analytical Letters*, **2013**, 46(14), pp. 2133-2144.

5. Ryder, N.S., "Terbinafine: Mode of action and properties of the squalene epoxidase inhibition", *British Journal of Dermatology*, **1992,** 126, Supplement 59, pp.2-7.

6. Li, B.S., Cary, J.H., Maibach H.I., "Stratum corneum substantivity: drug development implications", *Archives of Dermatological Research*, **2018**, 310, pp.537–549.

7. Kienzler J.L., Queille-Roussel, C., Mugglestone, C., Ortonne, J.P., Larnier, C., " Stratum corneum pharmacokinetics of the anti-fungal drug, terbinafine, in a novel topical formulation, for single-dose application in ermatophytoses", *Curr Med Res Opin*., **2007**,23(6), pp. 1293–1302.

8. Erdal, M.S., Peköz, A.Y., Aksu, B., Araman, A., "Impacts of chemical enhancers on skin permeation and deposition of terbinafine", *Pharmaceutical Development and Technology*, **2014**, pp.565-570.

9. Prausnitz, M.R., Elias, M.P., Franz, T.J, Schmuth, M., Tsai, J.C., Menon, G.K., Holleran, W.M., Feingold, K.R., "Skin Barrier and Transdermal Drug Delivery", **2012**, Medical Therapy Section 19, pp.2065-2073.

10. Bronaugh, R.L., Maibach, H.I., "Percutaneous Absorption: Drugs-Cosmetics-Mechanisms Methodology" , **2005**, *4th edn . New York : Marcel Dekker*.

11. Williams, A.C. , Barry, B.W., "Penetration enhancers", *Adv Drug Deliv Rev* . 56, **2004**, pp. 603 – 618.

12. Goates, C.Y., Knutson, K., "Enhanced permeation of polar compounds through human epidermis. I. Permeability and membrane structural changes in the presence of short chain alcohols", *Biochim. Biophys. Acta*, **1994,** pp.169–179.

13. Moghadam, S., Saliaj, E., Wettig,, S.D., Dong C., Ivanova, M.V., Huzil, J.T., Foldvari, M., "Effect of Chemical Permeation Enhancers on Stratum Corneum Barrier Lipid Organizational Structure and Interferon Alpha Permeability", *Mol. Pharmaceutics*, **2013**, *10* (6), pp 2248–2260.

14. Bommannan, D., Potts, R.O., Guy, R.H., "Examination of the effect of ethanol on human stratum corneum in vivo using infrared spectroscopy", *J. Controlled Release*, **1991**, 16, pp. 299-304.

15. Kim, Y.C., Park, J.H., Ludovice, P.J., Prausnitz, M.R.., "Synergistic enhancement of skin permeability by N-lauroylsarcosine and ethanol", *Int. J. Pharm*., **2008**, 352, pp.129–138.

16. Merle, C., Baillet-Guffroy, A.,"Physical and chemical perturbations of the supramolecular organization of the stratum corneum lipids: in vitro to ex vivo study", *Biochim. Biophys. Acta*, **2009**, 1788, pp.1092–1098.

17. Hatta, I., Nakazawa, H., Obata, Y., Ohta, N., Inoue, K., Yagi, N., "Novel method to observe subtle structural modulation of stratum corneum on applying chemical agents", *Chem. Phys. Lipids*., **2010**, 163, pp.381–389.

18. Pensack, R.D., Michniak, B.B., Moore, D.J., Mendelsohn, R., "*Infrared kinetic/structural studies of barrier reformation in intact stratum corneum following thermal perturbation*" *Appl Spectrosc.*, **2006**, 60 (12), pp.1399-404.

19. Li, R.Y., Wang, A.P., Xu, J.H., Xi, L.Y., Fu, M.H., Zhu, M., Xu, M.L., Li, X.Q., Lai, W., Liu, W.D., Lu, X.Y., Gong, Z.Q., "Efficacy and safety of 1 % terbinafine film-forming solution in Chinese patients with tinea pedis: a randomized, double-blind, placebo-controlled, multicenter, parallel-group study", *Clin Drug Investig.*, **2014,** 34(3), pp.223-30.

20. Massart, D. L.,Vandeginste, B. G. M., Deming, S. N., Michotte, Y., Kaufman, L., "Chemometrics: A Textbook", **1988**, pp.250-251.

21. Oertel, R. P., "Protein conformational changes induced in human stratum corneum by organic sulfoxides: An infrared spectroscopic investigation", *Biopolymers*, **1977**, 16 (10), 2329-2345.

22. Miyazawa, T., "Perturbation Treatment of the Characteristic Vibrations of Polypeptide Chains in Various Configurations", *The Journal of Chemical Physics,* **1960,** 32, pp.1647 -1652.

23. Miyazawa, T., Blout, E.R., "The Infrared Spectra of Polypeptides in Various Conformations: Amide I and II Bands", *J. Am. Chem. Soc.*, **1961**, 83, pp. 712–719.

24. Moore, D., Rerek, M.E., Mendesohn, R., "Role of ceramides 2 and 5 in the structure of the stratum corneum lipid barrier", *International Journal of Cosmetic Science,* **1999**, 21, pp. 353–368.

25. Venyaminov, S.Y., "Quantitative IR Spectrophotometry of Peptide Compounds in Water (H20) Solutions. 1. Spectral Parameters of Amino Acid Residue Absorption Bands"**,** *Biopolymers*, **1990**, 30, pp.1243-1257.

26. Mendelsohn, R., Anderle, G., Jaworsky, M., Mantsch, H.H., Dluhy, R.A., "Fourier transform infrared spectroscopic studies of lipid-protein interaction in native and reconstituted sarcoplasmic reticulum", *Biochimica et Biophysica Acta*, **1984**, 775, 215-224.

27. Zhao Y., Chen, L., Han, L., Mantalaris, A., Pistikopoulos, E.N, Marzinek, J., Lian, G., Bond, P.J., Noro, M.G., "Molecular and thermodynamic basis for EGCG-Keratin interaction-part I: Molecular dynamics simulations", *AIChE Journal*, **2013**, 59(12), pp.4816-4823.

28. Nara, M., Tanokura, M., Yamamoto, T., Tasumi, M., "A comparative study of the binding effects of Mg2+, Ca2+, Sr2+ and Cd2+ on calmodulin by fourier-transform infrared spectroscopy", *Biospectroscopy*, **1995**, 1, pp.47-54.

29. Boncheva, M., Damien, F., Normand, V., "Molecular organization of the lipid matrix in intact Stratum corneum using ATR-FTIR spectroscopy", *Biochimica et Biophysica Acta (BBA) - Biomembranes*, **2008**, 1778(5), pp.1344-1355.

30. Stryer, L., "Fatty Acids Are Key Constituents of Lipids", *Biochemistry. 5th edition,* **2002**.

31. Lin, S., Duan, K., Lin, T., "Simultaneous determination of the protein conversion process in porcine stratum corneum after pretreatment with skin enhancers by a combined microscopic FT-IR/DSC system", *Spectrochimica Acta Part A,* **1996**, 52, pp.1671-1678.

32. Strnad, P., Usachov, V., Debes, C., Gräter, F., Parry, D.A., Omary, M.B., "Unique amino acid signatures that are evolutionarily conserved distinguish simple-type, epidermal and hair keratins", *J Cell Sci*., **2011**, 124(24), pp.4221-4232.

33. Choe, C.-S., Schleusener, J., Lademann, J., Darvin, M.E., "Keratin-water-NMF interaction as a three layer model in the human stratum corneum using *in vivo* confocal Raman microscopy"**,** *Scientific Reports*, **2017**, 7: pp. 15900.

34. Horita, D., Hatta, I., Yoshimoto, M, Kitao, Y., Todo, H., Sugibayashi K.,"Molecular mechanisms of action of different concentrations of ethanol in water on ordered structures of intercellular lipids and soft keratin in the stratum corneum", *Biochimica et Biophysica Acta*, **2015**, 1848, pp. 1196–1202.

35. Zhao, Y., Marzinek, J.K, Bond, P.J., Chen, L., Li, Q., "A study on Fe^{2+} -α-helical-rich keratin complex formation using isothermal titration calorimetry and molecular dynamics simulation", *Journal of Pharmaceutical Science*, **2014**, 103, pp.1224-1232.

36. Nair, A. B., Kim, H.D., Chakraborty, B., Singh, J., Zaman, M., Gupta, A., Friden, P.M., Murthy, S.N., "Ungual and trans-ungual iontophoretic delivery of terbinafine for the treatment of onychomycosis", *Journal of Pharmaceutical Sciences*, **2009**, 98(11), pp.4130-4140.

37. Sugiura, K., "The Low Keratin Affinity of Efinaconazole Contributes to Its Nail Penetration and Fungicidal Activity in Topical Onychomycosis Treatment", *Antimicrob Agents Chemother.*, **2014**, 58(7), pp. 3837–3842.

38. Tatsumi, Y., Yokoo, M., Senda, H., Kakehi, K., "Therapeutic efficacy of topically applied KP-103 against experimental tinea unguium in the guinea pigs in comparison with amorolfine and terbinafine", *Antimicrobial Agents and Chemotherapy*, **2002**, 46(12), pp.3797-3801.

39. Kienzler, J.-L., Queille-Roussel, C., Mugglestone, C., Ortonne, J.P., Larnier, C., "Stratum corneum pharmacokinetics of the anti-fungal drug, terbinafine, in a novel topical formulation, for single-dose application in dermatophytoses", *Current Medical Research and Opinion*, **2007**, 23(6), pp.1293-1302.

40. Alberti, I., Kalia, Y.N., Naik, A., Bonny, J., Guy, R.H., "Effect of ethanol and isopropyl myristate on the availability of topical terbinafine in human stratum corneum, in vivo", *Int. J. Pharm.*, **2001**, 219, pp.11-19.

41. Kwak, S., Brief, E., Langlais, D., Kitson, N., Lafleur, M., Thewalt, J., "Ethanol perturbs lipid organization in models of stratum coenreum membranes: An

investigation combining differential scanning calorimetry, infrared and ^{2}H NMR spectroscopy", *Biochimica et Biophysica Acta*, **2012**, 1212, pp.1410-1419.

42. Lewis, N., Levin, I.W., Steer, C.J., "Infrared spectroscopic study of ethanol-induced changes in rat liver plasma membrane", *Biochimica et Biophysica Acta*, **1989**, 986, pp. 161-166.

Chapter 4: Comparison Of Hydration Levels In Human Skin Upon Application of Commercial Moisturizers By Confocal Raman Microscopy

4.1 Introduction

The SC, the outer most layer of skin, is a terminally differentiated epithelium that provides the essential barrier between the environment and the interior structure. For practical biological purposes it is waterproof. The tissue consists of impermeable fully differentiated epithelial cells ("corneocytes") connected by a network of intercellular junctions (corneodesmosomes") and immersed in stacks of unusual biological membranes ("stratum corneum intercellular membranes"). These membranes are thought to be the rate limiting step in, for example, the transdermal passive diffusion of water[1].

For cosmetic purposes, skin hydration is important for healthy looking skin. Favorable skin conditions including suppleness, smoothness, youthfulness, and radiance, have been attributed to a good skin moisturization[2]. With increasing age, water content decreases in skin. This is usually manifest as rough and dry skin, with a clinically dull appearance and loss of radiance, firmness, and suppleness.

Light interacts with skin at and beneath the skin surface, thus providing a youthful, radiant appearance. A small portion of light (~4-7%) is reflected off the stratum corneum as surface reflected light, while the majority of the light (~93-96%) penetrates into deeper skin layers. There it is back-scattered as subsurface reflected light[3,4]. Hydration enhances skin radiance by reducing surface roughness, structural disorganization of the stratum corneum, and optical heterogeneity between subsurface components. All these mechanisms of action promote deeper penetration of incoming light. As a result, back

scattered light increases from deeper skin layers to the skin surface and promotes a diffused lighting effect.

Moisturizers are frequently formulated as oil-in-water (o/w) emulsions, where oil droplets are dispersed in water and stabilized by emulsifiers[5]. There are two types of emulsions: creams and lotions, dependent on their viscosities. Gels also might be moisturizers with only hydrophilic material or ointments with only lipophilic ingredients. Moisturizers vary in complexity from simple compositions with only a few ingredients, to much more complex mixtures of many substances. In the case of o/w emulsions, the simplest possible moisturizers must contain three ingredients: water, lipid (oil), and emulsifier. Many of the ingredients used in moisturizers are the same as those found in the epidermis or on the skin surface, and may include fatty acids, ceramides, vitamins, urea, lactic acid, pyrrolidone carboxylic acid (PCA), etc. Lipids can be of vegetable, animal or mineral origin. Emulsifiers, which stabilize the lipid droplets in an emulsion, are either low-molecular weight substances, e.g., PEG-100 stearate, or long-chained polymers of large size, such as acrylates/C10–30 alkyl acrylate cross polymer. However, frequently emulsions have more than three ingredients, and usually mixtures of at least 15–20 substances. Those additional ingredients help to prepare moisturizers with desired properties, efficacy, and stability of the product. Moisturizers usually contain humectants, such as polyols: glycerin, propylene glycol, butylene glycol, sorbitol; alpha-hydroxy acids (AHAs) and their salts, e.g., sodium lactate, along with low-molecular weight substances such as urea, betaine, amino acids; and high-molecular weight polymers with water-binding capacity: sodium hyaluronate. To increase stability of the emulsion and to adjust its rheology, viscosity-increasing agents must be added into the formulation. Those agents

are polymers such as carbomer, acrylate copolymer and xanthan gum, along with high-melting waxes: glyceryl stearate, cetearyl alcohol. Sensory properties may be modified with silicones, such as dimethicone and cyclohexasiloxane. Additionally, moisturizers may contain additional ingredients, such as antioxidants, vitamins, herbal extracts, salts, and UV filters. Moisturizer pH can be adjusted to between slightly acidic and slightly alkaline and usually ranges from 4 to 7.

Moisturizers have therapeutic and cosmetic purposes, such as increasing skin water content and improvement in skin optical properties such as radiant appearance. However it is a big challenge for any moisturizing formulation to deliver sufficient quantities of water to the SC. The key ingredient of many humectants is glycerin[6], known for its hygroscopic character and large water binding capacity. Used for this purpose, it helps the SC to absorb water by attracting water from dermis and a humid environment into the epidermis[7]. However traditional humectant moisturizers, e.g., Cetaphil (CP), cannot continuously provide water absorption. A deeply hydrating cream "Dermal Replenishment (DP)" by Neostrata J&J, was formulated with naturally occurring SC components including NMF amino acids blend, glycerin and a sugar derivative to attract water and strengthen the skin moisture barrier. It also contained a complex of potent antioxidants and antiaging agents, including chardonnay grape seed extract, polyhydroxy acid (PHA) maltobionic acid, along with N-acetyl glucosamine and N-acetyl tyrosinamide to protect against external aggressors and help diminish the signs of aging. NMFs are naturally occurring in SC humectants or hygroscopic water soluble substances. The NMF is composed principally of free amino acids, and various derivatives of these amino acids such as PCA (the sodium salts of this acid are more hygroscopic than glycerin), urocanic

acid (a natural absorber of ultraviolet [UV] light), and inorganic salts, sugars, as well as lactic acid and urea[8,9,10]. Inorganic salts identified include the chlorides, phosphates, and citrates of sodium, potassium, calcium, and magnesium. The NMF is packaged within the corneocytes, making up approximately 10 percent of the corneocyte mass[11] and 20 percent to 30 percent of the dry weight of the stratum corneum.[12] NMF components are highly efficient humectants that attract and bind water from the atmosphere, drawing it into the corneocytes. This process can occur even at a relative humidity as low as 50 percent, allowing the corneocytes to maintain an adequate level of water in low-humidity environments[14]. The water absorption is so efficient that the NMF essentially dissolves within the water it has absorbed. Hydrated NMF (particularly the neutral and basic amino acids) forms ionic interactions with keratin fibers, reducing the intermolecular forces between the fibers and thus increasing the elasticity of the stratum corneum.[20] This elasticity serves to make the skin appear healthy and supple and to help prevent cracking or flaking due to mechanical stress [13].

Currently there are two major widely accepted methods to evaluate water content of SC: trans epidermal water loss (TEWL) and thermal conductivity. The skin water-loss barrier is not perfect. Water from the VE can escape through the SC into the ambient air, due to a water vapor pressure gradient between the two sides of the skin barrier[15]. This is the essence of TEWL. TEWL can be measured to give information about the quality of the skin water-loss barrier. The lower the TEWL the better the barrier. Thus TEWL is an indicator of the quality of the skin water-loss barrier. TEWL is measured by evaporimetry. However TEWL does not provide information about spatial distribution of water in the SC or VE. In the SC, water exists in two thermodynamically very different states: free water,

in which numerous ionized and non-ionized molecules are dissolved (metal salts, amino acids, urea) and bound water in interaction with the proteins and lipids of the SC. The last one accounts for 20–30 % of the total volume of water contained in the water-saturated layer. Bound water has mainly been studied by thermal conductivity methods[15]. The human skin shows a very high electrical resistance which is due to the properties of the SC.

Confocal Raman spectroscopy (CRS) offers advantages over TEWL and water loss electrical conductivity for the study of skin hydration. It can evaluate spatial distribution and relative water content in *ex vivo* and *in vivo* skin. In this study, a traditional moisturizer CP was compared to an advanced hydration moisturizer DR and also with untreated skin. CRS directly measures O-H vibrational modes providing direct information on relative water content inside skin at different depths. CRS has been used to measure water concentration profiles at different body sites such as cheek, upper arm, volar forearm and back of the hand[16], thus demonstrating the utility of our approach for analyzing skin hydration. In addition, CRS can help to visualize SC and VE by monitoring lipid-to-protein ratio 2880/2930 cm^{-1}, as well as to evaluate barrier function by monitoring 1127/1003 cm^{-1} ratio.

4.2 Materials and Methods

4.2.1 Materials

Cetaphil moisturizing lotion (Galderma, Fort Worth, TX, USA) and Neostrata dermal replenishment (Neostrata Co., Inc., Princeton, NJ, USA) were used for ex-vivo skin treatments. The Cetaphil ingredients are water, glycerin, hydrogenated polyisobutene, ceteareth-20, cetearyl alcohol persea (avocado oil), tocopheryl acetate (vitamin e), dimethicone gratissima, sodium levulinate, sodium anisate, caprylyl glycol, benzyl alcohol,

panthenol, stearoxytrimethylsilane, stearyl alcohol, citric acid, acrylates/C10-30, alkyl acrylate crosspolymer. The Neostrata active ingredients are SynerG formula Aminofil®, NeoGlucosamine®, maltobionic acid Prodew®, peptides. Neostrata's other ingredients are: water, glycerin, maltobionic acid, acetyl glucosamine, octyldodecyl neopentanoate, steareth-2, hydroxyethyl acrylate/sodium acryloyldimethyl taurate copolymers, isostearic acid, cyclopentasiloxane, acetyl tyrosinamide, saccharise isomerate, cyclohexasiloxane, palmytoyl tripeptide-1, palmitoyl tetrapeptide-7, vitis vinifera (grape) seed extract, sodium PCA, serine, glycine, alanine, lysine, arginine, threonine, proline, cetyl alcohol, propylene glycol, betaine, sorbitol, isopropyl myristate, glutamic acid, butylene glycol, polysorbate 60, sorbitan isostearate, carbomer, polysorbate-20, ammonium hydroxide, disodium EDTA, caprylyl glycol, sodium bisulfite, xanthan gum, phenoxyethanol, chlorphenesin, methyldihydrojasmonate, isobutyl methyl tetrahydropyranol, ethylene brassylate, methyl decenol, Cl 14700 (red 4), Cl 19140 (yellow 5).

Human abdominal skin from plastic surgery was obtained from dermatological offices with informed consent and ethics board approval from each office. Skin sections were wrapped in aluminum foil, fast frozen with liquid nitrogen and stored at -20°C for no more than 6 months prior to usage.

4.2.2 Methods

Sample Preparation

Skin was cut about 2 x 2 cm pieces using stainless steel surgical blades, defrosted and cleaned with Q-tips to remove any possible excess of sebum. It was then mounted in

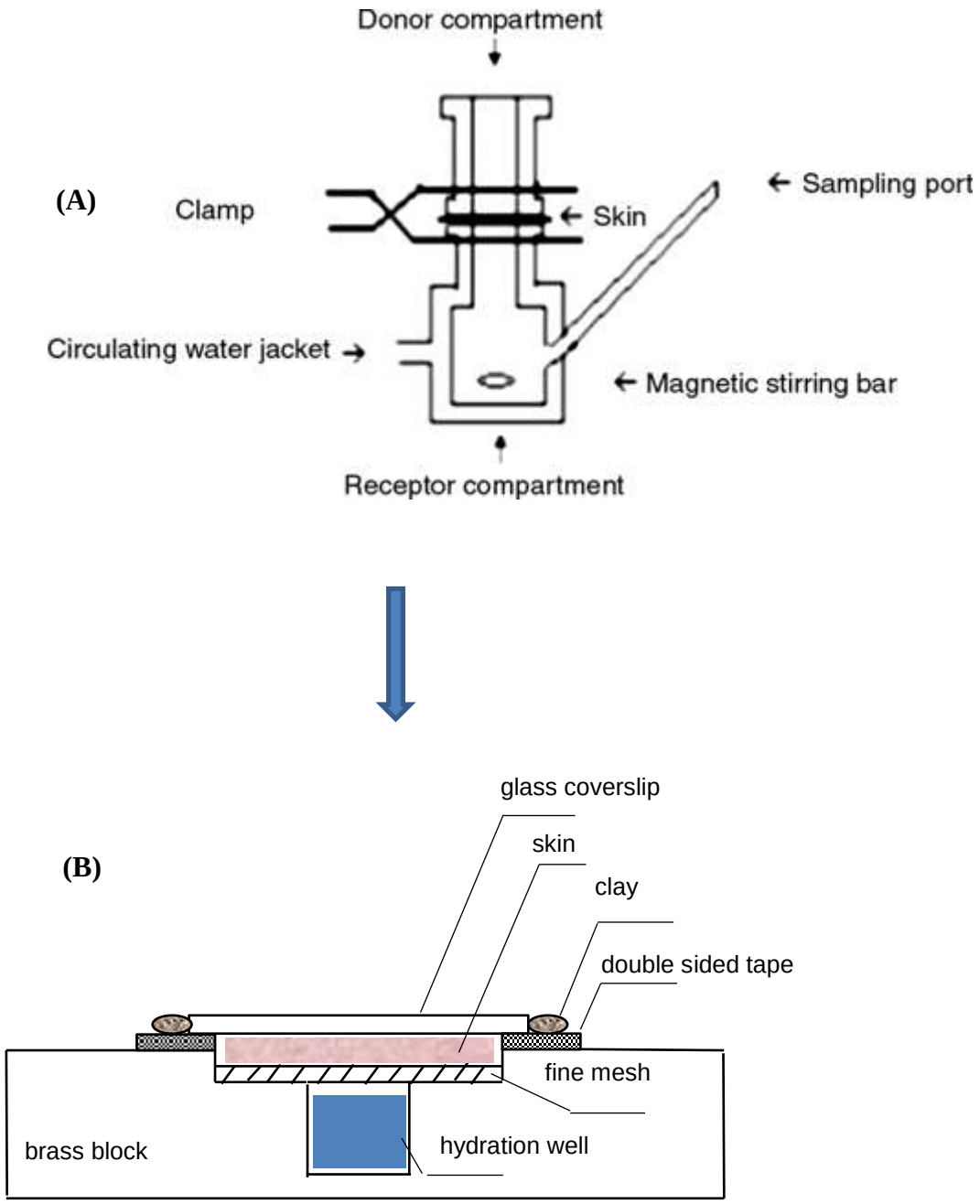

Figure 4-1. (A) Schematic of FDC experimental set up. (B) Cross section schematic of the homemade sample holder used to acquire Raman skin images.

a Franz diffusion cell (FDC) and 20 µL of product was applied on the skin surface at the donor compartment (nothing was applied to the surface of the untreated control). See Figure 4-1 (A) for FDC set up. 1X PBS buffer was added to receptor compartment in order to keep ex vivo skin properly hydrated. The sample was incubated at 34^{o}C for 24 hours in a hydrated environment. Following incubation, excess product was removed from the skin surface. Skin was removed from the FDC and trimmed to fit in the sample cell designed for Raman measurements (see Figure 4-1 B). Skin was sealed in the cell in a hydrated environment with a glass coverslip in close contact with skin surface.

Raman measurements and analysis

A WITec Alpha-300R Plus confocal Raman microscope (Ulm, Germany) equipped with a 532 nm laser and a 100X oil immersion objective (NA 1.25) was used for the experiments. Spectra were collected at room temperature with a laser power of 20mW. Data acquisition and analysis were accomplished using WITec Project Plus 4.1 software. XZ image planes (skin depth profiles) were acquired, typically over 80x60 µm^2, using 2 µm steps and a 5s integration time. Two image planes (from about the same location in skin) were acquired for each experiment, and each experiment was conducted three times.

Initial data treatment included cosmic ray removal and baseline correction (Project Plus shape option with a size of 120 and noise factor of 1). Cluster Analysis (K-Means: without background, Euclidean normalization and distance mode, and an average of 4 clusters) was used to mask the top glass layer, thereby defining the skin surface. The integrated area of peaks (sum) and intensity at parameters noted below were used to obtain the relative concentration of water, Figure 4-2. The wavenumber ranges used are as

follows: OH stretching sum (3083.9-3675.4 cm^{-1}), CH stretching sum (2809.3-3019.3 cm^{-1}) and Amide I max (1629.5-1676.1 cm^{-1}). Images of relative water content were measured from the OH sum peak/Amide I max peak ratio. The boundary location between SC and VE was estimated from the intensity ratio of the CH_2 asymmetric stretch sum 2880/CH_3 symmetric stretch protein sum 2930 cm^{-1} [17]. Barrier function was evaluated as a ratio of CC stretch sum 1127/ phenyl ring CC stretch sum 1003 cm^{-1}.

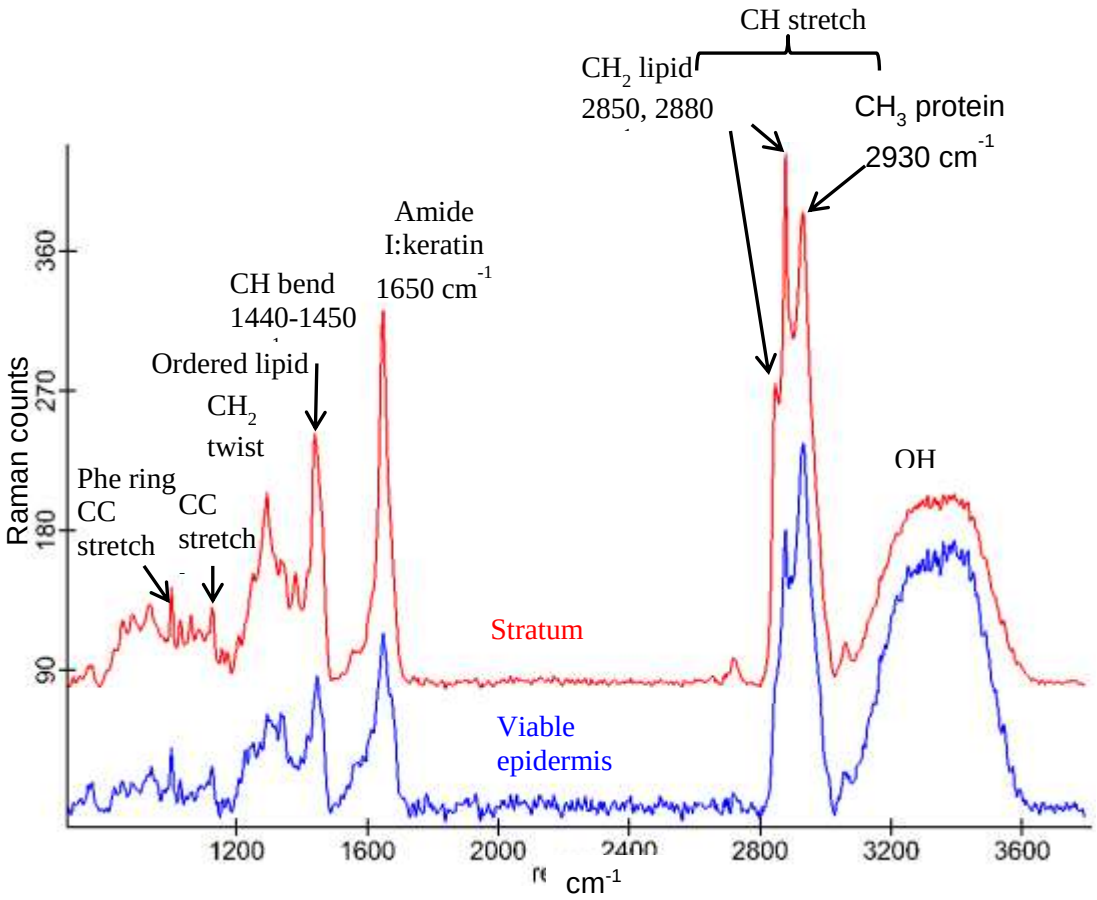

Figure 4-2. Raman spectra of epidermal regions in skin (average, normalized)

To perform quantitative comparisons among samples and to determine whether two independent samples were selected from populations having the same distribution, statistical analyses of data were completed. The *t*-test is the standard test for testing that the

difference between population means for two non-paired samples are equal. If the populations are not normal distributions, particularly for small samples, then the *t*-test may not be valid. The Whitney-Mann rank sum test is an alternative that can be applied when distributional assumptions are suspect. Sigma Plot 2000 software was used. To form the rank sum test, combined samples are ranked. Then the sum of the ranks for sample one, T_1, and the sum of the ranks for sample two, T_2 is computed. If the sample sizes are equal, the rank sum test statistic is the minimum of T_1 and T_2. If the sample sizes are unequal, then T_1 equals the sum of the ranks for the smaller sample is found. Then $T_2 = n_1(n_1 + n_2 + 1) - T_1$ is computed. T is the minimum of T_1 and T_2. Sufficiently small values of T cause rejection of the null hypothesis that the sample means are equal.

4.3 Results and Discussion

The effect of moisturizers on the SC was evaluated by tracking barrier function and water content. A series of different filters and data treatment techniques were developed to evaluate the following parameters: the boundary between SC and VE, the relative water content, and SC barrier function. The boundary between the SC and VE was delineated using the lipid to protein ratio (see Methods section). The resulting delineated skin images are shown in Figure 4-3. The more red areas are lipid-rich SC, while more green areas represent VE (richer in proteins). Figure 4-3 shows the following conditions: 1) untreated, 2) treated with CP, 3) treated with DR. All experiments were repeated three times, with two images per treatment condition. Lipid rich areas of SC (red) were used to create masks to clearly delineate SC from VE. Based on the resulted lipid rich areas of SC, masks were created. Those masks were further applied to images with water distribution in order to

make proper conclusions about water content in SC and VE depending on applied treatment.

The determination of relative water content is demonstrated in Figure 4-4 (A). Red represents areas with high water content and purple represents areas with low water concentration. Just by visualizing the image, it is possible to conclude that more blue/turquoise colors are present in the SC treated with CP, than in untreated or DR treated SC. The highest levels of red/yellow colors are present in DR treated SC. For proper quantitative comparisons among samples and to determine whether two independent samples were selected from populations having the same distribution, the Mann-Whitney rank sum test was used. All box plots in Figure 4-4 (B) demonstrated significant differences ($P<=0.001$) for all sample comparisons. In comparison to the untreated SC, DR treated SC demonstrated a 27.4% increase in water content. In comparison to CP treated SC, DR treated SC showed a 61.7% increase in moisture content. CP treated SC didn't show any increase in moisture content in comparison to untreated SC. In fact it decreased by 21.2%. The box plot representing skin treated with the NMF moisturizer clearly stands out from the two other samples, in SC skin sections. Figure 4-4 (A) shows the delineation of VE and water content in that area. Compared to untreated SC, water content increases by 1.8% in DR treated SC. Compared to CP treated SC, water content increases by 2.2% in DR treated SC. Overall, treatment with the NMF containing formula significantly increased the relative water content in the SC by 61.7% and in the VE by 2.2% as compared to the untreated control (based on mean values). In contrast, samples treated with a common humectant moisturizer (CP) didn't show increase in water content in SC and increased it only by 1.8% in VE, when compared to untreated control.

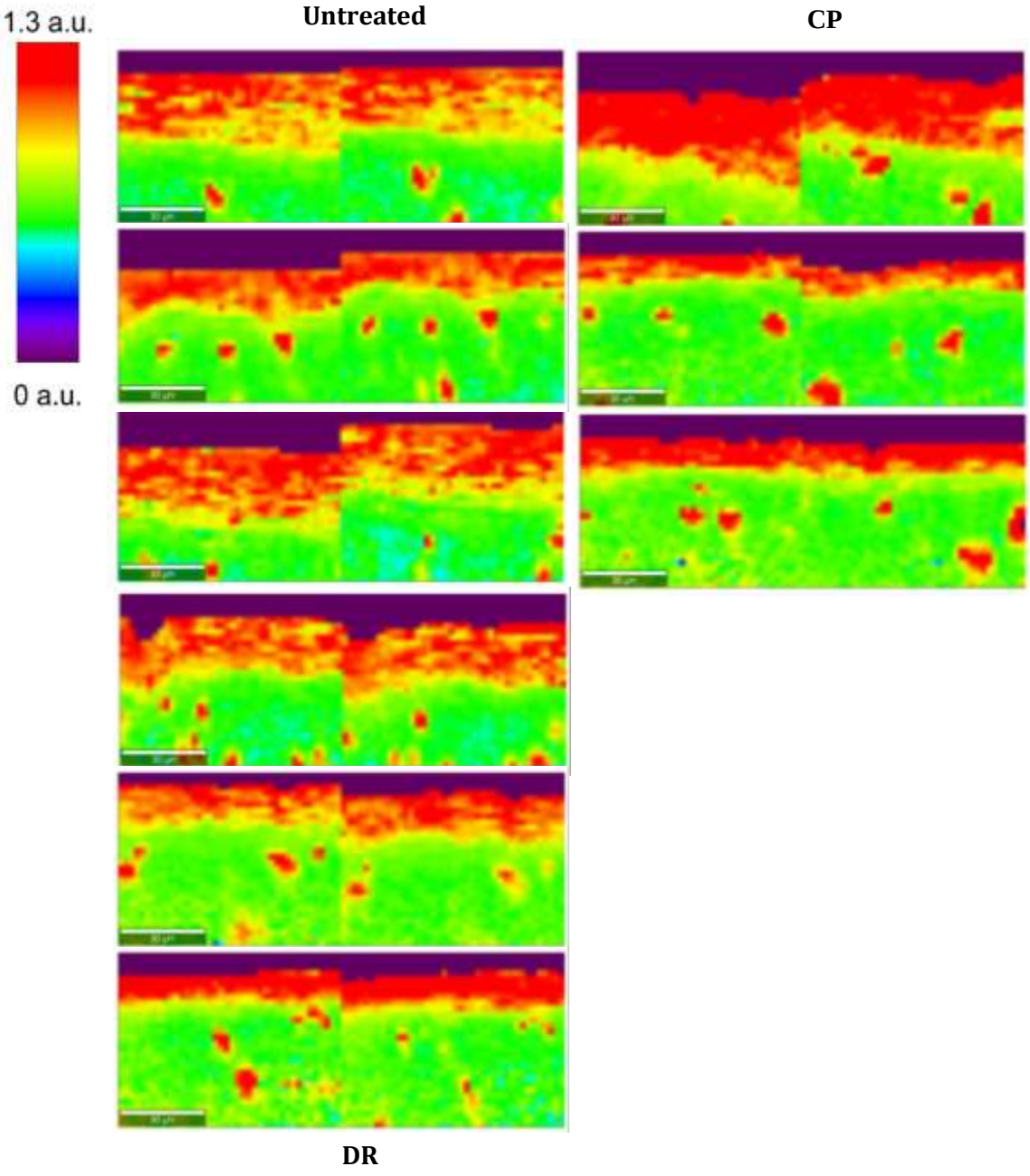

Figure 4-3. Delineation of SC/VE boundary using intensity ratio (CH_2 asymmetric stretch 2880/ CH_3 symmetric stretch 2930 cm^{-1}).

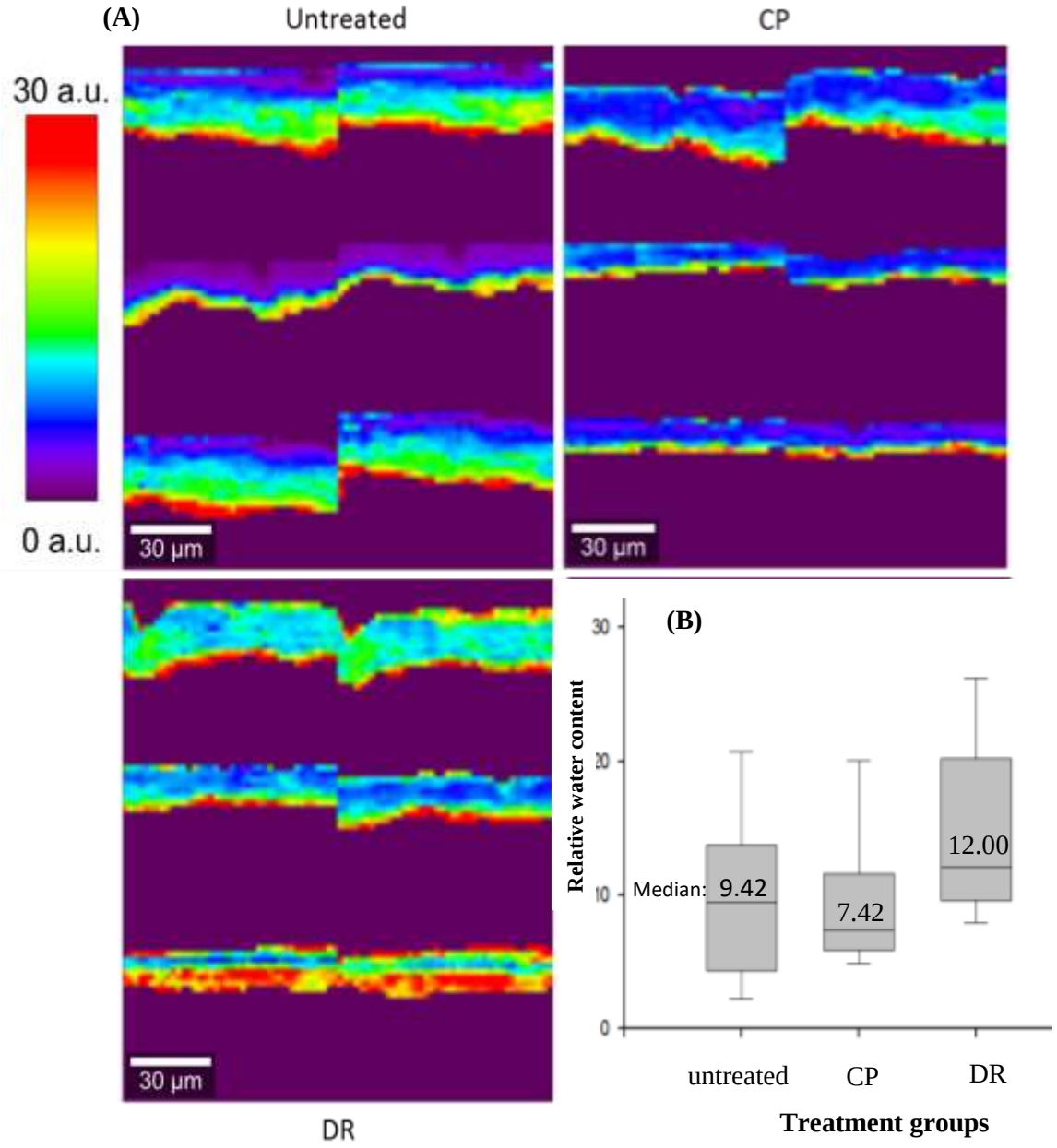

Figure 4-4. Relative water content vs treatments in delineated SC (A) Relative water content vs treatments: untreated, CP, DR (B) Mann-Whitney Rank Sum Test pairwise comparisons: untreated vs each treatment. There is a significant difference for all comparisons (P<=0.001).

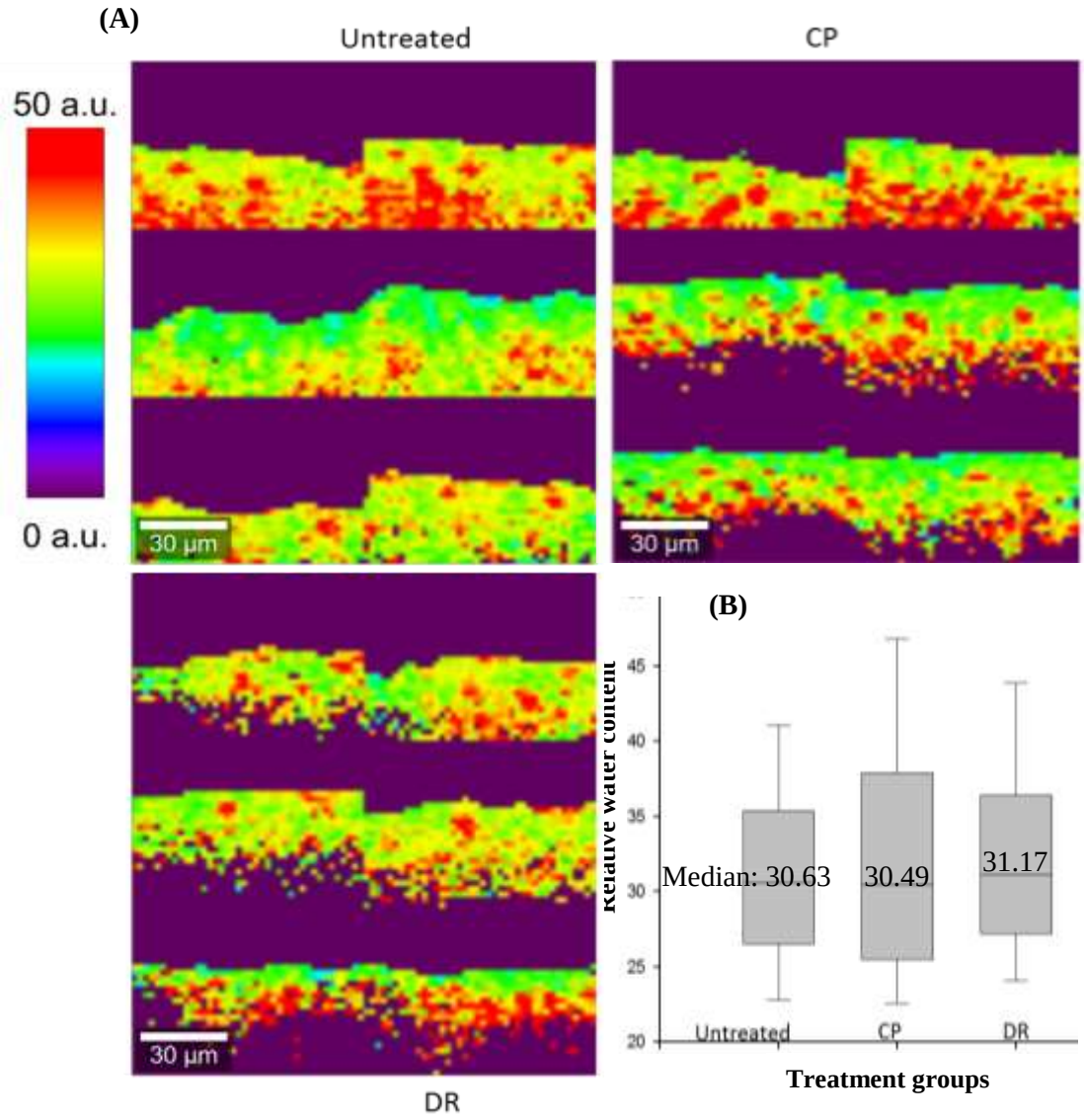

Figure 4-5. Relative water content (Sum H_2O/Sum Amide I) vs treatment in delineated VE (A) Relative water content (Sum H_2O/Sum Amide I) in delineated VE (S/N>3), (B) Mann-Whitney Rank Sum Test pairwise comparisons between treatments: statistically significant difference between CP & DR (P=0.005); no statistically significant difference between untreated and CP (P=0.94); statistically significant difference between untreated and DR (P<=0.001).

In contrast, samples treated with a common humectant moisturizer (conentCP) didn't show increase in SC water content and increased it only by 1.8% in the VE, when compared to untreated control.

Amino acids are widely used as humectants[18]. Amongst various amino acids, proline and PCA are particularly hygroscopic and also show a synergistic effect when mixed[19]. Those amino acids usually naturally occur inside of SC corneocytes. Skin hydration is significantly increased by formulations that mimic the skin's own natural moisturizing systems[20]. The significant increase in SC water content by 61.7% upon application of NMF moisturizer demonstrated in our work is consistent with the current body of research about benefits of NMF moisturizers.

Although glycerin is a strong humectant and moisture content should have increased in SC treated with CP, lack of such effects is not entirely unusual. Glycerin most effective when surrounding humidity is 70%[21]. Day to day humidity variation in the lab is between 30-70%.

Also there was no significant increase in water content in VE. Slightly lower water content values in CP treated VE were perhaps due to the hygroscopic properties of glycerin to draw water from the surrounding environment, including water from VE, thus lowering water content in the VE. Water content of DR treated VE increased only by 1.8%. The measurements were done within 24 hrs after treatment and perhaps that was not enough time for topical cream to penetrate deep enough into VE to produce more significant effects.

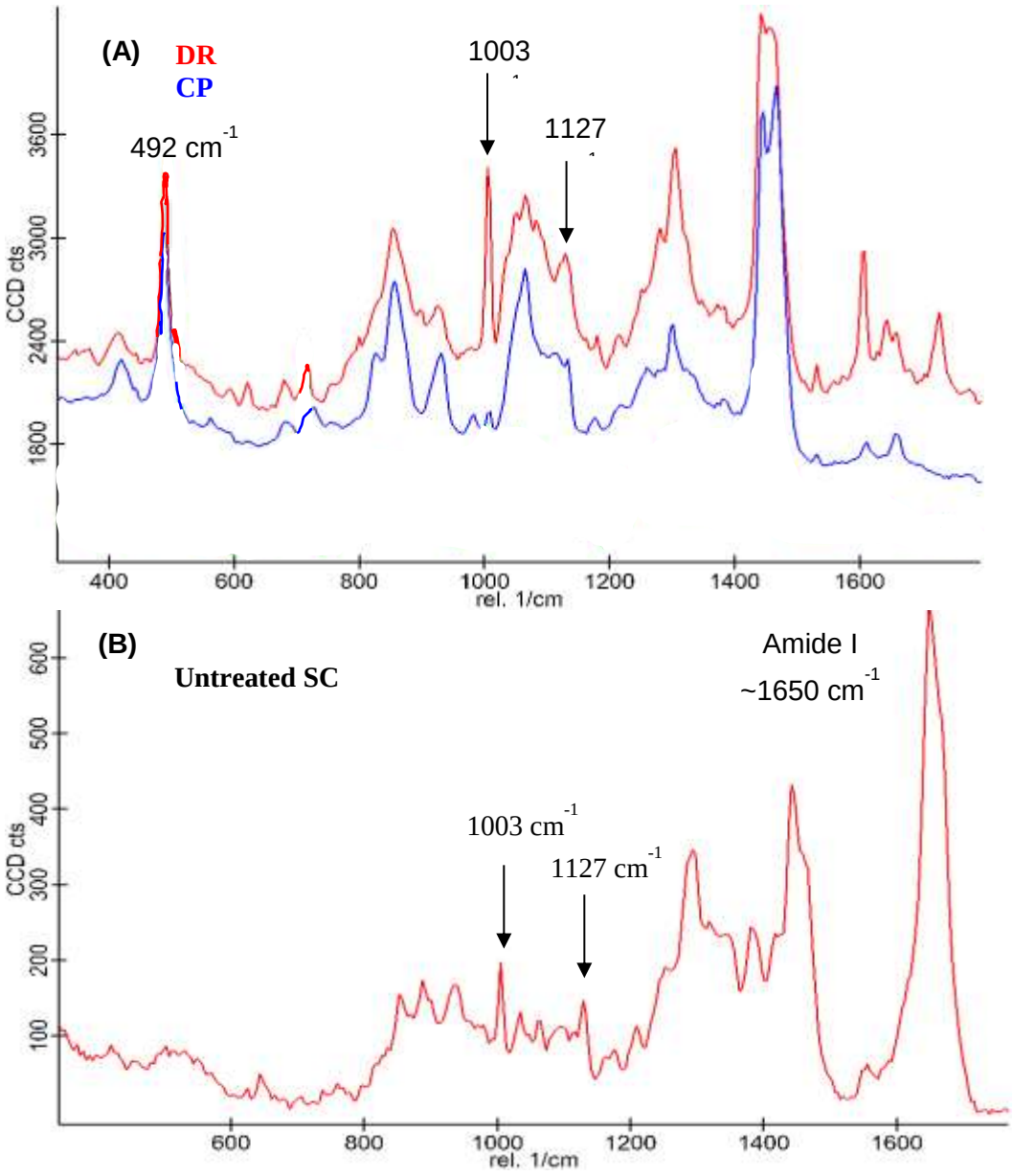

Figure 4-6. Issues with peak interferences. (A) Peaks in CP and DR formulations overlap endogenous skin peaks 1003 and 1127 cm^{-1} which serve as important markers during skin image evaluation; (B) endogenous peaks in SC

Several issues complicated current efforts to evaluate barrier function of the SC and track penetration of formulations: many formulation peaks overlapped skin peaks (see

Figure 4-5 A-B) and formulations were likely to phase separate when penetrating skin. The peak height ratio (1127/1003 cm^{-1}) is used to evaluate barrier function. The 1127 cm^{-1} peak originates from C-C stretch of all-trans lipid chains while the feature at 1003 cm^{-1} arises from aromatic C-C stretches of phenylalanine side chains. However, CP and DR formulations had Raman peaks almost exactly at the same frequencies. Therefore, it was a challenge to evaluate barrier function in regions with high levels of formulation. Two approaches were investigated in order to track formulation and to evaluate SC barrier function. First, via the peak height ratio (492 cm^{-1}/amide I as shown in Figure 4-6) and second, basis analysis approach (Figure 4-7). Both, the CP and DR formulations had unique peak marker at 492cm^{-1} which was not present in untreated skin. Therefore, the ratio of 492/Amide I peaks seemed to be a good analytical option. However, resulting images seemed to indicate formulation distribution even in untreated skin samples along the surface and in deeper regions, which was most likely due to the noise. Therefore the next option to be considered was generation of images based on the fitting of so-called "basis spectra" to the data set[22]. Basis Analysis is one of the multivariate techniques that produces intensity distribution images showing the distribution of different components. The procedure produces images with much better contrast compared with the case when only a small part of the spectrum is used (e.g., when a sum filter is used). Basis spectra can be the spectra of the pure components present in the sample. But it is noted that pure components might not be present in the sample spectra, or alternatively and it might have undergone a chemical reaction to form a new component. In addition, pure spectra cannot be easily acquired from the sample. Selective averaging is one of the methods performed to resolve these issues. The input for basis set analysis was the following: spectrum of each pure

formulation, averaged spectrum of SC, entire data set for each treatment. The fitting procedure is essentially fitting each of the spectra recorded using the basis spectra. It tried to minimize the fitting error D described by the equation:

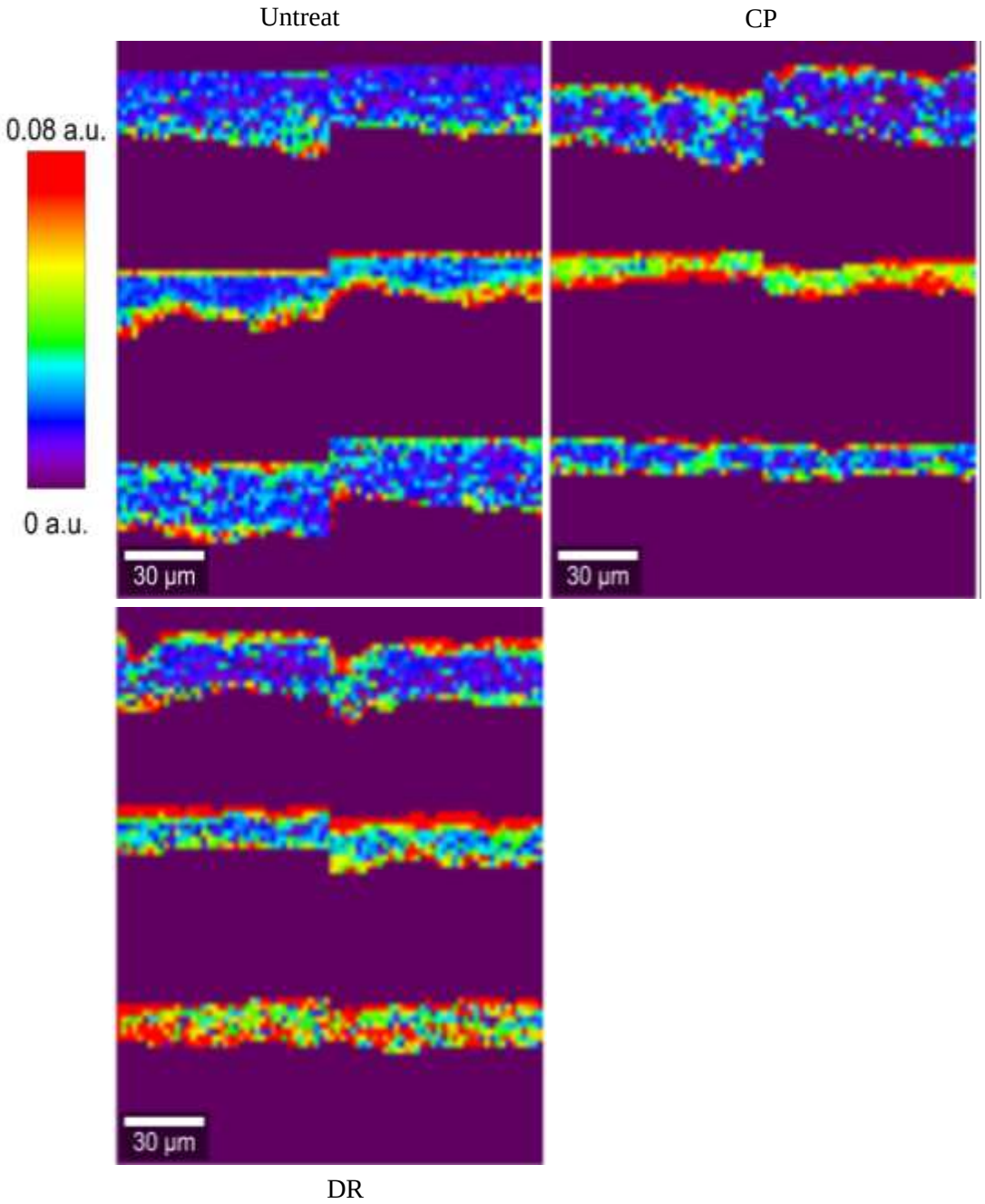

Figure 4-7. Formulation distribution image created by monitoring the intensity of the peak height ratio (492 cm^{-1}/Amide I) in delineated SC.

$$D = \left(\left[\overrightarrow{RecordedSpectra}\right]\right) - a \times \overrightarrow{BS_A} - b \times \overrightarrow{BS_B} - c \times \overrightarrow{BS_C} - \cdots)^2$$

by varying the weighting factors a, b, c, … of the basis spectra $\overrightarrow{BS}$. To improve such fits, it is better to avoid the use of the entire recorded spectral range (i.e., from 0 to 3500 cm^{-1}). The Rayleigh peak and common parts in the spectra (such as the glass substrate, for example) are best excluded from the fit. Additionally, parts of the spectra that do not contain Raman information should not be taken into account as they only contribute noise. Following the fitting of multiple spectra, the algorithm constructs one image for each basis spectrum showing the factors a, b, c, … plus one image for the fitting error D. The basis analysis fitting procedure used in this work produced such results as: one weighting factor image for each of the input spectra showing the intensity distribution and image of error. This helped to visualize the spatial distribution of the formulation and SC distribution in the skin sample (Figure 4-7). Basis set analysis produced more reliable formulation distribution images than looking at the images constructed with the peak/height ratio of 492/Amide I. Based on these formulation distribution images, a mask was created to remove spatial regions with formulation excess at the surface of SC and was also able to track the 1003/1127 cm^{-1} ratio better (supposedly with less significant interferences from the formulation peaks). Figure 4-8 (A) shows barrier function vs treatment images with masked out excess of formulation. Green, yellow and red colors represent higher intensities, hence better quality barrier function. Using these images a box plot of data was obtained (Figure 4-8 B). The median value of the lipid conformational order calculated in the untreated sample and sample treated with the CP formulation does not show statistically

significant difference (P=0.94). However there is a statistically significant difference between untreated and DR (P<=0.001) and CP and DR (P=0.005).

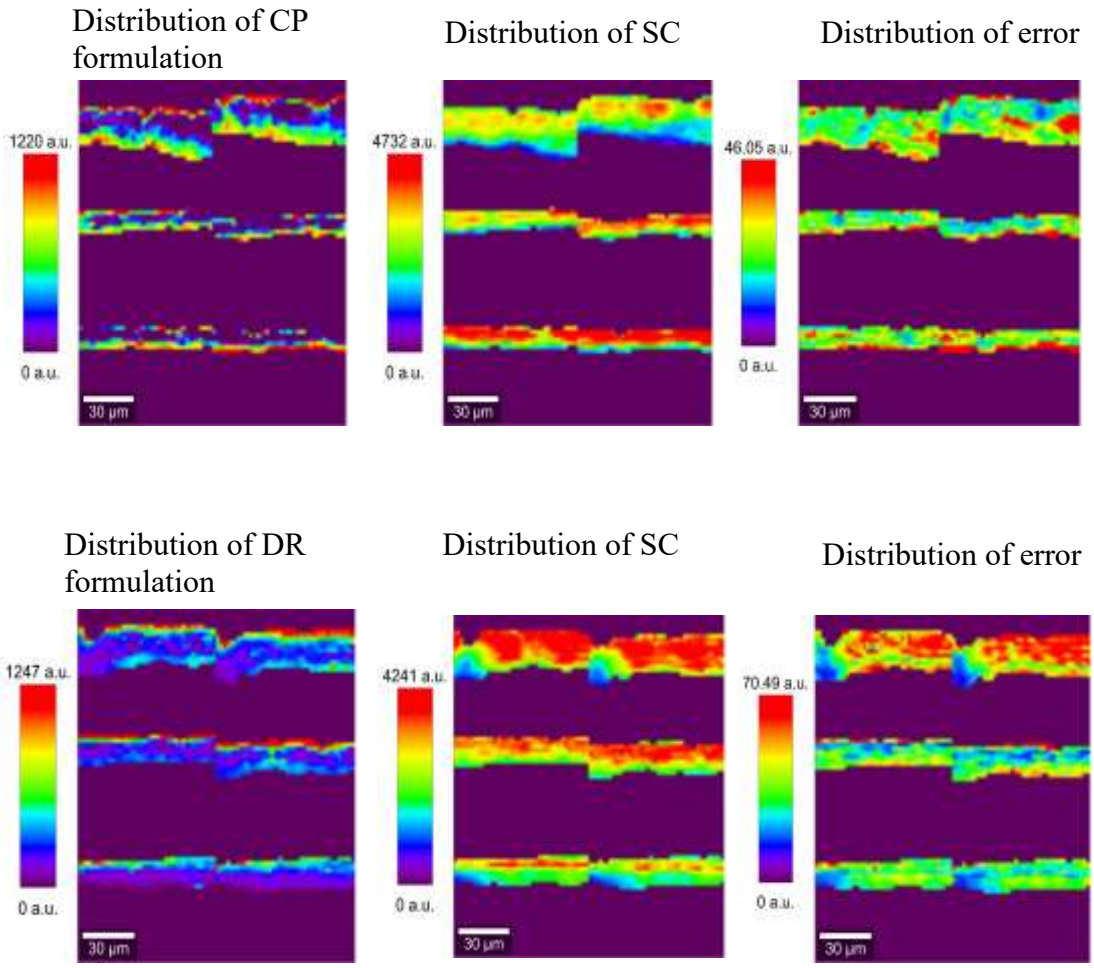

Figure 4-8. Basis set analysis results: one weighting factor image for each of the input spectra showing the intensity distribution of formulation, SC and image of error.

It is hard to say whether observed changes in lipid conformational order with DR treatment was due to the fact that NMF moisturizer does really perturb the barrier function, or whether the current data processing methods are not capable filtering out enough noise and interferences from formulation peaks.

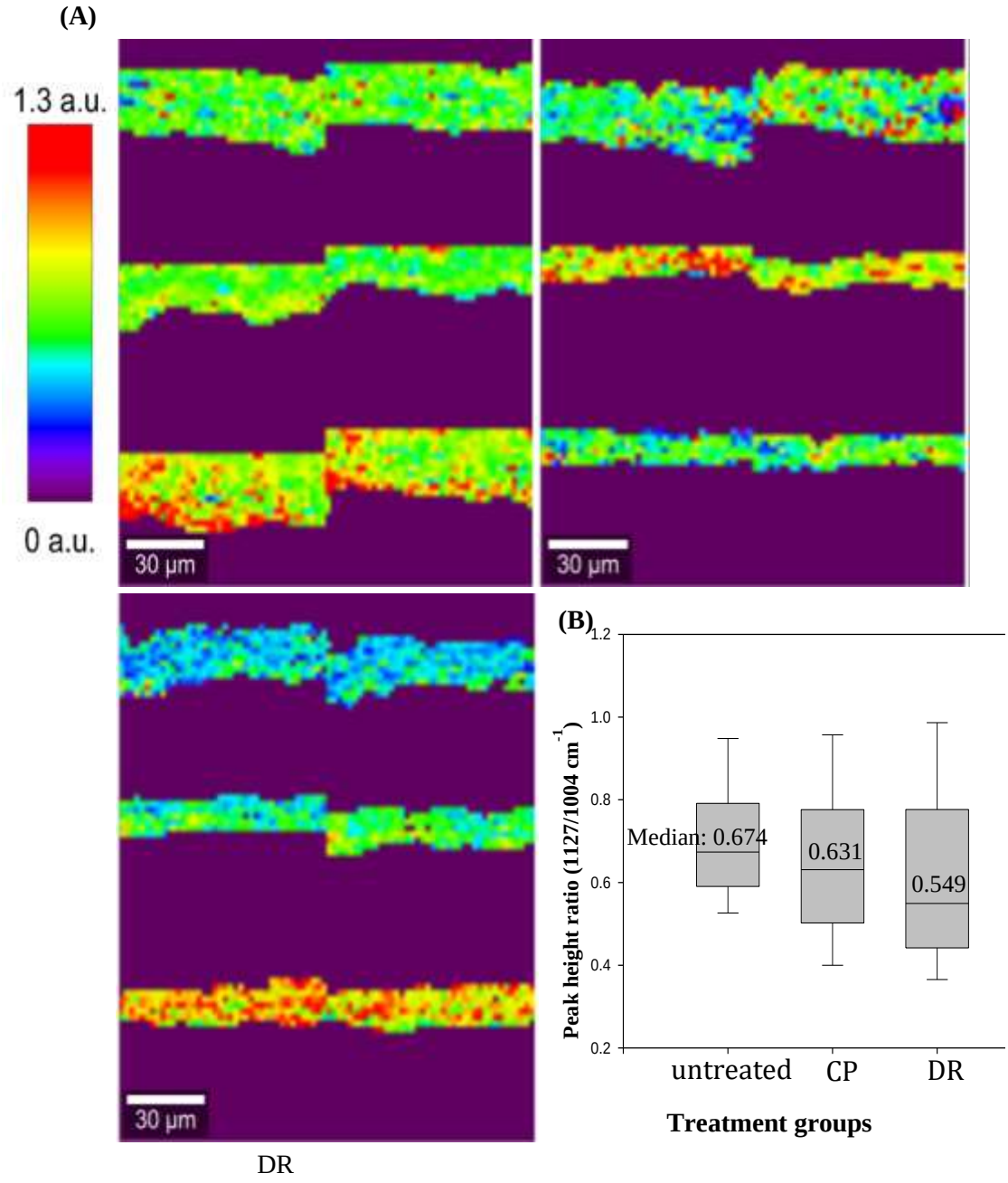

Figure 4-9. Barrier function evaluation. (A) Barrier function evaluation based on intensity of (Sum 1127/ Sum 1003) in delineated SC. Evaluation of barrier function was done following additional masking using basis set analysis to remove regions in the outermost SC with high amounts of formulation; (B) Mann-Whitney Rank Sum Test pairwise comparisons between treatments: statistically significant difference between CP & DR (P=0.005), no statistically significant difference between untreated and CP (P=0.94), statistically significant difference between untreated and DR (P<=0.001).

In this study CRM demonstrated its potential not just to measure both the water content and barrier function of SC, but also to show the spatial distribution of these parameters in the single micron distance range. CRM may be compared with the widely used TEWL method frequently used to evaluate skin barrier function. TEWL, (Transepidermal water loss) tracks the loss of water that passes from inside the body through the epidermis to the surrounding atmosphere via diffusion and evaporation processes. Measurement of TEWL is useful for detecting skin damage caused by exogenous chemicals, the impact of various formulations on the skin, physical insult (such as "tape stripping") or pathological conditions such as eczema. The lower the measured TEWL values, the better the inferred quality of the SC barrier[24]. TEWL is expressed in grams per square meter per hour and is used for studying the water barrier function of the human skin. A limitation of the approach is that the measured TEWL usually arises from a tiny spot on the surface of the SC, so the technique lacks any information on the spatial distribution of SC barrier tissue integrity. The more perfect the skin protective coat, the higher the water content and the lower the TEWL. Currently there are three different commercially available methods for evaluating skin moisture: they are based on capacitance[25] (Corneometer CM 825, Courage & Khazaka electronic GmbH, Cologne, Germany), impedance[26] (Nova Derm Phase Meter DPM 9003, NOVA Technology Corporation, U.S.A.), and conductance[27] (Skicon-200, IBS Ltd, Japan). Of the above-mentioned devices, the corneometer has gained acceptance as an efficient instrument to estimate the water content in the stratum corneum under a variety of experimental conditions. The device is based on a capacitance measurement of the dielectric medium, (the stratum corneum). With increasing hydration, its dielectric

properties change. However, these measurements provide information only from the spot limited by the size of the probe. In a typical device, the active moisture sensing area is 1.75 mm x 3.15 mm and is covered with a hygroscopic inorganic salt film. The measurement is thus macroscopic.

CRM appears be an important complimentary technique to both TEWL and capacitance measurements as it provides information on molecular level alterations in the skin barrier as well as depth profile/spatial distribution of changes in hydration level spatial distribution. As the availability of such information becomes more routine to acquire, the mechanism of action of more complex moisturizers will become better understood. As an example of an application of the approach, replacement of H_2O with D_2O was used to probe hydration mechanisms (spatial and temporal) by the Rutgers/J&J teams to investigate the delivery path of water into skin, i.e., whether water was delivered from the top or the bottom layers of the tissue[29]. This novel extension of CRM can obviously be valuable for further evaluation of water delivery mechanisms for various moisturizing formulations.

4.4 Conclusions

In comparison to traditional techniques that measure water content in SC such as TEWL or thermal conductivity, Raman imaging provides important information on water spatial distribution in the SC and VE, as well as barrier function. The advanced moisturizer (DR) containing naturally occurring (in skin) water binding compounds such as NMFs, demonstrated higher water content in SC in comparison to untreated skin or skin treated with traditional moisturizer. There is also the significant potential to use Raman imaging to evaluate barrier function.

4.5 References

1. Kwak, S., Brief E., Langlais, D., Kitson, N., Lafleur, M., Thewalt, J., "Ethanol perturbs lipid organization in models of stratum cornreum membranes: An investigation combining differential scanning calorimetry, infrared and ^{2}H NMR spectroscopy", *Biochimica et Biophysica Acta,* **2012**, 1212, pp.1410-1419.

2. Jiang, Z.-X., DeLaCruz, J., "Appearance benefits of skin moisturization", *Skin Research and Technology*, **2011**, 17, pp.51–55.

3. Igarashi, R., Suzuki, M., Nogami, S., Ohya, Y., "Molecular Dissection of ARP1 Regions Required for Nuclear Migration and Cell Wall Integrity Checkpoint Functions in Saccharomyces cerevisiae", *Cell Structure and Function*, 2005, 30, pp.57–67.

4. Matsubara, A., "Differences in the surface and subsurface reflection characteristics of facial skin by age group", *Skin Research and Technology*, 2011, 18(1), pp. 29–35.

5. Egawa, M., Hirao, T., Takahashi, M., "In vivo estimation of stratum corneum thickness from water concentration profiles obtained with Raman spectroscopy", *Acta Derm Venereol,* 2007, 87, pp. 4-8.

6. Buraczewska, I., "Skin barrier responses to moisturizers", 2008, Digital Comprehensive Summaries of Uppsala Dissertations from the Faculty of Medicine 381.

7. Rawlings, A., Canestrari, D.A.,"Moisturizer technology versus clinical performance", *Dermatologic Therapy*, **2004**, 17, pp.49-56.

8. Lodén, M. Role of topical emollients and moisturizers in the treatment of dry skin barrier disorders. Am J Clin Dermatol. 2003;4(11):771–788.

9. Harding, C.R., Watkinson, A, Rawlings, A.V., Scott, I.R., "Dry skin, moisturization and corneodesmolysis". Int J Cosmet Sci. 2000; 22(1):21-52.

10. Clar, E.J., Fourtanier, A., "Pyrrolidone carboxylic acid and the skin [in French]". Int J Cosmet Sci. 1981; 3(3):101-13.

11. Rawlings, A.V., Harding, C.R., "Moisturization and skin barrier function", *Dermatol Ther,* **2004**, 17(1), pp.43-48.

12. Marty, J.P., "NMF and cosmetology of cutaneous hydration", *Ann. Dermatol Venereol,* **2002**, 129 (1), pp.131-136.

13.Verdier-Sévrain, S., Bonte, F., "Skin hydration: a review on its molecular mechanisms", *J Cosmet Dermatol,* **2007**, 6(2), pp.75-82.

14. Rawlings, A.V., Matts, P.J., "Stratum corneum moisturization at the molecular level", *J Invest Dermatol.,***1994**, 103(5), pp.731-41.

15. Rowlings, A., "Humectants. Skin Moisturization", 2002, pp.245-250.

16. Honari, G., "Transepidermal water loss", *Applied Dermatotoxicology,* **2014**, pp.1-10.

17. Bernengo, J.-C., de Rigal J., "Physical Methods to Measure Stratum Corneum Water Content In Vivo", **2017**, pp.299-340.

18. Janssens., M, van Smeden, J., Puppels, G.J., Lavrijsen, A.P., Caspers, P.J., Bouwstra, J.A., "Lipid to protein ratio plays an important role in the skin barrier function in patients with atopic eczema", *Br J Dermatol*., **2017**, 170, pp.1248-1255.

19. Takehara, M., "Recent applications amino acids for cosmetics: interactions and synergetic effects of amino acids", 1983, *Cosmet. Toiletries*, 98, pp.51-56.

20. Sakamoto, K., "The development of two new moisturizing ingredients", 1984, *Cosmet. Toiletries*, 99, pp. 109-117.

21. Spada, F., Barnes, T.M., Greive, K.A., "Skin hydration is significantly increased by a cream formulated to mimic the skin's own natural moisturizing systems", 2018, *Clin Cosmet Investig Dermatol*., 11, pp. 491–497.

22. "Glycerine: an overview", *The Soap and Detergent Association,* **1990**, pp.1-26.

23. Robinson, M., Visscher, M., Laruffa, A., Wickett, R., "Natural moisturizing factors (NMF) in the stratum corneum (SC). I. Effects of lipids extraction and soaking", 2010, *J. Cosmet. Sci*., 61, pp.13-22.

24. Dieng, T.,"Confocal Raman Microscopy", *Springer Series in Optical Sciences,* **2010**, *158.*

25. Francesco, G., "The dynamics of TWL from hydrated skin*", Skin Research and Technology,* **2002,** 8, pp. 178–186.

26. Courage, W., "Hardware and measuring principle: corneometer" in "Bioengineering of the Skin: Water and the Stratum corneum". 1994, CRC Press, Boca Raton, pp.171-175.

27. Leveque, J.L., De Rigal J., "Impedance methods for studying skin moisturization", 1983, J. Soc. Cosmet. Chem., 34, 419.

28. Tsagami, H., “Impedance measurements for evaluation of the hydration state of the skin surface. Cutaneous Investigation in Health and Disease, Noninvasive Methods and Instrumentation”, 1980, *Marcel Dekker, New York*, pp.79-111.

29. Wang, H., Zhang, Q., Mao, G., Conroy, O., Pyatski, Y., Fevola, M., Cula, G.O., Maitra, P., Mendelsohn, R., Flach, C.R., “Novel confocal Raman microscopy method to investigate hydration mechanisms in human skin”, 2019, *Skin Res. Technol*., pp.1-9.

List of Publications

1. A. Gopalsamy, K. Lim, G. Ciszewski, K. Park, J. Ellingboe, J. Bloom, S. Insaf, J. Upeslacis, T. S. Mansour, G. Krishnamurthy, M. Damarla, Y. Pyatski, "Discovery of Pyrano[3,4-b]indoles as potent and selective HCV NS5B polymerase inhibitors", **2004**, *J. Med. Chem*. 47, pp. 6603-6608.

2. Y. Pyatski, Q. Zhang, R. Mendelsohn, C. R., Flach., "Effects of permeation enhancers on Flufenamic acid delivery in ex vivo human skin by confocal Raman microscopy", **2016**, *International Journal of Pharmaceutics*, 505(1), pp.319-328.

3. H. Wang, Q. Zhang, G. Mao, O. Conroy, Y. Pyatski, M. Fevola, G. Oana Cula, P. Maitra, R. Mendelsohn, C. Flach, "Novel confocal Raman microscopy method to investigate hydration mechanisms in human skin", **2019**, *Skin Res Technol*. pp.1–9.

4. Y. Pyatski, S. McManus, Flach, C.R., R. Mendelsohn, R.K. Prud'homme, "Flash NanoPrecipitation sunscreen formulation with beneficial properties for skin characterized by confocal Raman microscopy", **2019**, *Skin Pharmacology and Physiology*, (in publication).

List of Presentations

1. Y. Pyatski, Q. Zhang, R. Mendelsohn, C. R., Flach, **"**Confocal Raman Microscopy Tracks Cutaneous Delivery of Flufenamic Acid using Lipophilic Versus Hydrophilic Penetration Enhancers**", 2017,** *Biophysical Journal*, 112(3), pp. 454a-455a

2. Y. Pyatski, C. Flach, R. Mendelsohn, "IR Investigation of Terbinafine Interaction With Stratum Corneum Constituents" **2018**, SciX2018

3. Tierney, N.K., Wang, H., Liu-Walsh, F., Edison, B.L., Dufort, M., Y. Pyatski, Flach, C.R., Mendelsohn, R., Green, B., "Confocal Raman Imaging and 5 Environmental Stressors Model Demonstrates Benefits of Antiaging Facial Cream for Deep Hydration and Protection Against External Aggressors*",* **2019**, *77th Annual Meeting of the American Academy of Dermatology, Washington, DC; March 1–5, 2019*